AGNOSTIC TRACKING: NANOSCALE, HIGH BANDWIDTH, 3D PARTICLE TRACKING FOR BIOLOGY

Kalpit V. Desai

A dissertation submitted to the faculty of the University of North Carolina at Chapel Hill and North Carolina State University in partial fulfillment of the requirements for the degree of Doctor of Philosophy in the joint Department of Biomedical Engineering.

Chapel Hill, NC
2007

Approved by:

Dr. T. Gary Bishop (Research Advisor)

Dr. Carol Lucas (BME Advisor)

Dr. Richard Superfine (Reader)

Dr. Stephen R. Quint (Reader)

Dr. Russell M. Taylor, II

ABSTRACT

KALPIT V. DESAI: Agnostic Tracking: Nanoscale, high-bandwidth, 3D particle tracking for biology
(Under the guidance of Dr. T. Gary Bishop)

The ability to detect biological events at single molecule level provides unique insights in the field of biophysics. Back-focal-plane laser interferometry is a promising technique for single-molecule-scale, 3D position measurements at rates far beyond the capability of video. I present an in-situ calibration method for the back-focal-plane, low-power (non-trapping) laser interferometry. The software-based technique does not rely on any a priori model or calibration knowledge; hence the name Agnostic. The technique is sufficiently fast and non-invasive that the calibration can be performed on the fly, without interrupting or compromising the on-going experiment. The technique can be applied to track 3D, long range motion (up to 100 um) of a broad variety of microscopic biological objects. The spatiotemporal resolution achieved is of the order of a few nanometers and tens of microseconds.

Three biological applications enabled by the technique are presented: firstly, a prototype of an oscillating-bead high-bandwidth frequency-response analyzer for biology, based on Agnostic Tracking as implemented in our custom-built 3D Magnetic Force Microscope (3DFM); secondly, a magnetic-force study that revealed a previously-unknown anchoring-dependent nonlinear response of a cellular membrane; last, a rheological study that revealed a novel grouping of motion characteristics of individual vesicles diffusing inside live cytoplasm.

Dedicated to

My loving parents

ACKNOWLEDGMENTS

I would like to thank:

My committee members, Gary Bishop, Carol Lucas, Richard Superfine, Russell Taylor, and Stephen Quint, for their cooperation and supervision of this thesis

Gary Bishop, for being my advisor, sharing with me his original idea of injecting perturbations as a calibration method, and providing a relentless support throughout which made this dissertation possible

Richard Superfine, for stimulating the biophysicist inside me, and being an inspiration for how to appreciate and reconcile seemingly inconsistent perspectives

Russell M. Taylor, for a continuous financial support and valuable guidance on software development

Leandra Vicci, for introducing me to the Nanoscale Sciences Research Group, for always being there to troubleshoot technical emergencies, for continuously providing unique perspectives and valuable insights into electromagnetism, scattering theory, and almost every field of engineering

E. Tim O'Brien, for teaching me biology and being a good experiment buddy

David Marshburn, for his help with software development and data management

Jay Fisher, Jeremy Cribb, Ben Wilde, Sreeja Asokan, and David Hill for being my lab-mates, introducing me to the 3DFM, and continuously helping me on issues from making a specimen to aligning the optics

All members of the Nanoscale Sciences Research Group, for making my stay at UNC a pleasant and unforgettable experience

Gary Johnson, Ken Jacobson, and Yun Chen, for sharing materials and providing biological insights

Janet Jones, Sandra Neely, Tiffany Harris, Julie Edwards and Nancy McKinney, for making the wheels the bureaucracy turn

My parents, brother and sister-in-law for their love and impeccable trust

TABLE OF CONTENTS

LIST OF FIGURES

LIST OF TABLES

LIST OF ABBREVIATIONS

2D	Two Dimensional
3D	Three Dimensional
3DFM	Three Dimensional Force Microscope (Microscopy)
ADC	Analog-to-Digital Converter
AFM	Atomic Force Microscope (Microscopy)
AOD	Acoustic-Optical Deflectors
BFP	Back Focal Plane
DAC	Digital-to-Analog Converter
GPI	Glycosylphosphatidylinositol
HBC	Human Breast Cancer
MCL	Mad City Labs
MSD	Mean Squared Displacement
MTC	Magnetic Twisting Cytometry
NA	Numerical Aperture
OT	Optical Tweezers
PFM	Photonic Force Microscope (Microscopy)
PSD	Power Spectral Density function
QPD	Quadrant Photo Diode
SPT	Single Particle Tracking
SVD	Singular Value Decomposition
UNC-CH	University of North Carolina at Chapel Hill

LIST OF SYMBOLS

$\hat{x}$	(hat) Estimated value of variable x
$\overline{x}$	(overhead bar) x is a vector
$\vec{x}$	(overhead arrow) x is a real-space vector
$\overline{\overline{X}}$	(bold with overhead bar) *X* is a matrix
$E[x]$	Expected value of the quantity x
$\sigma[x]$	Variance of the quantity x
$x \mid y$	Value of x for a given value of y
$\overline{\overline{X}} \times \overline{\overline{Y}}$	Matrix Multiplication between matrices *X* and *Y*
$\Re_{X,Y}[\phi]$	Correlation between quantities *X* and *Y* at lag ϕ
$X * Y$	Convolution between quantities *X* and *Y*
$A(\tau)$	Specimen-translation-stage Impulse Response
$H(\tau)$	Position-Feedback Loop Transfer Function (H)
$\vec{W}$	Perturbations in stage command (W)
$\vec{\lambda}$	Perturbations in stage position (lambda)
F_{QP}	Mapping from QPD signals to probe position (relative to laser)
F_{PQ}	Mapping from probe position (relative to laser) to QPD signals

Chapter 1 Position tracking in biology

1.1 Particle tracking provides specific insights in local environment

The ability to image and manipulate biology provides novel biophysical insights. Quantities that may be of interest of investigation are several, e.g. viscoelasticity, stiffness, temperature, force etc; however displacement is most often the raw observation while other quantities are derived there from. In contrast to bulk imaging techniques (e.g. FRAP, FRET etc), which only give ensemble averaged measurements, monitoring motion of individual microscopic objects provide insights into local characteristics of a heterogeneous environment. The task of monitoring the motion is commonly referred to as *tracking*; the object whose motion is being monitored is referred to as a *probe* or a *particle*; and the techniques employed are collectively referred to as single particle tracking (SPT) techniques. SPT techniques can be broadly classified into two categories: one, where the probe being tracked is an external particle mechanically coupled to the biological entity of interest, e.g., a beating cilium, a cell membrane etc; and two, where the motion of the biological entity itself is directly monitored, e.g., an organelle diffusing inside a cytoplasm. Let us briefly review the history of single particle tracking techniques.

1.2 History of single particle tracking techniques

The first usage of particle tracking in biology was demonstrated by Crick et al in1950 [1] in a work that was seminal for multiple paradigms. They inserted 5 μm length (longest dimension) magnetic particles into chick fibroblasts using phagocytosis – a process by which cells engulf particles attached to their surfaces, and pulled them using an external magnetic field to probe properties of the cytoplasm. Images were cinemicrographically recorded on a Kodak 55 mm film at 9 to 15 fps. Angular displacement of the particle was measured manually for each frame using a pencil, a millimeter graph paper, an eyepiece, and a large protractor. Yagi [2] used a similar approach to investigate properties of amoeba protoplasm, while Abercrobie et al [3, 4] used a slight variant, time-lapse cinemicrography, to investigate locomotion of fibroblasts by tracking motion of adherent particles. The first use of SPT using computer-enhanced video recording was reported by Webb and collaborators, in which they tracked fluorescent-labeled low-density lipoprotein (LDL) receptors in human-fibroblast cell membranes [5]. Since then, SPT has quickly become widely used for microscopic position measurements in biology [6-10]. De Brabander et al developed Nanovid ultramicroscopy, a technique for tracking colloidal gold particles of 20 to 40 nm diameter, in which they used endocytosis and protein motion on the surface of the cell membrane for tracking [6, 11-13]. Sheetz and collaborators developed particle tracking techniques based on differential interference contrast (DIC) microscopy to track the motion of motor molecules

and membrane proteins with nanometer resolution [14-17]. Fujiwara et al [18] and Murase et al [19] used colloidal gold particles with a high-speed video camera, to track tagged lipids of a cell membrane with a spatial precision of 17 nm at sampling rate of 40 kHz. Selvin and collaborators developed Fluorescent Imaging with One Nanometer Accuracy, i.e. FIONA, a method for tracking a single fluorophore by fitting a Gaussian model of the point-spread function to the image of the fluorophore [20]. This method offers spatial resolution of 1.5 nm and temporal resolution of 0.5 s to 0.1 s, which they used for investigating molecular motor activities [21]. Most of these techniques were applicable for position detection only in the focal plane of the camera. Speidel et al [22] developed a tracking technique using epifluorescence video imaging in off-focus mode, enabling tracking of particles moving less than 3 μm in axial direction with 100 ms temporal resolution. Video based tracking is fundamentally limited by the number of detected photons, so spatial resolution varies inversely with the frame rate. Recently Gratton and collaborators reported a creative laser-based feedback mechanism where a beam continuously orbits, circular in XY and steps in Z, around the particle. The center of the orbit is dynamically adjusted to keep the PMT (photo-multiplier tube) signal minimized, and the location of the center is used as the measurement of particle position. This approach was applied to track fluorescent particles in 3D with spatial resolution of 20 nm and temporal resolution of 30-60 ms [23-25].

1.3 Biological studies demanding high spatiotemporal resolution

As one can deduce from the review presented above, most of the particle tracking techniques work only in 2D, and none the techniques provide both high spatial and temporal resolution, at the same time. At the single-molecule level, the characteristic displacement is a few nanometers, e.g., the step size of a molecular motor, diameter of a protein etc.; where as the characteristic time is of the order of tens of microseconds e.g. the rise time of Myosin. Also, because biomolecular motion is not constrained to be in 2D, 3D measurements enable a more complete picture and thus are desirable. Let us consider a few biological problems that require 3D position measurements with high spatiotemporal resolution.

1.3.1 Probing viscoelastic properties of the cytoplasm

In spite of significant efforts and substantial advancements in the field of biophysics, viscoelastic property of various regions of the cytoplasm is an active area of research. One appealing approach for probing properties of the cytoplasm is to analyze the diffusive or driven motion of endoplasmic particles. The particle being tracked could be a phagocytosed bead or it could be an endogenous vesicle. Magnetic beads can also be ingested by cells and pulled by magnetic fields. Because neither passive nor driven motion is normally constrained to be in the imaging plane, 3D position detection is usually required. Detection of nanoscale steps may suggest molecular-motor activity [20].

Because much of the diffusive motion occurs at short time scales, high temporal resolution is preferred when investigating viscoelastic properties of cytoplasm.

1.3.2 Probing dynamics of cell membranes

The mechanical properties of cell membranes and the cytoskeleton are important for understanding the structure of cells and how they respond, through remodeling and gene expression, to external stimuli. These responses can be fast when related to the intrinsic mechanical properties of the cell structure, or slow when indicating the biochemical response of the cell. We can attach functionalized beads to the cell membranes and monitor their motion in response to external magnetic force. Such measurements of the creep response may reveal valuable information about viscoelasticity of the membrane. Also, hop diffusion has been exhibited in gold particles attached to phospholipids embedded in the cell membrane; where it is hypothesized that a plasma membrane is compartmentalized and the probe hops through one compartment to another. Using the techniques available at the time, Kusumi, Jacobson and collaborators [9, 18, 26] were able to measure two nested levels of compartments, where 230 nm compartments exist within larger 750 nm compartments. A probe on average spends around 10 ms and 330 ms in the respective compartment levels. Quoting the publication [26],

> *"…hop diffusion on a very fine scale is generally not detected. This is because the time (approximately microseconds) and distance scales (approximately tens of nanometers) needed to visualize the membrane skeleton fence in full detail require much higher temporal resolution…"*

Clearly, a position measurement system with desired spatiotemporal resolution would enable further investigation.

1.3.3 Actin-Based Motility

The forces generated by the polymerization of actin underlie many forms of cellular motility. Extension of lamellipodia, filopodia, ruffles and amoeboid "crawling" in eucaryotic cells -- which are essential for several cellular processes including wound healing, embryonic development, neuron outgrowth and the metastasis of cancerous cells -- depend on the forces derived from actin polymerization. In addition, several cellular pathogens, including the bacterium *Listeria monocytogenes*, hijack the host cell's cytoskeletal proteins to assemble actin filaments and propel themselves through the host cell cytoplasm [27, 28]. Bacterial actin-based motility can be realized in vitro by coating a submicron sized bead with the bacterial protein, ActA, which is then put into the cytoplasmic extract [29]. Measuring the thermal fluctuations of the bead while undergoing motility would be of great interest. The nanometer scale steps in the bead motion may reveal insertion of actin monomers. The high bandwidth fluctuations may reveal insights about the properties of the bacterial connection to the actin tail. Overall, the study may provide critical insights on the mechanism by which the pathogen moves within and between eukaryotic cells. Technological demands for this study include the ability to track the 3D trajectory of ActA-coated magnetic beads in cytoplasmic extracts with nanometer scale spatial and approximately 50 microsecond temporal resolution. Tracking the motion of the bead for ranges up to 15 microns along all 3 axes is necessary.

1.3.4 Cystic Fibrosis

Cystic fibrosis (CF) is a genetic disease affecting approximately 30,000 children and adults in the United States. In a healthy lung, cilia beat in a whip-like fashion to propel the particulate-laden mucus to the glottis where it is expelled from the airways and swallowed. The coordinated activity of thousands of molecular motors oscillates cilia to cause the flow of the pulmonary barrier fluid over long distances. It is also hypothesized that cilia play a sensory role in the feedback loop that stabilizes the salt-water transport system. In Cystic Fibrosis, a defective CF gene disrupts the equilibrium of the salt-water transport system. This in turn produces thick and sticky mucus and subsequently clogs the mucociliary clearance system, which is the first line of defense against inhaled particulates, aerosols, and pathogens in the airways of the lung [30]. We can attach magnetic beads to the cilia and apply magnetic forces to the beads using our home-built 3D Force Microscope (3DFM); instrumentation aspects of 3DFM will be described in more detail in chapter 6. Measurement of the motion of the bead attached to cilia can be used to compute forces generated by cilia. Measurement of the motion of other beads in the vicinity of beating cilia may help us understand the cilia-induced hydrodynamics and viscoelastic properties of the mucus.

The next chapter will describe Laser Interferometry, a 3D position detection system that promises the high spatial and temporal resolution that is required by the studies described above.

Chapter 2 Back-focal-plane laser interferometry

We saw in the previous chapter that several biological problems demand spatiotemporal resolution of the order of nanometers and tens of microseconds. In this chapter, I will review back-focal-plane laser interferometry, a technique that promises subnanometer resolution at rates of 100s of kHz.

2.1 Introduction to back-focal-plane laser Interferometry

Back-focal-plane laser interferometry was first developed to measure the position of a particle inside an optical trap [31-37], and recently its use for position detection at low, non-trapping power was reported [38-41]. As shown in Figure 2-1, a probe placed in the focus of a coherent laser beam causes light scattering and an interference pattern between scattered and unscattered light is produced. This interference pattern is projected on a quadrant photodiode (QPD) that is placed at the back-focal-plane of the objective. A photograph of the interference pattern observed on a QPD is shown in the upper-right corner of Figure 2-1. The QPD produces four electrical signals, each as a function of the incident-light intensity. Motion of the probe within the beam causes a change in the interference pattern, which in turn changes the QPD signals. As shown in Figure 2-2, a lateral displacement with respect to the optical path causes a shift

in the interference-pattern projection, while an axial displacement causes a change in the radius of the fringes of the interference-pattern projection.

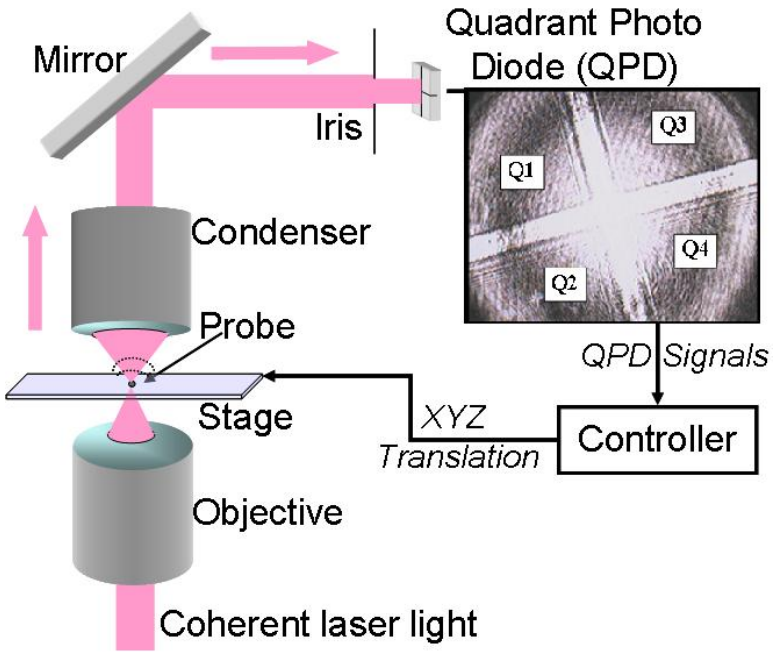

Figure 2-1: Layout of a back-focal-plane interferometric tracking system

Because the operable volume of the interferometric detection system by itself is limited to the size of the beam-waist, i.e., smaller than 1 μm^3, position feedback is often added to keep the probe centered in the laser. Position feedback is implemented either by moving the specimen relative to the laser using a specimen-translation stage or by moving the laser relative to the specimen using acoustic-optical deflectors (AODs). We used Nano-LP 100 from Mad City Labs Inc., a closed loop specimen-translation stage with subnanometer accuracy and 100 μm range for all three axes.

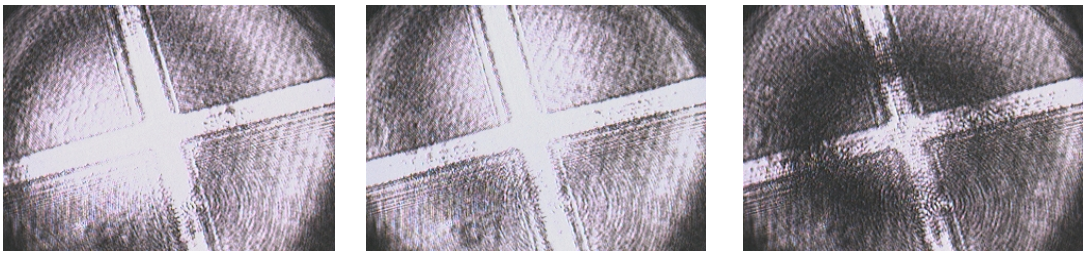

X Y Z

Figure 2-2: Diffraction patterns generated by displacements along axes

2.2 Calibration of the detector response: State of the art

In order to measure the position of the probe, the detector (QPD) must be calibrated, i.e., the mapping from four QPD signals to 3D probe position must be known. In theory, for particles within limits of Raleigh scatterer (diameter < 0.2*wavelength), sums and differences of the individual quadrant signals give the 3D position of the particle with subnanometer accuracy at bandwidths only limited by the detector electronics (up to 1 MHz). Rohrbach and collaborators have also developed rigorous mathematical methods for mapping four **Q**PD signals into 3D **p**robe position (referred to as QtoP map or F_{QP}) for probes larger than Raleigh scatterers [42, 43]. In spite of the significant theoretical development and the potential for unmatched spatiotemporal resolution, the adoption of laser interferometry has been relatively limited. This reluctance can largely be attributed to the stringent constraints put by theoretical models over shape, size and composition of the probes. Interpretation of the QPD signals, as offered by the theoretical models, gets extremely complex for particles larger than a Raleigh scatterer.

Theoretical models also assume dielectric particles or, at the best, particles with uniform refractive index. Simulations have shown that the F_{QP} quickly departs from the linear differences-and-sums relationship for gold particles even with sizes smaller than Raleigh scatterer [44]. To the best of our knowledge, no such analytical model for magnetic particles has been reported. Magnetic tweezers, a technique gaining wide popularity among biophysicists [1, 45-55], requires magnetic probes for application of force. The ability to track magnetic beads with laser interferometry promises synergistic advantages, enabling a wide range of experiments. Our custom built three-dimensional force microscope (3DFM) [49] was designed to utilize this synergy, which required the development of a technique for tracking magnetic beads.

Traditionally, the parameters of F_{QP} are computed by fitting analytical models to a volumetric-scan data acquired by raster scanning a probe that is immobilized relative to specimen. Thus estimated parameters of F_{QP} are then used to measure the position of the probe of interest. Raster-scan calibration has severe limitations in addition of being tedious. Because the probe whose motion is of interest is different from the probe used to estimate F_{QP}, probe-to-probe variations significantly compromise the accuracy of position detection. To avoid these probe-to-probe variations, Lang et al. reported fitting multivariate nonlinear polynomials as F_{QP} for each probe of interest [38]. A high-power laser was used to trap and scan the particle across a surface within a low-power, detection laser; and the calibration of the detector over that surface was then used for position detection in 2D. If this approach is extended to 3D, relatively high trapping power injected in the specimen to facilitate the calibration scan may cause local heating

[56-59]. Also, because optical trapping is employed, the probes to be used must be optically trappable. Unfortunately, trapping magnetic particles is hard because of the non-uniform distribution of magnetic content. Moreover, because the trap-enabled calibration scan moves the bead relative to its environment, mapping from trapping force to bead position must be known in order to calibrate the response of the detector in terms of bead position. Unfortunately, this mapping usually depends on unknown viscoelastic properties of the environment.

2.3 Need for on-the-fly calibration of the detector response

In addition of their individual limitations, both of the calibration approaches listed above suffer from a common limitation; they only facilitate a static approximation of F_{QP}. The true F_{QP} is a function of the refractive index of the immediate environment of the probe. As the probe moves through an optically heterogeneous environment, F_{QP} changes. Figure 2-3 shows results of a simulation carried out using Mie scattering theory for plane waves as presented in Born and Wolf [60] for a 1 μm diameter sphere with a refractive index of 1.5 in an 830 nm coherent laser beam. The E field associated with scattered light is compared for three different indices of refraction, chosen in a range that is commonly observed for cytoplasm. As seen in the figure, the azimuthal scattering field changes by 500% for a 10% change in the refractive index. These changes in the scattering field manifest as changes in the interference pattern and ultimately changes in the QPD signals. Because the QPD signals depend quadratically on the field, a change in the refractive index of the medium can

dramatically affect the QPD response to probe motion, i.e., F_{QP}. This simulation therefore shows the true F_{QP} is likely to change as the probe moves through an optically heterogeneous biological environment.

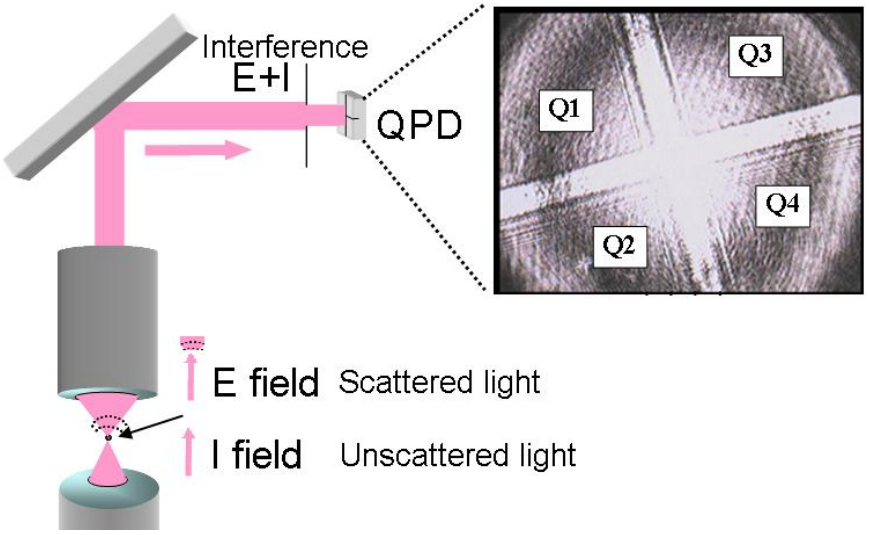

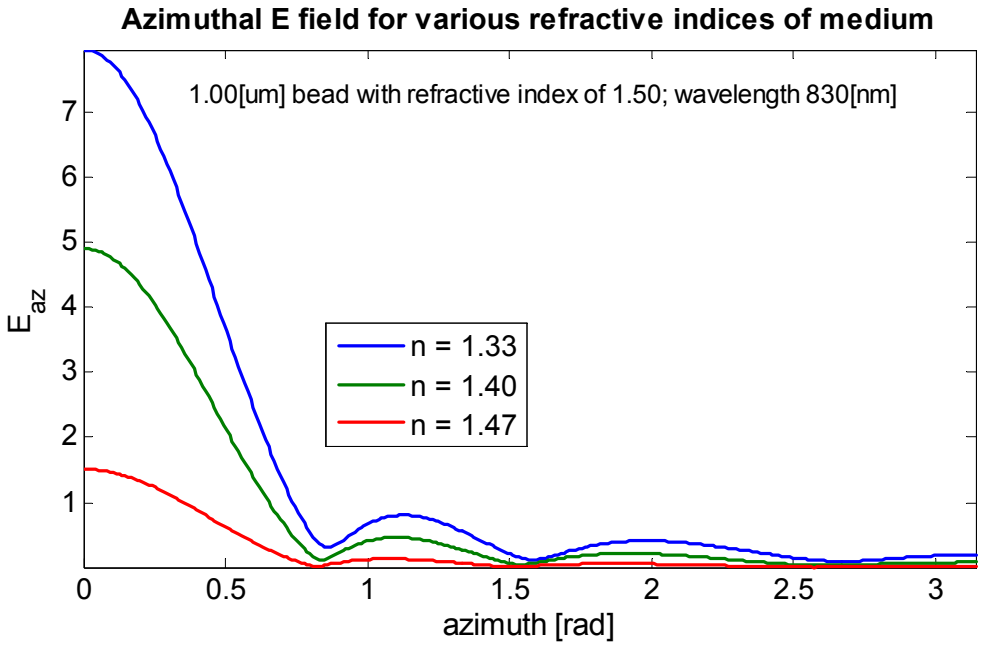

Figure 2-3: Effect of refractive-index variations on the scattering field

The feedback loop normally operates with sufficient loop gain to suppress errors in $\hat{F}_{QP}$ due to this effect. However this suppression only operates within the feedback loop bandwidth which is severely limited by the mechanical stage response. Measuring bead motion up to the bandwidth of the QPD signals, which is typically far greater, is desirable. However, this information is only accessible from the loop error signal, which itself is necessarily "open loop." Therefore, the wideband component of the bead motion cannot be compensated and relies on the accuracy of $\hat{F}_{QP}$. Therefore, environment-induced changes in the true F_{QP} introduce a "hidden" error at these frequencies that cannot be detected. For accurate wideband tracking, the variations in the true F_{QP} must be accounted for.

2.4 Optimization of sensitivity

It is known that the mapping function from QPD signals to probe position has less-sensitive as well as multivalued regions, i.e., regions where two or more probe positions produce identical set of QPD signals. To be able to detect nanoscale biological events, it is desirable to have high sensitivity. For a given amount of system-noise, a higher sensitivity provides a better signal-to-noise ratio and enables detection of smaller displacements. Also, for the position measurements to be unambiguous, it is necessary to avoid multivalued regions. Both of the above require an ability to optimally adjust the location of the probe relative to beam such that we operate in a linear neighborhood with high sensitivity.

As described above, there is a driving motivation for a detector-calibration technique that does not rely on analytical models; that can be used for tracking magnetic beads; that facilitates on-the-fly calibration of the detector; and that facilitates optimization of the detector sensitivity.

2.5 Thesis Statement

I present Agnostic Tracking, a detector-calibration approach that can augment the laser interferometric 3D position detection system by

1. *significantly relaxing constraints over probe size, shape, and composition*
2. *enabling on-the-fly calibration of the QPD response to probe motion*
3. *facilitating maximization of the QPD sensitivity*

Briefly, we inject perturbations in the position of the specimen-translation stage, which in turn introduces perturbations in the probe position relative to the laser. Changes in the QPD signals that are caused by the known perturbations in the probe positions are used to extract the calibration parameters. The technique does not rely on prior knowledge of the calibration parameters or an analytical model, hence the name Agnostic. The technique uses a single, low-power, non-trapping laser and does not require a major change to the basic instrumentation of a back-focal-plane interferometric-detection system. Because optical trapping is not employed, local heating of the specimen is avoided and magnetic beads can be used. We demonstrate versatility of the technique by tracking 3D motion of unlabeled organelles moving inside live cells and tracking magnetic beads

attached to live cell membranes. The technique is sufficiently fast and noninvasive that the calibration can be performed on-the-fly frequently, and if desired, continuously.

The next two chapters (3, 4) will describe the method for calibrating the detector formally and in detail. Chapter 5 will show performance evaluation of the calibration algorithm. Chapter 6 will present a technique for dynamically optimizing the sensitivity and its test on a volumetric-scan dataset. The remainder of the dissertation will present selected biological applications of Agnostic Tracking. Chapter 7 will describe using the 3DFM as a frequency-response analyzer for biology. Chapter 8 will describe biological results obtained by probing cell-membrane mechanics and tracking organelles diffusing inside cytoplasm.

Chapter 3 Agnostic Tracking method

Agnostic Tracking is based on methods from system identification. The term *system identification* refers to the process of extracting parameters of a mathematical model of the system dynamics by analyzing input-output signals of the system. For us, the system to be identified is the transfer function from four QPD signals to 3D probe position. We inject small perturbations in the drive signal of the specimen-translation stage and thus in the probe position relative to the laser. These perturbations cause small changes in the QPD signals. The stage position reported by stage sensors and simultaneous QPD records are then analyzed to estimate the mapping from QPD signals to probe position. Building upon this overall framework, this chapter will describe Agnostic Tracking in a formal and mathematical manner.

3.1 Instrumentation of the interferometric tracking system

All the instrumentation referred here was of the second generation of 3DFM as reported in [48]. We used an 825 nm, 36 mW fiber-coupled diode laser (model IFLEX1000-P-2-830-0.65-35-N; Point Source, Southampton, England) for position detection. Laser power at the specimen plane is approximately 25 μW, too low to damage a specimen. Feedback signals are obtained from a Quadrant Photo Diode (model QD-.05-0-SD; Centrovision, Newbury Park, CA). Because

10 kHz was a high enough sampling rate to satisfy our experimental needs at the time, we modified the QPD electronics to have a 40 kHz cutoff frequency. A three-axis closed-loop nanopositioning stage (model Nano-LP 100; Mad City Labs Inc., Madison, WI) is used for computer-controlled specimen-translation relative to the laser. For more details, please refer to our previous instrumentation paper [48].

3.2 Coordinate frames and related notations

A scientist is primarily interested in measuring the motion of the probe relative to the specimen; which may be caused by diffusion, other interactions with the environment, and external forces. In laser interferometry, the motion of the probe relative to the specimen, at short time scales, causes small excursions away from the laser. These excursions can be measured by a QPD provided that an estimate of F_{QP} is available. Because the laser-interferometry detection system by itself can only function within about 1 μm of the focused laser beam waist, longer range excursions must be assisted by a specimen-translation stage driven by a computer-based feedback controller. The controller software moves the stage (and thus the whole specimen) relative to the laser to keep the probe within the operable range of the laser. Thus, to measure the probe's displacement relative to the specimen at any moment, we need to combine two independent measurements:

1. The probe's displacement relative to the laser beam waist as detected by the QPD, and

2. The cumulative displacement of the stage since the beginning of the experiment.

It is therefore convenient to define two coordinate systems: a **S**pecimen Coordinate Frame (SCF) to express probe motion relative to the specimen; and a **L**aser Coordinate Frame (LCF) to express probe motion relative to the laser beam waist.

Let us follow the notations below to represent a point and its coordinates:

$A(t)$: A point *A* in space at time t

$\vec{A}_F(t)$: Coordinates of the point *A* at time t in the *F* coordinate frame.

*F**: The origin of coordinate frame *F*

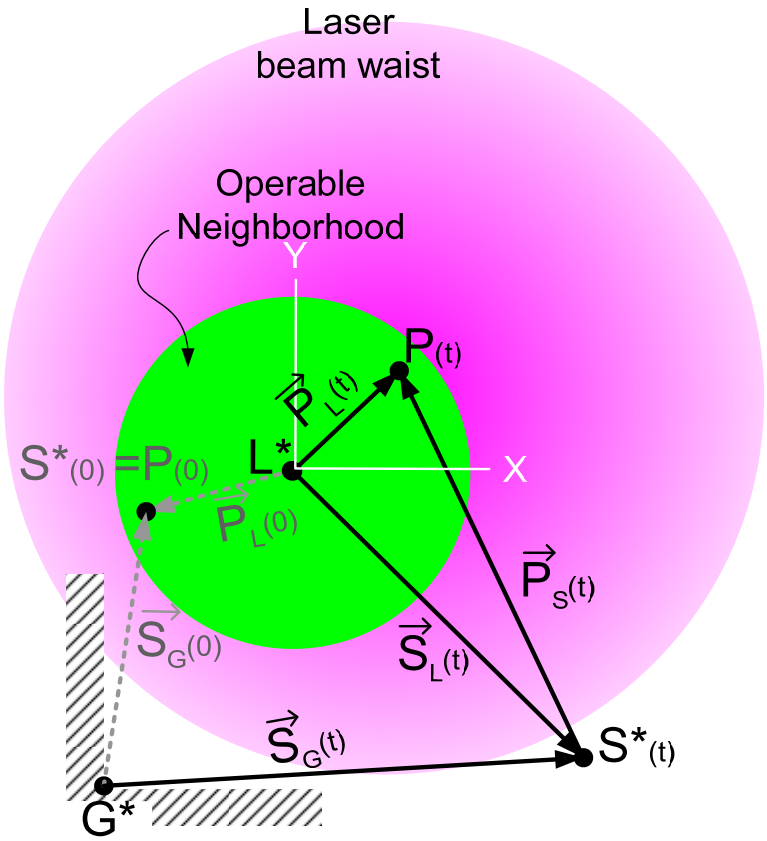

Figure 3-1: 2D projection of coordinate-frames arrangement

Figure 3-1 shows the relationship between coordinate frames. Let L* designate the location of the origin of the LCF, and the circle around it represent an *operable neighborhood*. The *operable neighborhood* is defined as the region of the laser beam beyond which accuracy of the last estimate of F_{QP} is undetermined. Because we do not know or control the position of the probe in the geometry of the beam-waist, the operable neighborhood is not shown to be centered in the beam-waist. The function of position feedback is to keep the probe within the operable neighborhood. Let us choose a point S* within and fixed relative to the specimen, as the origin of the SCF. It is convenient to let S* be the initial location of the probe in the SCF. Let point P designate the probe position which is arbitrary at time t=0 and to be determined at time t, constrained at both times only to be within the operable neighborhood. In a global laboratory reference frame let us define an origin G* to be the location of the stage when stage-sensor output is zero. Using the notations defined above we have,

$\vec{P}_L(t)$: Coordinates of the probe at time t in the LCF,

$\vec{P}_S(t)$: Coordinates of the probe at time t in the SCF,

$\vec{S}_G(t)$: Coordinates of the stage at time t as reported by sensors,

$\vec{S}_L(t)$: Coordinates of the stage at time t in the LCF, and

$$\vec{P}_S(t) = \vec{P}_L(t) - \vec{P}_L(0) + \vec{S}_G(0) - \vec{S}_G(t)$$

The position $\vec{S}_L(t)$ of the stage relative to the laser is computed simply by adding a constant offset $\vec{P}_L(0) - \vec{S}_G(0)$ to sensor outputs $\vec{S}_G(t)$. For describing *relative* dynamics, we may use $\vec{S}_L(t)$ to represent the stage displacement reported by its sensors and omit the Global coordinate frame from further discussion. Thus we write,

$$\widehat{\vec{P}}_S(t) = \widehat{\vec{P}}_L(t) - \vec{S}_L(t) \qquad \text{Equation 3.1}$$

Equation 3.1 is used to maintain a time-history record of probe position relative to the specimen. Note that I have put a hat (^) on $\vec{P}_L$ (and thus also on $\vec{P}_S$), to differentiate the estimate from its true value. Because $\vec{P}_L$ is directly unobservable we must use its estimate; the procedure for estimating it will be described soon. The mechanical response of the stage hits a noise limited measurement floor at 550 Hz. Thus the stage-sensor signals beyond 550 Hz contain little true motion information and are dominated by electrical noise, so we digitally filter the stage sensed positions with a 600 Hz low pass cutoff.

3.3 In-situ estimation of F_{QP} for each probe of interest

Because $\vec{P}_L$ cannot be measured without knowing F_{QP}, each experiment must start by estimating F_{QP}. Also, because the position feedback cannot be initiated without being able to measure $\vec{P}_L$, the first estimate of F_{QP} is always when position feedback is not operational. We will refer to this kind of estimation as offline estimation, as opposed to on-the-fly estimation, which refers to the case where estimation is performed while position feedback is operational.

We inject perturbations in the probe position relative to laser and fit a parametric model of F_{QP} to the data that is acquired during perturbations. This section will describe engineering details, i.e., various schemes of perturbing the position of the probe, various types of perturbation signals, and various types of parametric models that could be chosen.

3.3.1 Selection of a parametric model

We assume that the true mapping function from QPD signals to position is continuous and differentiable within operable neighborhood. Thus according to the Stone-Weierstrass theorem [61], the mapping could be approximated by a polynomial with arbitrary accuracy. Consequently, we chose polynomials in QPD signals as the structure of F_{QP}. Polynomial regression, when using natural variables as the regressors, may suffer from *near collinearities* (high correlation coefficients) between regressor variables. Centralizing the regressor variables (removing mean values) removes most of the collinearities for polynomials of up to 2nd order. For polynomials of higher order, a more complicated approach is required that maps natural polynomial variables into orthogonal polynomial variables [62]. From the volumetric-raster-scan data for an ensemble of probes, we observed that the coefficients of the polynomials do not change by a significant amount beyond 2nd order, especially for 200 nm; hence we limited the polynomial structure to 2nd order. Thus, F_{QP} is a group of three polynomials, one for each axis:

$$F_{QP_x}: P_{Lx}\left(Q'_1,...,Q'_4\right) = \sum_{i=1}^{4}\left[\beta_i^x Q'_i + \sum_{j=i}^{4}\beta_{ij}^x Q'_i\, Q'_j\right] \qquad \text{Equation 3.2}$$

Where, $Q'_k = Q_k - \mu\left[Q_k\right] = Q_k - Q_k^0$

3.3.2 Schemes for perturbing the probe position relative to laser

The options we have for perturbing the probe position can be divided into two broad categories:

1. Move the whole specimen relative to the laser beam, or vice versa. Examples: move the specimen-mounting stage; move the laser beam itself.
2. Move only the probe of interest relative to the laser beam. Examples: pull a magnetic bead with magnets; trap a bead using a second high-power laser and move the trap inside the detection laser.

Each method has its advantages and limitations. Method 1 is instrumentation-wise simpler, requiring only a calibrated 3-axis stage (or calibrated actuators to steer the beam). Method 1 is also versatile, applicable to a wide variety of probes (magnetic or nonmagnetic beads, organelles etc), as long as the probe produces a detectable scattering signal. On the downside, the background moves with the probe; so the estimated response ($\widehat{F}_{QP}$) is the sum of the response to the probe motion and the response to the background motion. Thus, depending upon how strongly the background contributes to the total scattering, an error is introduced in the measurements. In the extreme case, if the background-scattering signal dominates over the probe-scattering signal, method 1 is of little use. However, we have observed that beads and organelles larger than 300 nm normally produce a sufficiently large scattering signal even with a live cytoplasm as the environment.

In method 2, only the probe of interest moves relative to the laser while the environment stays unperturbed, thus background scattering does not contaminate the estimate $\widehat{F}_{QP}$. However, the approach of moving the probe relative to its environment itself could be a severe limitation. Motion of the probe in response to the actuator signal is affected by the viscoelastic properties of the environment. Thus, the viscoelastic properties of the environment must be known a priori in order to map the actuator signals into probe positions relative to specimen. Paradoxically but quite frequently, the ultimate goal of an experiment may be to investigate the viscoelastic properties of the specimen. This is particularly true when the environment is a live cytoplasm. Moreover, method 2 requires sophisticated instrumentation while it is less versatile compared to method I. Use of magnets as the actuator requires magnetic beads as the probe, while use of optical trap requires probes that can be trapped (e.g., particles with a uniform refractive index throughout the body).

We chose method 1 and used a pre-calibrated, 3-axis, specimen-mounting stage for moving the specimen relative to the laser.

3.3.3 Formulation of regression equations for offline estimation of F_{QP}

We will write the RHS of Equation 3.2 in a compact, vector-multiplication form as,

$$F_{QP_x} : P_{Lx}\left(Q'_1,...,Q'_4\right) = \overline{\beta}^x \times \overline{R} \qquad \text{Equation 3.3}$$

Where,

$\overline{\beta}^x$ = Regression-coefficient vector

$\overline{R}$ = Regressor-variable vector, that contains all Q' terms in Equation 3.2

Because the specimen is mounted on the stage, the position of the probe relative to laser ($\vec{P}_L$) is a vector sum of the position of stage relative to laser ($\vec{S}_L$) and the position of probe relative to stage ($\vec{P}_S$). Using these facts and notations, we can construct the block diagram for offline estimation of F_{QP} as shown in Figure 3-2. Note that the F_{PQ} block bundles up several physical processes, i.e. scattering, interference, and light detection by QPD. Naturally, the true F_{PQ} is unobservable.

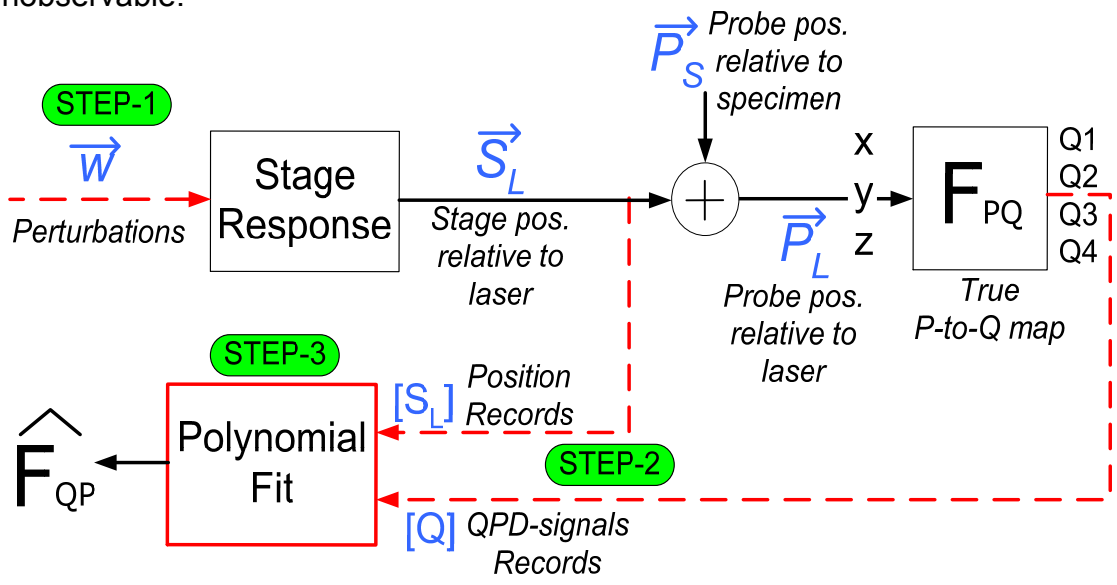

Figure 3-2: Block diagram of F_{QP} estimation procedure (offline)

Using the block diagram, we can rewrite Equation 3.3 in terms of observable signals, i.e., $\vec{S}_L$ and $\vec{P}_L$. From the right-most summer junction we can write,

$$\vec{S}_L(t) = \vec{P}_L(t) - \vec{P}_S(t)$$

Substituting the expression for $\vec{P}_L$ from Equation 3.3, we write the regression equation as:

$$\vec{S}_L(t) = \overline{R}(t)\overline{\beta} + \vec{\varepsilon}'(t) - \vec{P}_S(t)$$

$$\vec{S}_L(t) = \overline{R}(t)\overline{\beta} + \vec{\varepsilon}(t)$$ Equation 3.4

Where,

$\vec{\varepsilon}'(t)$ = noise, deviations of the polynomial model from the true F_{QP}

$\vec{\varepsilon}(t) = \vec{\varepsilon}'(t) - \vec{P}_L(t)$ = the error term for regression procedure

From Equation 3.4, the least-square estimate of coefficient vector $\overline{\beta}$ is given by [63]

$$\widehat{\overline{\beta}} = \left(\overline{\mathbf{R}}^T\overline{\mathbf{R}}\right)^{-1}\overline{\mathbf{R}}^T\mathbf{S}_L$$ Equation 3.5

Where $\overline{\mathbf{R}}$ and $\mathbf{S}_L$ are the matrices comprised by stacking $\overline{R}(t)$ and $\vec{S}_L(t)$ for different values of t in each row. Once $\widehat{\beta}$ is computed, the position of the probe relative to laser is estimated as:

$$\widehat{\vec{P}}_L(t) = \widehat{\beta} \times \overline{R}(t)$$ Equation 3.6

Note that before application of Equation 3.6, the QPD signals must be centralized by the same Q^0 that was used to centralize the regressor variables in Equation 3.2.

3.3.4 Design of perturbation signals for offline estimation of F_{QP}

Design of perturbation signals involves choosing type, amplitude and duration. Selection of type is driven by two primary criteria:

1. The perturbations should be uncorrelated with the probe motion relative to the specimen coordinate frame ($\vec{P}_S$). As seen from Equation 3.4, the error term for the regression procedure includes probe position relative to the specimen. As one of the assumptions of linear regression, the error term must be uncorrelated with the output variable (i.e., $\vec{S}_L$).

2. The three perturbation sequences, one for each axis, should be uncorrelated with each other. This facilitates estimation of F_{QP} for all three axes simultaneously.

For offline estimation, we chose three statistically-independent pseudo-random sequences as the perturbations because they satisfy both criteria listed above. It is known that the true F_{QP} is single-valued only within a small region of the beam waist; the size of that region (200 to 300 nm) sets an upper bound to the perturbation amplitude. Within this limit, higher amplitude of perturbations is always preferred because that provides a larger operable neighborhood, thus allowing for larger excursions of the bead at bandwidth beyond the capabilities of the feedback-loop. Typically, we set the amplitude of perturbations to 100 nm, giving 200 nm as the size of the operable neighborhood. Using regression Equation 3.5 and Equation 3.6, it can be shown that [Appendix A]

$$\sigma^2\left[\hat{\beta}_k^x \middle| \overline{R}_k\right] = \frac{\sigma^2\left[\overline{\varepsilon}'_x \middle| \overline{R}_k\right] + \sigma^2\left[\overline{P}_{Sx} \middle| \overline{R}_k\right]}{\sum_{n=0}^{N} R_{k\langle n\rangle}{}^2} \qquad \text{Equation 3.7}$$

Where,

$\hat{\beta}_k^x$ = Estimated kth element of the regression-coefficient vector β^x

$\overline{R}_k$ = kth column of the regressor matrix $\overline{\mathbf{R}}$

P_{Sx} = x-axis component of the motion of the probe relative to specimen

N = Number of data points used for estimation

Equation 3.7 expresses the variance of the estimated coefficient in terms of system noise, probe motion relative to specimen, amount of data, and variance of corresponding regressor variable. For a linear F_{QP}, because $R_k \propto \vec{W}$

the denominator of Equation 3.7 increases quadratically with the perturbation amplitude. Thus, in addition of larger operable neighborhood, higher perturbation amplitudes also produces more precise estimate of F_{QP}. Also, as indicated by the N-point summation in the denominator, longer perturbation durations would give more precise estimates of the coefficient. However, for offline estimation, longer durations may let the probe diffuse out of the single-valued region. Thus, for significantly mobile probes, keeping the duration of perturbations as short as possible is preferable.

Also, the only inescapable goal of offline estimation is to be able to initiate a stable position feedback. Because a feedback loop usually operates with a sufficient gain margin, scaling-type error in the estimate of F_{QP} is tolerable for maintaining a stable feedback. At system noise of approximately 10 nm RMS, for probes moving with velocities up to approximately 1 μm/S, we were able to achieve stable feedback using perturbations of 0.1 second duration. For probes that move faster than 1 μm/S, bright-field video can be used to initiate a low-bandwidth 2D position feedback to keep the probe centered within the beam while the agnostic solver is acquiring data for the first offline estimate of F_{QP}.

Once an estimate of F_{QP} is available and position feedback is initiated, the user has an option to perform on-the-fly estimation, which would be explained later. As will be shown, when feedback is operational, one can get around the nuisances of uncontrolled external disturbance ($\vec{P}_S$), which allows for long-duration perturbations, thus producing a better estimate of F_{QP}.

3.4 Operation of position feedback

Once an estimate of F_{QP} is available, the position of the probe relative to laser can be estimated and thus position feedback can be initiated. The block diagram in Figure 3-3 shows the operation of the position-feedback loop. Note that as shown in the block diagram, the PI controller moves the specimen-translation stage in order to keep $\hat{\vec{P}}_L$ as close to the set-point $\vec{R}_L$ (which is usually zero) as possible.

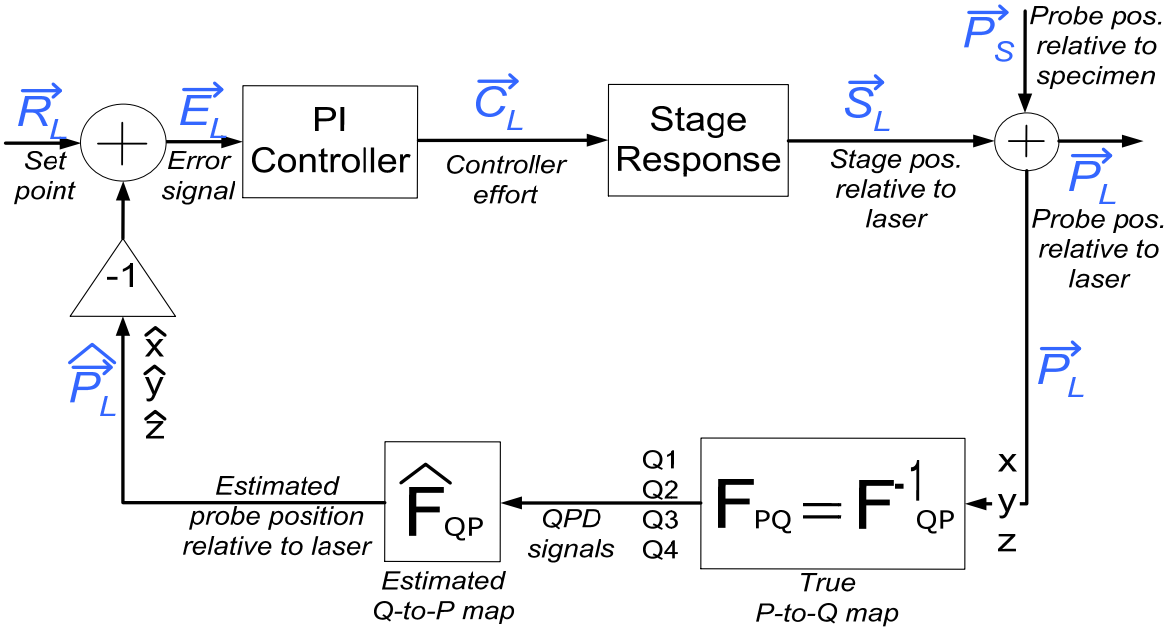

Figure 3-3: Block diagram of the position-feedback system

Chapter 4 On-the-fly estimation of F_{QP}

I mentioned in chapter 2 that there are primarily two motivations for reestimating F_{QP}:

1. In order to account for the variations in the true F_{QP} caused by change in the ambient refractive index.
2. To be able to optimize the sensitivity of the detector by dynamically adjusting the location of the probe within the beam.

Because position feedback is usually incorporated for tracking long range motions of the probe, the re-estimation of F_{QP} must be performed while the feedback is operational. We will refer to this type of estimation as on-the-fly estimation. From the scientist's point of view, it is highly desirable that on-the-fly estimation procedure neither forces interruption of the on-going experiment nor causes any corruption in the acquired stream of data. In this chapter, we will understand the challenges that these goals pose, and their solutions.

4.1 Feedback-controller interferes with the perturbation signals

Figure 4-1 presents the block diagram for on-the-fly estimation; which is constructed by merging the offline estimation block diagram presented in Figure 3-2 and the position feedback loop presented in Figure 3-3.

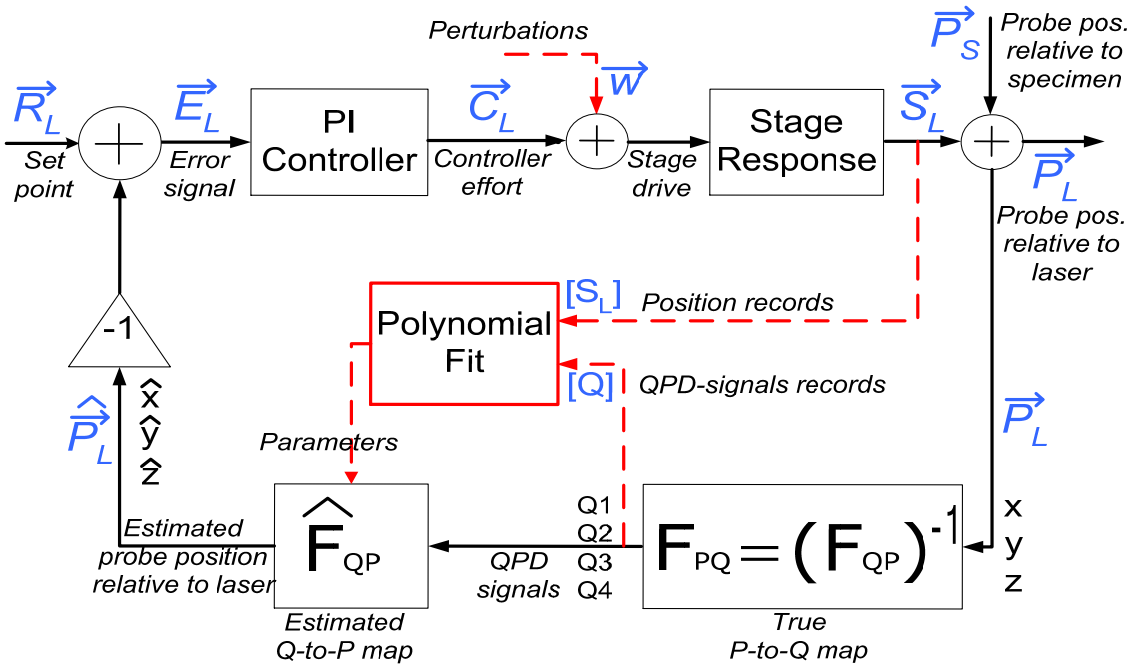

Figure 4-1: Block diagram of on-the-fly estimation

As seen from the block diagram of Figure 4-1, if perturbations are applied while in feedback, the measured stage position is the combination of the stage response to two signals: feedback-controller effort, and perturbations. By design, the controller effort tends to compensate for and cancel out the probe motion relative to the laser. This function of an actuator to suppress the external disturbance has interesting implications from a system-identification point of view. Let us ignore the perturbation signal for the moment and theoretically investigate how much of $\vec{P}_S$ transmits through the feedback loop and is visible into $\vec{P}_L$.

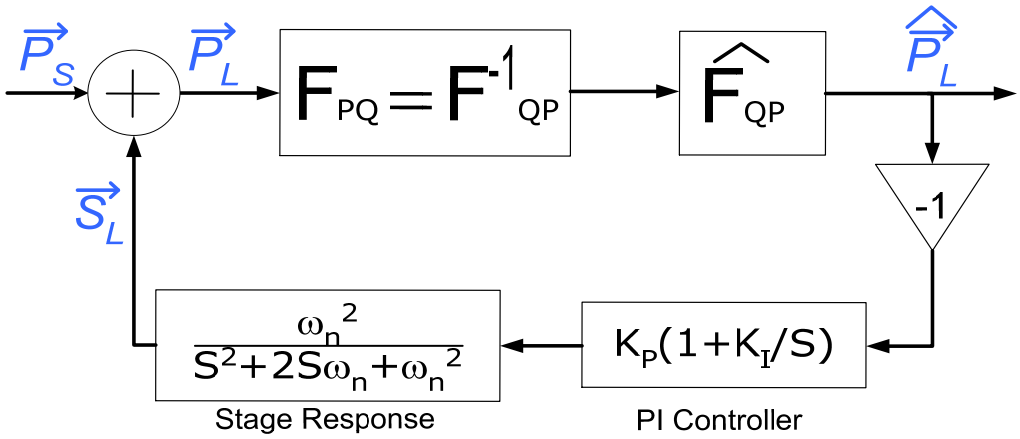

(a)

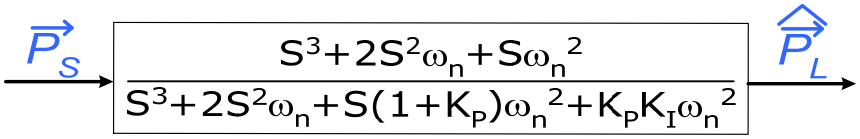

(b)

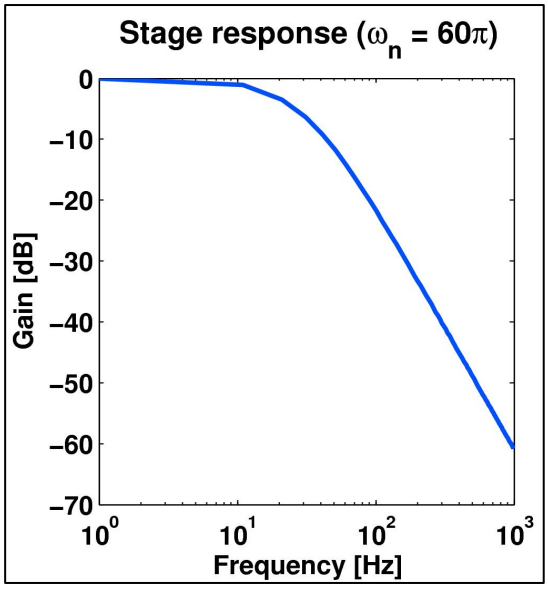

(c)

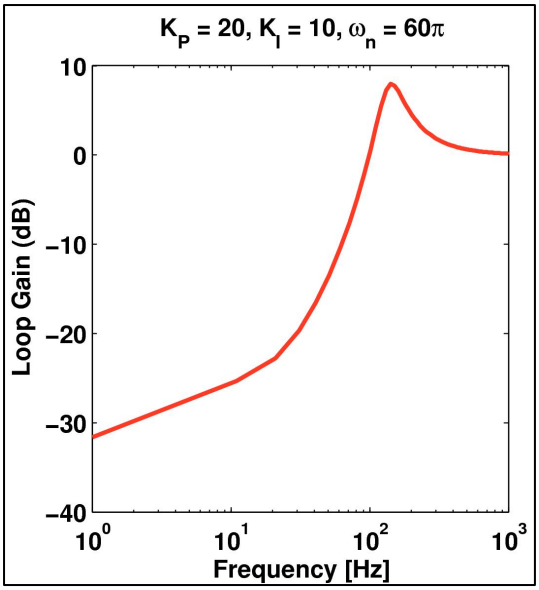

(d)

Figure 4-2: Transfer function from P_S to P_L

Figure 4-2(a) depicts the block diagram of the position-feedback loop rearranged such that $\vec{P}_S$ is the input and $\vec{P}_L$ is the output. The stage response is approximated by a critically-damped 2-pole model. Figure 4-2(b) shows the

equivalent closed-loop transfer function assuming ideal estimate ($\widehat{F}_{QP} = F_{PQ}^{-1}$). Figure 4-2(c) shows the frequency-response of the 2-pole-model for the stage, computed using the Matlab command *freqresp*. Figure 4-2(d) shows the amplitude (gain) response of the closed-loop transfer function, also computed using *freqresp*. As seen, the feedback loop acts mostly as a high-pass filter suppressing low-frequency components of $\vec{P}_S$ from transmitting into $\vec{P}_L$.

From the summer junction of Figure 4-2(a)

$$\vec{P}_L(t) = \vec{S}_L(t) + \vec{P}_S(t) \qquad \text{Equation 4.1}$$

If we let $H(\tau)$ represent the closed-loop transfer function from $\vec{P}_S$ to $\vec{P}_L$; we can write:

$$\begin{aligned} &\vec{P}_S(t) * H(\tau) = \vec{S}_L(t) + \vec{P}_S(t) \\ \Leftrightarrow\ &\vec{S}_L(t) = \vec{P}_S(t) * \left[H(\tau) - 1\right] \end{aligned} \qquad \text{Equation 4.2}$$

Based on the equations for $\vec{P}_L$ and $\vec{S}_L$, and using the fact that the power-spectral-density (PSD) function of a particle diffusing inside a Newtonian fluid exhibits negative 2 slope; a frequency-domain comparison is sketched in Figure 4-3. Note that, as shown in the inset, the simplified stage response model is adjusted to capture the salient features of the MCL stage response. As shown in the sketch, the within-loop-bandwidth components of the external disturbance ($\vec{P}_S$) are compensated by the motion of the actuator driven in feedback; thus they are absent in the PSD of the sensed-position signal ($\vec{P}_L$) but appear in the PSD of the actuator signal ($\vec{S}_L$) instead. Immediately beyond the cutoff frequency of the feedback loop is a transition zone, where part of the external disturbance is compensated by the stage motion, while most of the external disturbance

transmits into the sensed-position signal ($\vec{P}_L$). The transition zone continues until the stage motion hits the noise floor, after which any external disturbance goes through the feedback loop unchecked, and thus fully appears in the sensed-position signals. The fact that the relation between $\vec{P}_L$ and $\vec{S}_L$ is not linear or straight forward suggests that the regression procedure for on-the-fly estimation is not as simple as that for offline estimation.

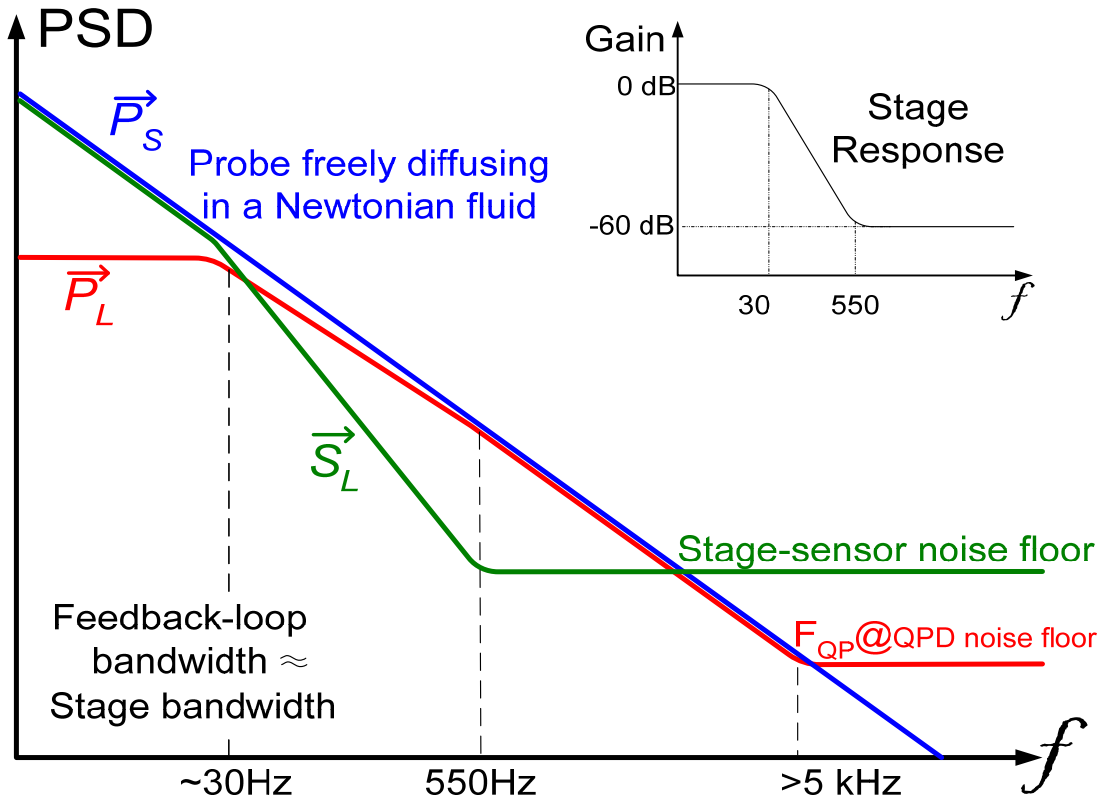

Figure 4-3: Frequency-domain comparison sketch [not drawn to scale]

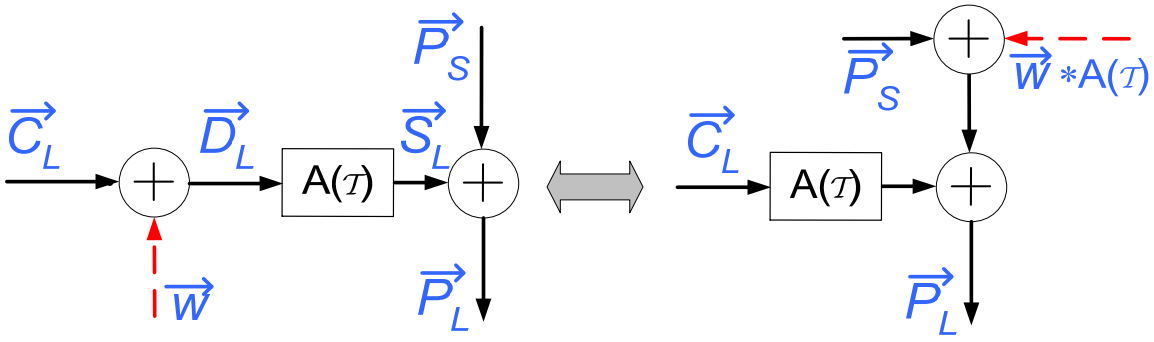

Figure 4-4: For the feedback loop, perturbation is an external disturbance

Let's look into this issue more formally; we need to formulate the regression equation in terms of observable signals. As in the offline estimation case, we will first try to express the unobservable $\vec{P}_L$ in terms of the observable $\vec{S}_L$. Let $A(\tau)$ represent the impulse response of the stage. Figure 4-4 shows two ways of representing how perturbations are injected. Using block-diagram-manipulation principles, we can transform one representation into the other and vice versa. As seen from the diagram on the right, perturbations can be thought of as a part of the external disturbance that the feedback loop tends to suppress. Thus we can write

$$\vec{P}_L(t) = H(\tau) * \left[\vec{P}_S(t) + A(\tau) * \vec{W}(t) \right] \qquad \text{Equation 4.3}$$

Also, algebraically equating the signals at the summation junction,

$$\vec{P}_S(t) = \vec{P}_L(t) - \vec{S}_L(t) \qquad \text{Equation 4.4}$$

Substituting Equation 4.4 into Equation 4.3,

$$\vec{P}_L(t) = H(\tau) * \left[\vec{P}_L(t) - \vec{S}_L(t) + A(\tau) * \vec{W}(t) \right]$$

$$\vec{P}_L(t) * \left[H(\tau) - 1 \right] = H(\tau) * \vec{S}_L(t) - H(\tau) * A(\tau) * \vec{W}(t)$$

$$\vec{P}_L(t) = \frac{H(\tau)}{H(\tau) - 1} * \left[\vec{S}_L(t) - A(\tau) * \vec{W}(t) \right] \qquad \text{Equation 4.5}$$

As seen from Equation 4.5, without knowledge of $H(\tau)$ and $A(\tau)$, $\vec{P}_L$ is not expressible as a linear combination of $\vec{S}_L$ and an uncorrelated error term. In practice, $A(\tau)$ may depend on several parameters, e.g., mechanical loading, temperature, etc; while $H(\tau)$ depends on $A(\tau)$ and the rate of the feedback loop (which is usually variable if the controller is programmed on a conventional operating system). In the most rigorous approach, $A(\tau)$ could be estimated on-the-fly using correlation between the input-output records of the stage. However, that approach requires complex mathematics as well as an ability to synchronize stage drive with stage sensor readings. Fortunately, if we make an assumption about the nature of F_{QP}, there is a simpler solution.

4.2 Memoryless-system assumption

If we assume that the QPD signals at any moment do not depend on past probe positions, then the mapping F_{PQ} (and thus F_{QP}) is memoryless and thus frequency independent. The assumption is valid up to the bandwidth of the sensor (QPD) which has been reported to be as high as 1 MHz [64]. If F_{QP} is frequency independent, we can restrict the perturbations to a single frequency and still be able to fully identify F_{QP}. Moreover, the stage positions associated with sinusoidal perturbations can be accurately extracted by correlating the measured stage positions with a sinusoidal template of prescribed frequency. Thus, no knowledge of the loop transfer function or the impulse response of the stage is necessary. Also, statistical independence among the perturbation sequences can be easily achieved by selecting three coprime numbers as the

frequencies of the sinusoids. Thus, sinusoidal perturbations drastically simplify the estimation algorithm.

4.3 Regression equations for on-the-fly estimation

Because the regression process is identical for three axes, we will limit the discussion to the x axis only. First we will see how to separate stage sensed positions into perturbations and controller effort. Because perturbations are sinusoidal, assuming that stage response is linear, we can write:

$$W_x * A^x(\tau) * H^x(\tau) = k_w^x \sin\left(2\pi f_w^x t + \phi_w^x\right) \qquad \text{Equation 4.7}$$

Where,

f_w^x = frequency of the perturbation sinusoid for x axis

k_w^x = amplitude of the perturbation sinusoid after feedback suppression

ϕ_w^x = phase of the perturbation sinusoid after feedback suppression

Here, k_w and ϕ_w are the unknown parameters. We can find both by correlating stage positions with sinusoid templates. If t_s is the sample-interval, and N is the total number of data points used for the estimation process, we can make a sinusoid template as

$$T_{x\sin} = \sin\left(2\pi f_w^x n t_s\right) \qquad n = 0,1,2,....,N$$

If we define the correlation function between quantities A(n) and B(n) as,

$$\Re_{A,B}[\phi] = \sum_{n=0}^{N}\left(A(nt_s) - \mu[A]\right)\left(B(nt_s + \phi) - \mu[B]\right)$$

Then, the delay is estimated as

$$\hat{\phi}_w^x = \arg\max_{\phi}\left(\Re_{S_{gx},T_{x\sin}}\left[\phi\right]\right)$$ Equation 4.8

The original sinusoidal template is then adjusted for the delay.

$$T_{x\sin}^{\phi} = \sin\left(2\pi f_w^x n t_s + \hat{\phi}_w^x\right) \qquad n = 0,1,2,....,N$$

Then, the estimated amplitude of perturbations is given by

$$\hat{k}_w^x = \frac{\Re_{S_{gx},T_{x\sin}^{\phi}}\left[\phi = 0\right]}{\Re_{T_{x\sin}^{\phi},T_{x\sin}^{\phi}}\left[\phi = 0\right]}$$ Equation 4.9

Substituting expressions for k_w^x and ϕ_w^x into Equation 4.7, we can accurately determine how much of the perturbation component is visible in $\vec{P}_L$ after feedback suppression. Thus Equation 4.3 can be written as

$$\vec{P}_L(t) = \vec{P}_S(t) * H(\tau) + \vec{W}(t) * A(\tau) * H(\tau)$$

$$\vec{P}_L(t) = \vec{P}_S(t) * H(\tau) + \hat{k}_w \sin\left(2\pi f_w t + \hat{\phi}_w\right)$$

Rearranging and considering only the X axis,

$$\hat{k}_w^x \sin\left(2\pi f_w^x t + \hat{\phi}_w^x\right) = P_{Lx}(t) - P_{Sx}(t) * H^x(\tau)$$

$$\hat{k}_w^x \sin\left(2\pi f_w^x t + \hat{\phi}_w^x\right) = \overline{R}(t)\overline{\beta}^x + \varepsilon_x(t)$$ Equation 4.10

Where the error term for the regression equation is given by

$$\begin{aligned}\varepsilon_x(t) &= \varepsilon_x'(t) - P_{Sx}(t) * H^x(\tau) \\ &= \varepsilon_x'(t) - p_x(t)\end{aligned}$$ Equation 4.11

Where,

$\varepsilon_x'(t)$ = error due to deviations of the polynomial model from the true F_{QP};

$$p_x(t) = P_{Sx}(t) * H^x(\tau)$$

As shown in appendix A, the variance in the estimate of coefficients is given by

$$\sigma^2\left[\hat{\beta}_k^x \middle| \overline{R}_k\right] = \frac{\sigma^2\left[\overline{\varepsilon}'_x \middle| \overline{R}_k\right] + \sigma^2\left[\overline{p}_x \middle| \overline{R}_k\right]}{\sum_{n=0}^{N} R_{k\langle n\rangle}{}^2}$$

Equation 4.12

Here the second term in the numerator has changed from $\sigma^2\left[\overline{P}_{Sx} \middle| \overline{R}_k\right]$ for the offline case to $\sigma^2\left[\overline{p}_x \middle| \overline{R}_k\right]$ for the on-the-fly case. Because $p_x(t)$ is obtained by applying the filter $H^x(\tau)$ to $P_{Sx}(t)$, $\sigma^2\left[\overline{p}_x \middle| \overline{R}_k\right]$ is smaller than $\sigma^2\left[\overline{P}_{Sx} \middle| \overline{R}_k\right]$. Thus, if the probe is highly mobile, the on-the-fly estimation will be more precise.

4.4 Design of perturbation signals for on-the-fly estimation of F_{QP}

From the previous discussion, we know the type of perturbation suitable for the on-the-fly estimation, i.e. sinusoidal. The remaining choices are of frequency, amplitude, and duration.

As we saw in Figure 4-4, the perturbations are also subject to suppression by the feedback loop, so the selected frequencies should be outside the bandwidth of the feedback loop. The loop-bandwidth is limited by the response of the stage, in our case at approximately 30 Hz. Also, our stage exhibited mechanical resonance at around 250 Hz, so it was preferable for the perturbation frequencies to be as far below 250 Hz as possible. Also, the frequencies should be coprime so that perturbations are statistically independent and we can

estimate F_{QP} for all three axes simultaneously. Clearly, several combinations of frequencies could satisfy these constraints. We chose 67, 61, and 53 as the perturbation frequencies for x, y, and z axis respectively.

The amplitude of the perturbations for on-the-fly estimation shares all the constraints of offline estimation. In addition, there is a weak preference for the perturbation amplitude not to be greater than that used for the last estimation session. Need for this constraint can be appreciated if we realize that we possess knowledge of F_{QP} only in a local region that is defined by the *operable neighborhood*. Validity of the estimated F_{QP} outside the operable neighborhood is simply unknown, and because of its nonlinear nature it is possible that the true F_{QP} departs significantly from the polynomial model that was fit. In that case, if the perturbations for the next estimation session drive the probe outside the operable neighborhood, the exponential nature of the polynomial model may produce position estimates that are unrealistically large; thus making the feedback-controller unstable and disrupting the experiment. As a separate note, by perturbation amplitude I refer to the motion that is visible in $\vec{P}_L$ after feedback suppression, i.e., the amplitude of $\vec{W} * A(\tau) * H(\tau)$. Thus to produce perturbations of desired amplitude, the amplitude of the drive signal $\vec{W}$ in Figure 4-1 must be amplified to account for the suppression by $A(\tau) * H(\tau)$.

The duration of perturbations for on-the-fly estimation has virtually no upper bound. Because, unlike the offline case, we are not limited by the time before which the probe moves out of the single-valued region. However, when the background itself is highly volatile, true F_{QP} may change rapidly. In this case, F_{QP} must be estimated at a bandwidth that is high enough to keep up with the

variations of F_{QP}. The need for higher estimation bandwidth may put the upper bound on the durations of perturbations. However, conceptually, it is also possible to continuously inject perturbations while estimating F_{QP} in parallel when needed, by employing recursive stochastic estimators e.g. Kalman filter [65-67]. Because experiments reported in this thesis did not demand high bandwidth updates of F_{QP}, we did not pursue that line of thought.

In this chapter we saw that F_{QP} can be estimated without interrupting the on-going experiment and that on-the-fly estimation can produce more precise estimates of F_{QP} compared to offline estimation. In the next chapter we will see experimental results evaluating the performance of agnostic tracking.

Chapter 5 Performance evaluation of Agnostic Tracking

In chapter 3 and chapter 4, we saw how to estimate F_{QP} offline as well as while operating in feedback. This chapter is concerned with evaluating how well those estimation procedures work.

5.1 Testing the memoryless-system hypothesis

In chapter 4, we made an assumption that the system under consideration is memoryless, that is, the QPD signals at any moment do not depend on past probe positions. Clearly, this is true only insofar as QPD response can be considered instantaneous; so, for frequencies beyond the QPD bandwidth limit, this assumption will fall apart. We tested the validity of the assumption by correlating probe position with QPD signals.

A micron-size bead was immobilized with respect to the specimen and was put in the focus of the laser. The specimen-translation stage was driven with band-limited white noise signals (generated digitally using Matlab routine *rand*). Stage positions (reported by sensors) and QPD signals were recorded at 10 kHz using a single ADC board. Stage position and QPD signals were then cross-correlated (using Matlab routine *xcorr*) and plotted. Using the same experiment, we also found results that supported the assertion that simple analytical models for QPD response have limitations. Figure 5-1 shows two different cases. In the

plot on the right, two of the correlation peaks are positive while two of the correlation peaks are negative; suggesting that F_{QP} *(x)* happens to resemble the simplest analytical model where position is given by distributing a quadrant into two pairs and then taking the difference of the QPD signals between the two pairs [36, 37]. However in the plot on the left, three peaks are positive and only one peak is negative, thus position cannot be computed by simply taking differences between two pairs of the quadrants. We have observed many other combinations of peak polarities, and the case on the left is just as likely to be encountered as the case on the right.

It is encouraging, however, that the peak of correlation occurs always at zero (±0.1 ms) lag. This is true for all four quadrants of the QPD. The zero lag correlation suggests that there is no measurable lag between a change in position and a change in QPD signals. In other words, for the sampling rate of interest (i.e. 10 kHz), F_{PQ} (and thus F_{QP}) can be safely considered a memoryless system.

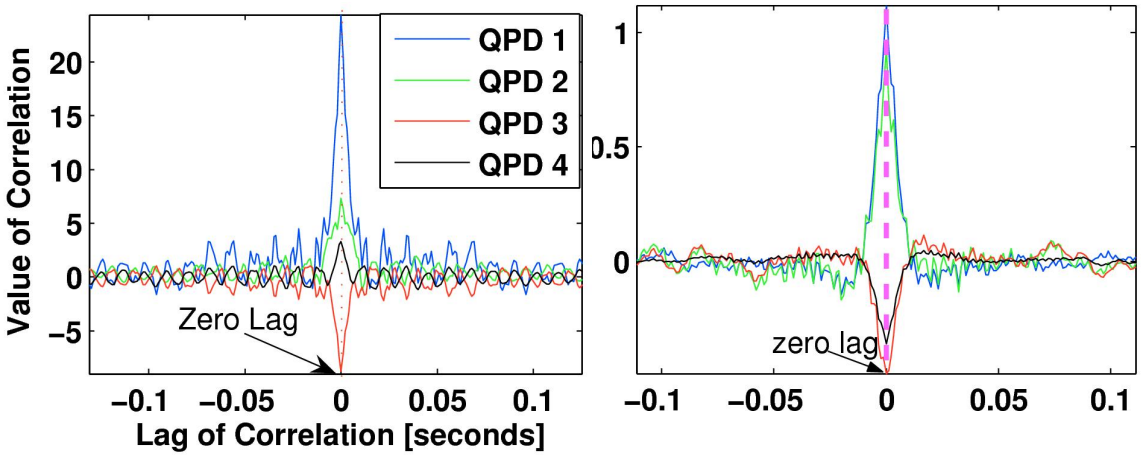

Figure 5-1: Correlation between position and QPD signals

5.2 Viscosity calibration using Agnostic Tracking

A minute particle suspended in a fluid constantly experiences random collisions due to thermal energy of the surrounding fluid molecules. As a result the particle randomly moves around in the fluid, or in other words, exhibits Brownian diffusion [68, 69]. By applying the Stokes-Einstein relationship to the observed motion of the particle, the viscoelastic modulus of the fluid can be extracted [70]. Or in other words, if the viscoelastic modulus of the fluid is known, the accuracy of the position-tracking technique can be determined by comparing the estimated values with the known standards. I used 2M sucrose solution at room temperature as the calibration standard. An ensemble of 14 paramagnetic, 1 μm diameter beads diffusing freely in 2M Sucrose solution was tracked using Agnostic Tracking. Figure 5-2 shows the 3D trajectories of the beads.

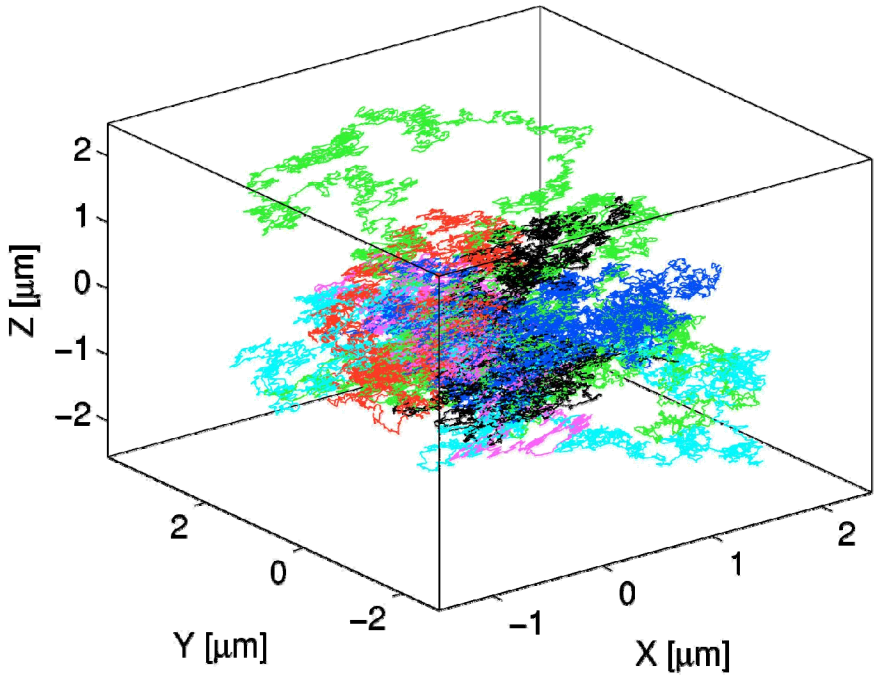

Figure 5-2: 3D diffusion trajectories for an ensemble of beads

The 3D Mean-squared-displacement (MSD) was computed as a function of window span (τ) using the following equation:

$$\left\langle \Delta r^2(\tau) \right\rangle = \frac{1}{T}\sum_{t=0}^{t=T}\left[r(t+\tau) - r(t) \right]^2$$

The MSD analysis was carried out on three signals, bead position relative to specimen (solid blue), bead position relative to laser (solid red) and stage position (dotted green).

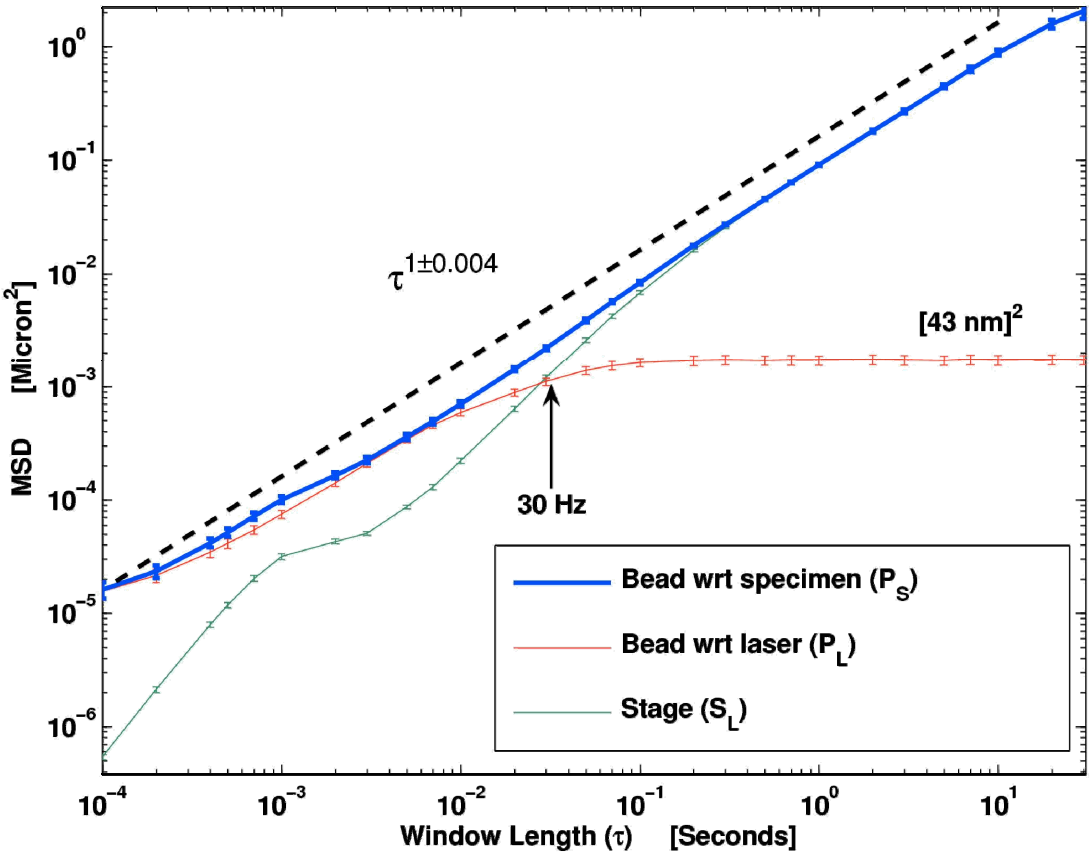

Figure 5-3: MSD analysis for free diffusion in a Newtonian fluid

Figure 5-3 shows the MSD analysis for one of the 14 beads, whereas the error bars represent standard error over the whole ensemble. The MSD of the bead position relative to specimen closely follows the unity-power law (0.997 ±

0.004) for the whole range of τ, as expected for free diffusion in a Newtonian fluid [10]. Also, using Stokes-Einstein relationship, we obtained the estimated viscosity of 0.021 ± 0.001 Pa-S, which is in excellent agreement with the theoretical value 0.0212 Pa-S at room temperature (298 K) [71]. The agreement between established standards and measured values implies that the position-measurement bandwidth is at least as high as the sampling rate, i.e.,10 kHz.

Several other important observations can be drawn from the plot. Firstly, the MSD of the bead position relative to laser exhibits a plateau for longer time scales (> 0.03 s); but the MSD of the stage position closely follows the MSD of the bead position relative to specimen, which is expected because the position feedback controller constantly attempts to keep the probe centered in the laser by moving the specimen-translation stage in a way to compensate for and cancel out the probe position relative to specimen. Thus the diffusive motion at longer time scales is suppressed from probe position and is reflected in the stage position instead. Secondly, for shorter time scales (< 0.01 s), the MSD of the bead position relative to laser closely follows the MSD of the bead position relative to specimen; while the MSD of the stage position rolls off, which is also expected considering that the bandwidth of the specimen translation stage is limited to about 30 Hz. When the stage is unable to move, the diffusive motion leaks through the feedback loop and is visible in the probe motion relative to laser. The frequency limit beyond which the feedback is unable to compensate for the probe motion relative to specimen is manifested by the crossover between the red and the green curve. The occurrence of the cross over suggests that the bandwidth of the feedback loop is around 30 Hz.

5.3 Evaluating performance of on-the-fly estimation

It is natural for a scientist to ask two questions: one, how accurate is the on-the-fly estimation; and two, how invasive to the experimental data are the perturbations that were injected for on-the-fly estimation. We will first see that the two questions are closely related and are two different ways of asking for the same information. Later we will see an experimental result answering the question. Let us refer to the sketch of Figure 3-1. Here $\vec{P}_S$ is the primary measurement of scientific interest. Let us investigate what happens when we add perturbations into the stage position. Let's denote λ as the perturbations injected in the state position, so $\lambda(t) = W(t) * A(\tau) * H(\tau)$. Reproducing Equation 3.1:

$$\widehat{\vec{P}}_S = \widehat{\vec{P}}_L - \vec{S}_L$$

If we inject perturbations into the stage position,

$$\vec{S}_{L-pert} = \vec{S}_L + \vec{\lambda}$$

If we assume negligible slosh at this scale, the probe moves with the specimen, and thus with the stage. So, perturbations in $\vec{S}_L$ cause identical perturbations in $\vec{P}_L$. So,

$$\vec{P}_{L-pert} = \vec{P}_L + \vec{\lambda}$$

In the ideal case where $\vec{P}_L = \widehat{\vec{P}}_L$

$$\widehat{\vec{P}}_{L-pert} = \widehat{\vec{P}}_L + \vec{\lambda}$$

Substituting back into the original equation,

$$\begin{aligned}\hat{\vec{P}}_{S-pert} &= \hat{\vec{P}}_{L-pert} - \vec{S}_{L-pert} \\ &= \hat{\vec{P}}_L + \vec{\lambda} - \vec{S}_L - \vec{\lambda} \\ &= \hat{\vec{P}}_S\end{aligned}$$

Thus, injecting small perturbations in the stage position should not cause any change in the measurement of probe position relative to specimen. However, it is important to note that the conclusion is based on two assumptions:

1. There is no or negligible slosh. In other words, the inertia of the probe is negligible.
2. The estimate of probe position relative to laser is ideal, i.e., $\hat{\vec{P}}_L = \vec{P}_L$

We ignore the electrical noise present in the measurement of the signals, assuming that it is uncorrelated with the perturbations. Thus, if injecting perturbations increases the error in $\hat{\vec{P}}_S$, the additional error can only be attributed to a violation of one or both of the assumptions above. Because we assume that the amount of electrical noise in the measured QPD signals is unaffected due to perturbations, an additional error in $\hat{\vec{P}}_L$ can only be attributed to an inaccuracy in the $\hat{F}_{QP}$ that was obtained recently on the fly. In this section we seek to characterize the part of the error in $\hat{\vec{P}}_S$ that is caused due to perturbations injected. The characterization will give a pessimistic estimate of the error in the on-the-fly $\hat{F}_{QP}$ because slosh is the potential source of error being ignored.

Because $\hat{\vec{P}}_S$ and λ share the same dimension, i.e. displacement, we can think of a linear, memory-less transfer-function that has perturbations at the input and the additional error in $\hat{\vec{P}}_S$ at the output. Because the transfer-function is

linear, the additional error must be correlated with the perturbations. This leads us to a method for determining the error caused due to perturbations.

Let's say f denotes a *leakage factor* -- the error that is introduced due to perturbations represented as a fraction of the perturbation amplitude. Considering only one axis, we can write:

$$\hat{P}_{S-pert} = \hat{P}_{S-nopert} + f\,\lambda$$

$$\Rightarrow \Re_{\tau=0}\left(\hat{P}_{S-pert}, \lambda\right) = \Re_{\tau=0}\left(\hat{P}_{S-nopert}, \lambda\right) + f\Re_{\tau=0}\left(\lambda, \lambda\right)$$

$$\Rightarrow f = \frac{\Re_{\tau=0}\left(\hat{P}_{S-pert}, \lambda\right) - \Re_{\tau=0}\left(\hat{P}_{S-nopert}, \lambda\right)}{\Re_{\tau=0}\left(\lambda, \lambda\right)}$$

Thus, we can determine the leakage factor by first comparing the correlation of perturbations (λ) with $\hat{\vec{P}}_S$ in presence and absence of the perturbations, and then normalizing by the autocorrelation of the perturbations. As described previously, the leakage factor also gives a pessimistic estimate of how accurate the $\widehat{F}_{QP}$ obtained on the fly is.

Figure 5-4 shows results of an experiment to characterize the leakage factor. Here a paramagnetic probe of 1 μm diameter diffusing in 2M sucrose is tracked. The time at which perturbation injection begins is defined as time 0. The data acquired during the later half (0.5 seconds) of the perturbation span is used to obtain $\widehat{F}_{QP}$ as per the on-the-fly estimation procedure described in Chapter 4. The first half is used as the test bed for the newly obtained $\widehat{F}_{QP}$. The figure depicts curves for three signals: $\vec{S}_L$ (the measured position of stage) at the

bottom, $\hat{\vec{P}}_L$ (the estimated position of the probe relative to laser) in the middle, and $\hat{\vec{P}}_S$ (the probe position relative to specimen) at the top. .

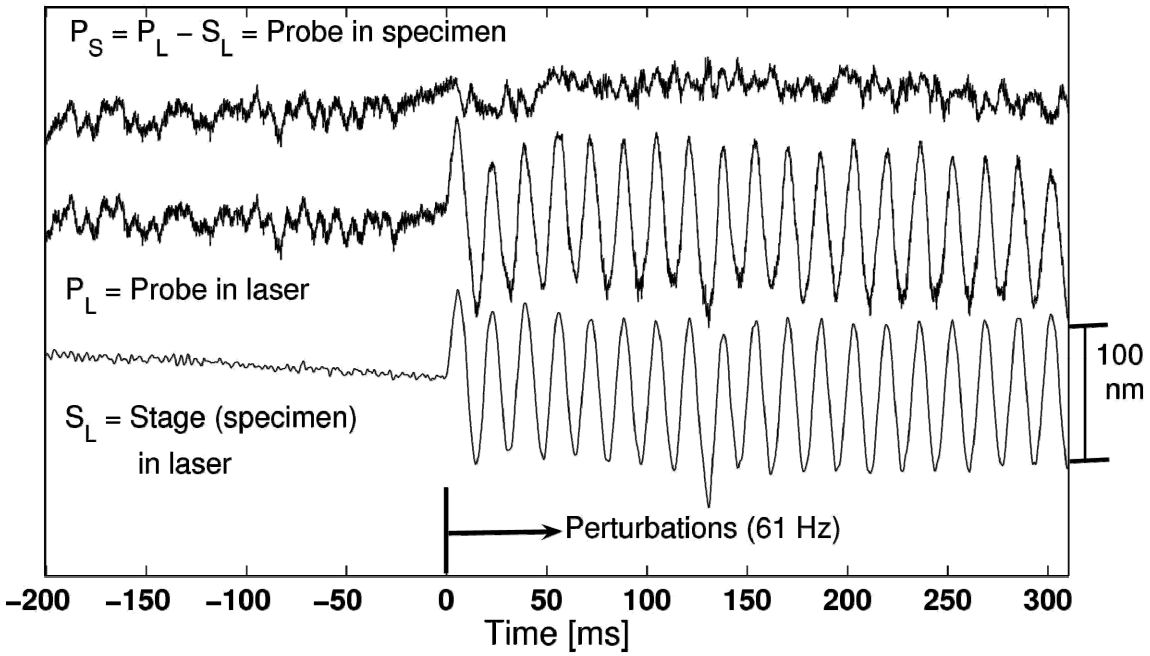

Figure 5-4: Performance characterization of on-the-fly estimation

As can be seen from Figure 5-4, the perturbation sinusoids are not visible in $\hat{\vec{P}}_S$, suggesting that the perturbations in the measured stage position are identically visible in $\hat{\vec{P}}_L$, further implying the accuracy of the newly obtained $\hat{F}_{QP}$ is accurate. For quantifying the accuracy we used the procedure described in the beginning of this section to compute the leakage factor. Here, 0.5 second span before time 0 was considered as the 'no-perturbation zone', and the 0.5 second span beginning at time 0 was considered as the 'perturbation zone'. The perturbation vector $\vec{\lambda}$ was determined using the template-matching procedure described in chapter 4 Equations 4.7 to 4.10. For the data shown in Figure 5-4, we obtained a leakage factor of 0.021; which, for 50 nm perturbation amplitude,

means that 50*0.021 = 1.05 nm of error was introduced due to the injection of perturbations. Interestingly, for perturbation amplitudes smaller than 50 nm, the leakage factor increased so as to keep the error floating at around 1 nm; but for perturbation amplitudes larger than 50 nm, the leakage factor stayed relatively constant at around 0.02, giving larger error for larger amplitude of perturbations. Putting these results together, we can draw several conclusions:

1. On-the-fly estimate of F_{QP} is accurate to within approximately 2%
2. 2% of perturbation amplitude, or 1 nm, whichever is higher show up as an error in the on-going measurement stream
3. The 1-nm baseline for the error introduced may be due to the compromised signal-to-noise ratio as the perturbation amplitude decreases; or it may be due to slosh, cross-coupling between QPD signals and stage drive etc.

In this section we saw that on-the-fly estimation has a spatial resolution of the order of one nanometer. In the previous sections we saw that the .temporal resolution of the technique is at least 0.1 ms. These numbers show that Agnostic Tracking allows us to harness the high spatiotemporal resolution that is offered by back-focal-plane laser interferometry.

5.4 Variations in the estimated F_{PQ} under numerous test conditions

The main motivation behind performing on-the-fly estimation is to be able to account for the variations in the QPD response to probe motion (F_{PQ}) as the probe moves through an optically heterogeneous environment. A simulation investigating the effect of variations in ambient refractive index was presented in chapter 2. In this section, I will attempt to experimentally characterize the variation in true F_{PQ} that is caused due to a heterogeneous biological environment. The reader may notice that in this section I am talking about the transfer function from probe position to QPD signals, i.e. F_{PQ}. Because F_{PQ} represents the physical phenomenon – in contrast to F_{QP}, which only represents an abstract concept -- it is easier and more intuitive to think in terms of F_{PQ}. In this dissertation, I will limit the use of F_{QP} to the discussion concerned with the software algorithms for position detection and detector calibration.

To characterize the variation of F_{PQ} due to changes in the ambient refractive index, we first need to characterize the variations that are observed in the estimated F_{PQ} but are not caused by the change in the ambient refractive index. Two potential sources of those variations are background scattering and instabilities of the estimation process. I will further elaborate on the first source.

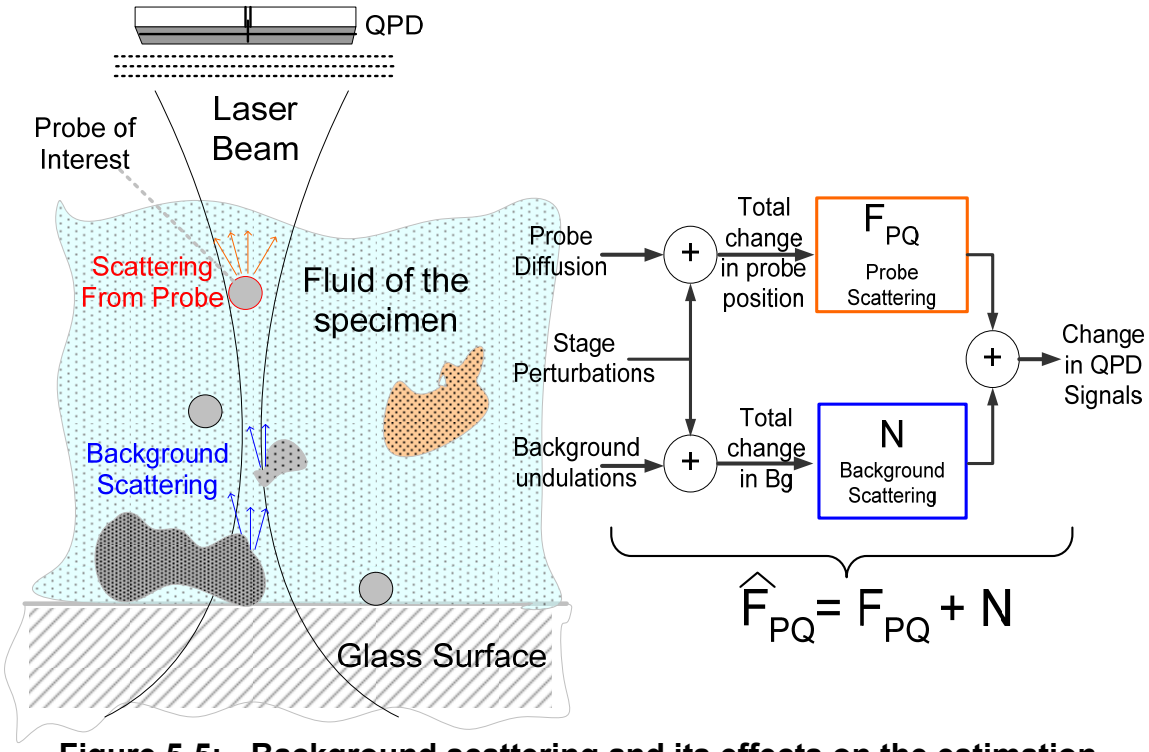

Figure 5-5: Background scattering and its effects on the estimation

Figure 5-5 presents a sketch (not drawn to scale) of the environment of the optical path. As seen, the optical path of the laser may encounter scattering objects other than the probe under investigation. For example, the scattering objects may include the specimen fluid, organelles or other probes. Thus there are two contributors to the scattering that is detected by QPD: probe scattering and background scattering. Because perturbations are injected in the stage position, the background moves with the probe. Thus as shown in Figure 5-5 on the right, the changes in QPD signals are caused by the change in probe position, as well as by the change in background position. Thus even in the most ideal case, where the probe is immobilized and background is static (no undulations), the estimated F_{PQ} is the sum of the sensitivity to probe position (true F_{PQ}) and the sensitivity to background position (N). Thus, sensitivity to

background scattering is a fundamental limitation of the agnostic tracking approach.

Thus there are three potential sources of variations in $\widehat{F}_{PQ}$ that may be observed for a probe moving through a biological environment.

1. Instabilities of the F_{PQ}-estimation algorithm
2. Variation in N, i.e., the sensitivity to motion of the background
3. Change in the refractive index of the environment

The remainder of the section presents four experiments; the first two are to investigate instabilities of the F_{PQ}-estimation algorithm, the third to investigate variations in the sensitivity to motion of the background, and the last to investigate variations caused by the change in the refractive index of the environment.

5.4.1 Immobilized bead

Here the specimen is a clean slide of 2M sucrose fluid, in which 1 μm diameter polystyrene beads are diffusing. For this experiment, a bead stuck to the glass coverslide, thus immobilized relative to the specimen, is chosen as the probe. Following is a description of the rest of the experiment, analysis and graphical representation procedure; which is identical for all four experiments.

Agnostic Tracking is initiated and one-second long perturbations are injected at every ten seconds for at least ten times. Immediately after each perturbation session, both F_{PQ} and F_{QP} are estimated and the F_{QP} used for position feedback is replaced with the newly estimated F_{QP}. Afterwards, the estimates of F_{PQ} are compared by applying each instance of F_{PQ} to a fixed range

of probe position, and plotting resulted QPD signals (one designated channel) as a function of that position range. The range of positions is chosen to be -40 to +40 nanometers; once along the X axis (lateral) and once along the Z axis (axial). Each figure also includes an annotation for the mean value of the slope $\mu(\Delta Q/\Delta P)$ and the standard deviation in the slope $\sigma(\Delta Q/\Delta P)$, where the slope is computed in the region between -20 to +20 nm. The standard deviation is represented as a fraction of the mean value for easier interpretation of the percentage dispersion.

As shown in Figure 5-6, all curves tightly overlay for the case of the fixed bead. The percentage variation in the estimate is 6.1% for lateral motion and 6.4% for axial motion.

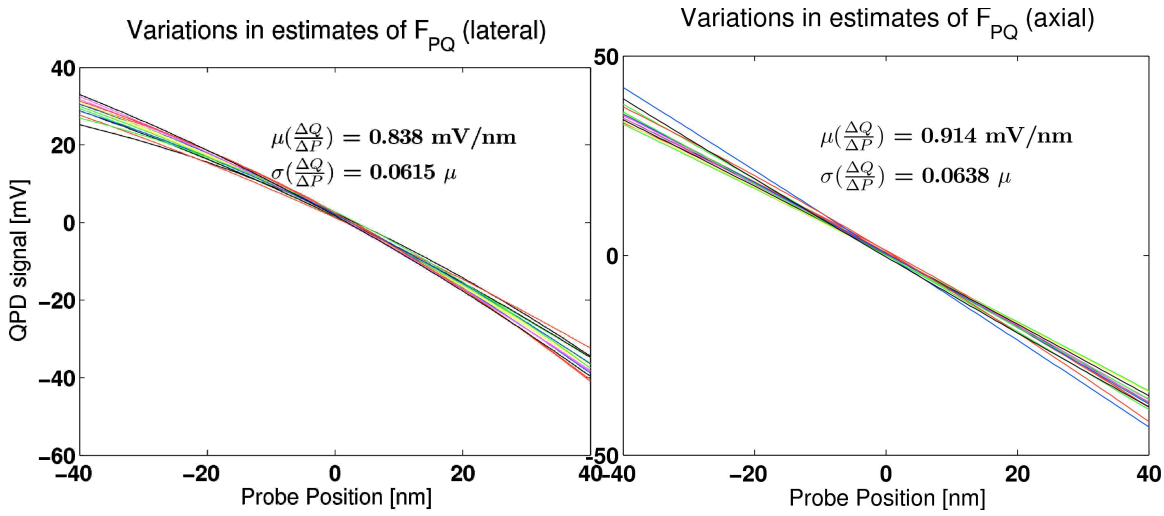

Figure 5-6: Variations in estimates of F_{PQ} for a fixed bead

5.4.2 Bead freely diffusing in a clean fluid

Here the specimen is identical to the one described in the previous section, except that a bead freely diffusing in the fluid is chosen as the probe. The results are plotted in Figure 5-7.

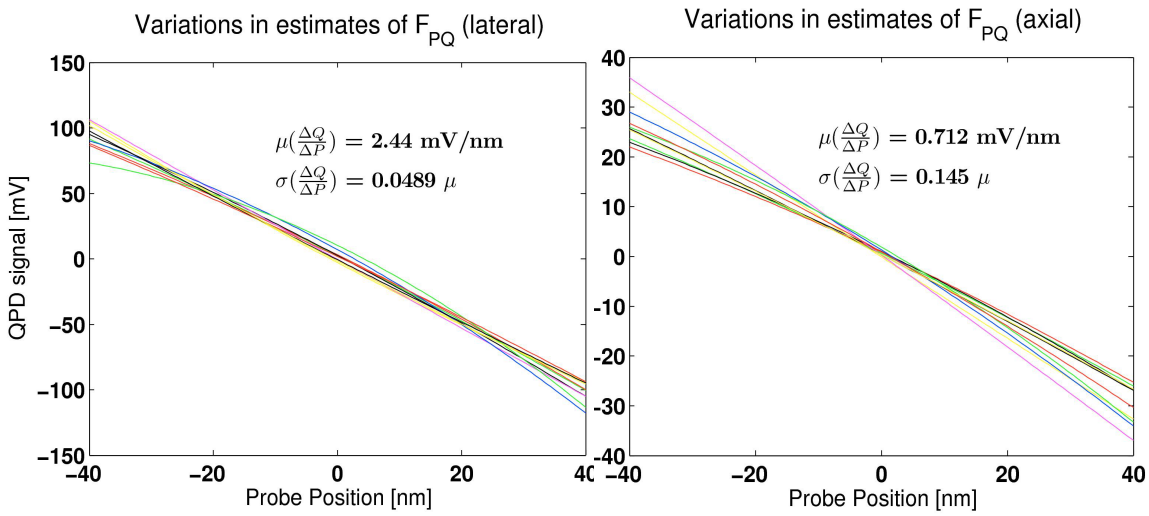

Figure 5-7: Variations in estimates of F_{PQ} for a freely diffusion bead

It is encouraging to see that the variations in the lateral-sensitivity estimates are less than 5%, suggesting a good stability of the on-the-fly estimation procedure. Here, the larger variations (14.5%) in the axial-sensitivity estimates, at least in part, may be attributed to the fact that the bead is also diffusing in Z. Sensitivity to Z motion is significantly affected by the distance from the reflecting surfaces, e.g., glass coverslides.

5.4.3 Cellular environment, no probe in the focus of the laser

Here the specimen is a slide with live cells and 1 μm diameter superparamagnetic beads. However, no bead is put under the focus of the laser. We seek to characterize how much the background scattering contributes to the estimated sensitivity. Presumably, the software is tracking a feature of the background that is producing a detectable scattering signal. An experiment and analysis procedure identical to previous sections is used, and the results are plotted in Figure 5-8.

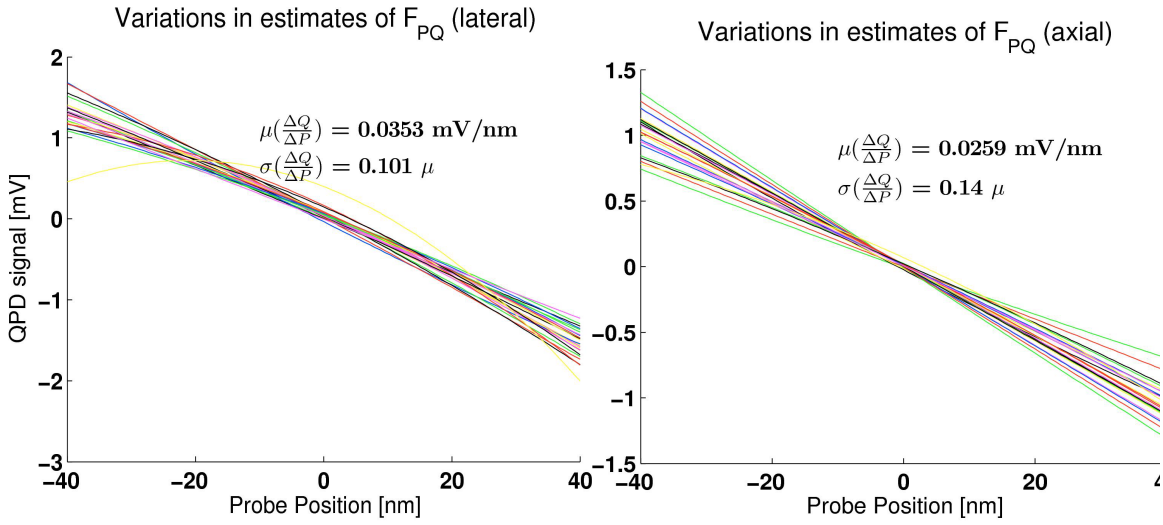

Figure 5-8: Variations in estimates of F_{PQ} for background scattering

The relatively tight distribution of the sensitivity estimates suggests that a biologically rich background does produce detectable scattering. However, compared to the freely diffusing bead, the lateral sensitivity to background is down approximately by a factor of 80 and the axial sensitivity to background is down approximately by a factor of 30.

5.4.4 Bead pulled inside a biological environment

Here, the specimen is same as the previous case, except a superparamagnetic bead is chosen as the probe. The bead is then pulled using electromagnets of 3DFM, and its motion is tracked. The rest of the experiment and analysis procedure is identical to previous cases.

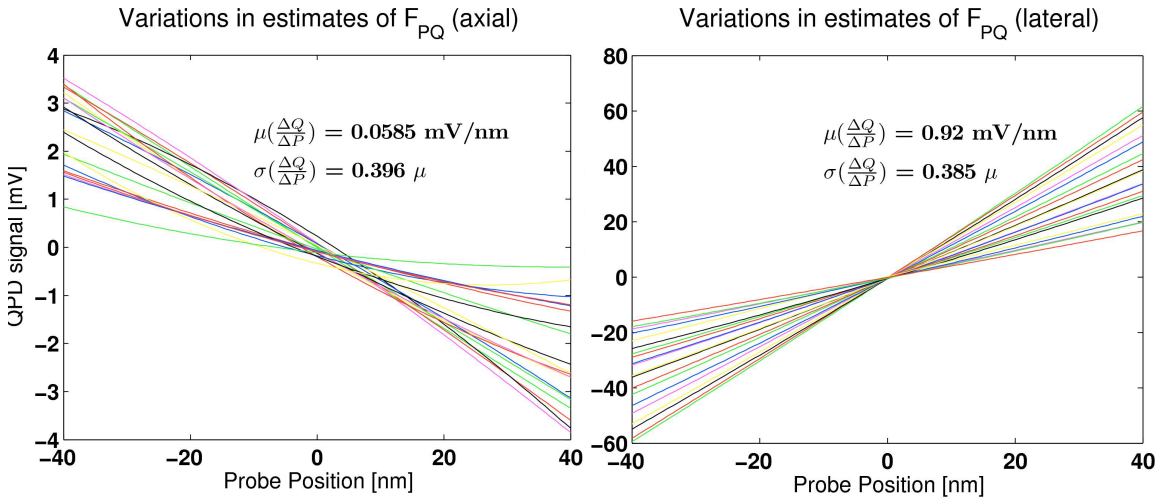

Figure 5-9: Variations in estimates of F_{PQ} for a bead among live cells

As seen in Figure 5-9, both, axial and lateral sensitivity estimates vary by approximately 40%, by far the largest among all four cases. One may be concerned about the Z sensitivity in this case, which happens to be only slightly higher than twice compared to the background scattering caused by the environment. While the axial sensitivity suffers greatly by a biologically rich environment, it should be noted that, in the case of the background scattering, the numbers necessarily represent a worst case scenario because we need sufficient sensitivity in order to initiate tracking, which forces us to select a location in the background that produces strongest scattering. Also, when a probe is in the focus of the laser beam, the background must naturally be out of

focus, which greatly reduces the contribution of the background to the scattering detected by QPD.

A table is presented to summarize the results of the four experiments.

Experiment Type	Est. lateral sensitivity		Estimated axial sensitivity	
	$\mu\left(\frac{\Delta Q}{\Delta P}\right)$ [mV/nm]	$100\times\frac{\sigma}{\mu}$	$\mu\left(\frac{\Delta Q}{\Delta P}\right)$ [mV/nm]	$100\times\frac{\sigma}{\mu}$
Bead stuck to glass coverslide	0.84	6.2	0.91	6.4
Bead diffusing in clean fluid	2.44	4.9	0.71	14.5
No bead, only biological background	0.035	10.1	0.026	14.0
Bead diffusing in biological background	0.92	38.5	0.059	39.6

Table 5-1: Summary of variations in estimated F_{PQ}

Using the table, we can safely conclude that when the bead is diffusing in a biological environment, at least two thirds of the observed variation in $\widehat{F}_{PQ}$ can be attributed to the change in ambient refractive index. Thus, for tracking a probe in a biological environment, F_{QP} should be estimated frequently, and if needed, continuously.

Chapter 6 Optimization of the detector sensitivity

In previous chapters we saw a procedure to calibrate the position detection sensitivity. This chapter presents an approach to improve the detector sensitivity itself.

6.1 Motivation

As mentioned in the Chapter 2, the true F_{QP} is nonlinear and has less-sensitive as well as multi-valued regions within the beam waist. The sensitivity of F_{QP}, and thus of the QPD, directly affects the signal-to-noise ratio of the position measurement system. To be able to reliably detect single-molecule-scale displacements, the probe must be kept in a region of the beam waist where the sensitivity of the QPD is sufficiently high. However, for a low-power laser interferometry, thermal and other forces of the environment dominate among the forces driving the probe. So, until position feedback is initiated, we have little control over the probe position relative to the beam waist. Thus any offline estimate of F_{QP}, including the one for initiating position feedback, must be obtained at the arbitrary spot of the beam-waist where the probe happens to be. Clearly, sufficient sensitivity cannot be guaranteed to begin with. Once position feedback is operational, it is desired to search within the beam waist for a probe position that offers higher sensitivity of the QPD.

Hence, the problem is of a function optimization type. We have a function, i.e. sensitivity of the detector, and starting from a given value of an independent variable, i.e., probe position, we incrementally explore the input parameter space to search for the value that maximizes the given function. The emphasis is on reaching to a spot where smallest displacements at the length-scale of interest can be detected; we do not aim to find a spot that has the highest sensitivity *globally*. This chapter presents an approach to locally optimize the sensitivity of the detector, along with an evaluation based on a real volumetric-scan data as the test-bed F_{QP}.

6.2 Definitions

F_{PQ}: The mapping from 3D probe position to QPD signals. F_{PQ} is a model of the physical scattering process as observed by the QPD. F_{PQ} is a family of four polynomials, one for each quadrant:

$$F_{PQ_j} : F_{PQ_j}\left(P_x, P_y, P_z\right) = Q_j \qquad j = 1,2,3,4$$

Jacobian: The mapping from a change in probe position to a change in QPD signals. A Jacobian can be computed by taking partial derivative of each polynomials of F_{PQ} with respect to X, Y, and Z coordinates. Knowledge of the Jacobian is used for characterizing responsiveness of the QPD at any given point in the operable neighborhood.

$$J = \begin{vmatrix} \frac{\partial Q_1}{\partial P_x} & \frac{\partial Q_1}{\partial P_y} & \frac{\partial Q_1}{\partial P_z} \\ \frac{\partial Q_2}{\partial P_x} & \frac{\partial Q_2}{\partial P_y} & \frac{\partial Q_2}{\partial P_z} \\ \frac{\partial Q_3}{\partial P_x} & \frac{\partial Q_3}{\partial P_y} & \frac{\partial Q_3}{\partial P_z} \\ \frac{\partial Q_4}{\partial P_x} & \frac{\partial Q_4}{\partial P_y} & \frac{\partial Q_4}{\partial P_z} \end{vmatrix}$$

Singular value decomposition (SVD) [72] of the Jacobian evaluated at the operating point would give three singular values.

$$J\left(P_{x0}, P_{y0}, P_{z0}\right)$$

$$\Downarrow SVD$$

$$\underbrace{\begin{bmatrix} . & . & . & . \\ . & . & . & . \\ . & . & . & . \\ . & . & . & . \end{bmatrix}}_{R_Q} \times \underbrace{\begin{bmatrix} S_1 & 0 & 0 \\ 0 & S_2 & 0 \\ 0 & 0 & S_3 \\ 0 & 0 & 0 \end{bmatrix}}_{S} \times \underbrace{\begin{bmatrix} . & . & . \\ . & . & . \\ . & . & . \end{bmatrix}^T}_{R_P^T}$$

Sensitivity Index: The three singular values provide a measure of the sensitivity along three principal directions. Because and simple, univariate optimization routine can only optimize one variable, we need to combine the three singular value into a single number. We refer to the representative number as Sensitivity Index.

A Proper design of the function that combines the singular values to produce Sensitivity Index is crucial. Because the need for a sufficient sensitivity is equally strong for all directions, the combining function should be designed such that if *any* of the three singular values is lower, the sensitivity index is lower. If simple functions, e.g., sum, product etc, are chosen to combine the three singular values and produce Sensitivity Index, the optimizer routine is free to accentuate already-higher singular value(s) at the expense of diminishing already-lower singular value(s). Sum of reciprocals on the other hand would motivate the optimization routine to balance the three singular values; however, it is a counterintuitive language to say that the Sensitivity Index must be minimized

in order to achieve higher sensitivity. Hence, we chose reciprocal of sum of reciprocals of the singular values to define the (I_S):

$$I_S = \left[\frac{1}{S_1} + \frac{1}{S_2} + \frac{1}{S_3} \right]^{-1}$$

6.3 Evaluation Framework

I used Matlab simulations on a real volumetric-scan data to evaluate various optimization strategies. The volumetric-scan data was obtained by raster scanning a fixed probe in approximately 1 μm x 1 μm x 1.4 μm size volume of the beam waist; and recording the stage position and the QPD signals simultaneously. The grid granularity was 20 nm x 20 nm x 30 nm in X, Y and Z respectively. At each point on the grid, 1000 samples were collected at 10 kHz rate, and averaged to obtain an accurate and less noisy measurement of the stage position and the QPD signals. A controlled amount of noise was artificially introduced during simulations to investigate the sensitivity of a particular optimization approach to the amount of noise present. A list of several points in the volume was randomly generated, and then twelve points from the list were manually selected by ignoring the points that fell in hopelessly insensitive regions of the volume. Because we aim to optimize only locally, beginning at a point within a flat and insensitive neighborhood guarantees a failure of the optimization routine, while providing no insight on how successful the optimization routine is in general. Each of those twelve points was fed to the optimization routines as the

initial operating point, and the success and speed of convergence to a local maximum was investigated.

6.4 Optimization Strategy

Because the problem is of local optimization type, my first attempt was to use gradient-based steepest ascent [73]. The idea is to apply the gradient operator [74] to each of the 12 Jacobian elements (polynomials in X, Y and Z.) and step in a direction given by the vector sum of the 12 gradient vectors. The approach was largely unsuccessful. Presumably, the primary reason behind the poor performance was use of more variables (twelve) than inherent degrees of freedom (three). The approach uses twelve gradient vectors to optimize sensitivity along three directions. This under-constrained process accentuates the sensitivity of a successful convergence to the amount of noise present. We devised an extension to the gradient-based steepest ascent method, by reducing the number of variables to the number of degrees of freedom.

6.4.1 Steepest ascent after untangling the space

We use Singular-value Decomposition (SVD) to untangle the parameter space and reduce the number of variables from twelve to three. The SVD of the numerical Jacobian evaluated at the operating point decomposes the Jacobian into three matrices: a rotation matrix in XYZ space (R_P), a diagonal matrix (S) containing three singular values, and a rotation matrix in QPD space (R_Q). If we assume that the rotation matrices remain constant within a small neighborhood, we can algebraically apply the rotations to the original elements (polynomial

expression in terms of X, Y, Z) of the Jacobian. If the assumption is valid, then the off-diagonal elements of the Jacobian should vanish; which was verified for the test-bed scan data. The polynomial expressions in the diagonal elements of the rotated Jacobian describe how the sensitivity varies along the three principle directions, as a function of X, Y and Z coordinates of the operating point. The remaining task is identical to the gradient-based steepest ascent, except the number of parameters is now reduced to three, which should help converge. The step-by-step algorithm is given below:

1. Sample the local neighborhood (approximately 150 nm^3) of the operating point by simulating perturbations, and fit F_{PQ} on the data obtained. Use linear interpolation when the perturbation point falls between two points of the volumetric-scan grid. For results reported here, a 2nd-order F_{PQ} was fit. The procedure for fitting F_{PQ} is identical to that for fitting F_{QP}, except that Ps are the independent variables and Qs are the dependent variables.
2. Compute Jacobian (*J*) by taking partial derivative of each of the four polynomials of F_{PQ} with respect to X, Y, and Z coordinates.
3. Evaluate *J* at the operating point and obtain a 4 x 3 matrix J_0. Compute singular-value-decomposition of J_0, and obtain the sensitivity-index as per the formula mentioned above.
4. If the sensitivity index is smaller than the previous iteration, reduce the step-size by a predefined fraction. I used 1/3rd of the size of the operable neighborhood as the initial step size and 0.5 as the reduction fraction.
5. Apply inverses (i.e. transposes for unitary matrices) of the rotation matrices obtained by the SVD to the Jacobian *J,* and obtain a rotated

Jacobian $J_R = R_Q^T \times J \times R_P$. Verify that the non-diagonal terms of J_R are negligible. The three elements of the leading diagonal of J_R represent the analytical expressions for the three principal components of J. This step accomplishes the task of untangling the parameter space.

6. Apply gradient operator on each of the three analytical expressions obtained in step 5. The resulting vector expressions signify the three directions along which the three principal components of J have steepest rate of increase.
7. Obtain a vector sum of the three gradient vector expressions and evaluate the sum at the operating point. The result gives the direction for the step.
8. Adjust the magnitude of the vector to be identical to the preset step size. Translate the operating point by the resulting vector. Repeat from step 1

6.5 Performance evaluation

The volumetric-scan-based performance-evaluation framework is described in section 6.3. The results obtained were very encouraging. With 10 nm (rms) noise added to the position measurements, the approach reliably converged to the local maximum (11 out of 12 points), with 11 iterations on average. Also, the reliability of the approach was largely unaffected by the lower sensitivity of the initial operating point, as long as the initial operating point was not surrounded by insensitive neighborhoods. For example, an operating point with the sensitivity index as low as $1/10^{th}$ of a nearby local maximum yielded a successful convergence to the local maximum.

Figure 6-1 presents a full-size version of the visualization scheme that was used to monitor the progress of the optimization process. The red-color cross indicates the operating point. The gray-scale square on the left shows how the sensitivity index varies over the XY slice of the beam waist (brighter means more sensitive), whereas the gray-scale bar on the right shows how the sensitivity index varies along the line parallel to the Z axis and passing through the operating point. The solid red line in the Z bar indicates the location of the operating point in Z. The operable neighborhood (150 nm x 150 nm x 150 nm) is indicated by the circle centered at the cross in XY, and by the two dotted lines symmetrically placed around the solid line in the bar.

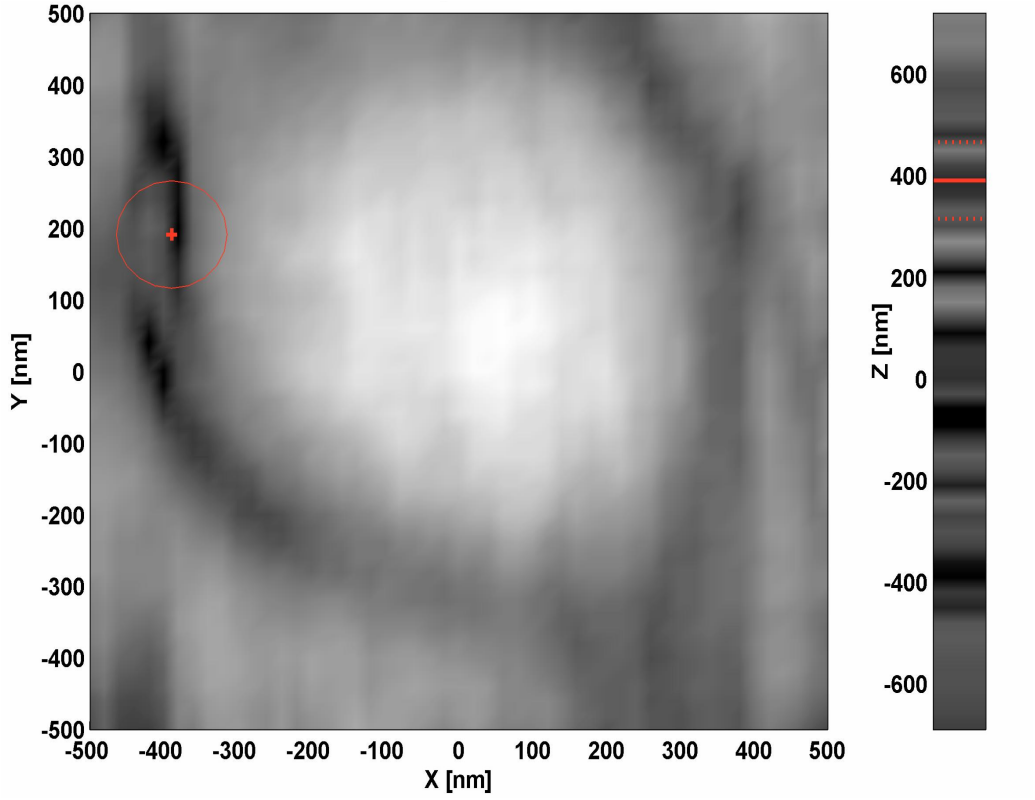

Figure 6-1: Visualization of sensitivity in the scanned volume

Figure 6-2 shows every other frame in the iteration sequence. For each frame the bottom-left plot shows absolute values of the sensitivity index and the singular values, for both the current iteration (blue bars) and the initial operating point (brown bars). The numbers in the parenthesis on the Y axis represent values of the sensitivity index and singular values at the current operating point. The bars in the bottom-right plot show the ratio of the current sensitivity index and the individual singular values to those for the initial operating point.

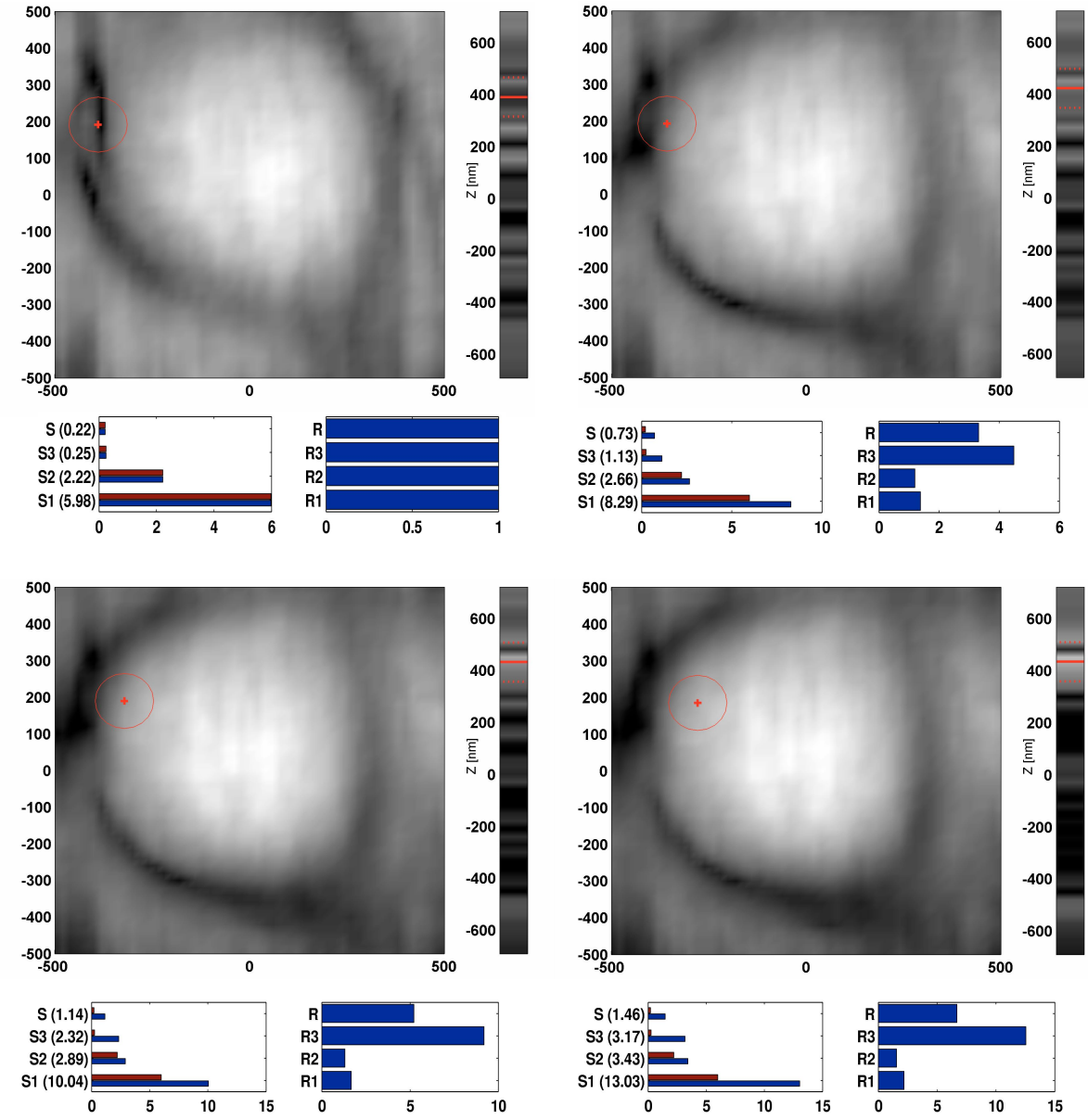

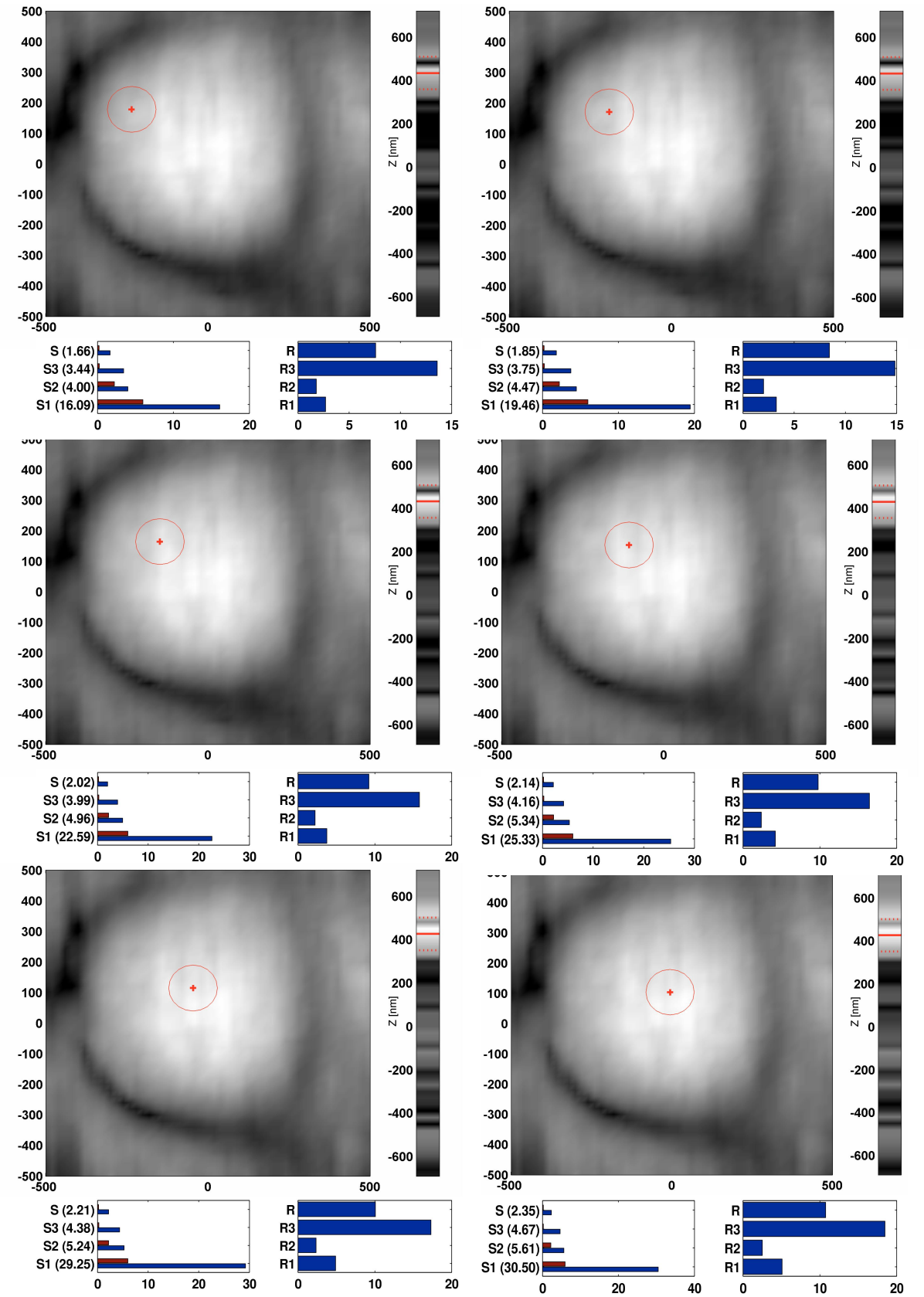

Figure 6-2: Odd-numbered iterations of a successful optimization attempt

It can be seen from the sequence that initially, S_3, is the smallest among the three singular values; also S_3 shows the largest improvement (18 fold) among the three singular values as well. This feature of improving the weakest is what we sought for while designing the formula for the Sensitivity Index. It is also noteworthy that the sensitivity index has improved more than ten fold during the convergence course of 20 iterations.

6.6 Handling relocation of the laser-coordinate-frame origin

Relocating the operating point is an essential step for the optimization procedure. Also, because controlling the probe position within laser is essential, the optimization procedure can only be executed after the position-feedback is operational. Relocating the operating point is essentially changing the set point ($\vec{R}_L$) for the position-feedback loop, as shown in Figure 3-3. Because the original equation for measuring probe position relative to specimen does not involve any term for the set point, it is not obvious how the relocation of the set points can be handled when optimization is executed. I will elucidate the issue in this section.

Figure 6-3(a) shows the coordinate frames arrangement at the beginning (time 0) and the same at the current time (t). The arrangement at time 0 is identical to the one presented in the Figure 3-1. The origin of the laser coordinate frame has moved at time t as the result of the optimization procedure. As shown in the vector arrangement in Figure 6-3(b), the change in the operating point (L*) can be represented as $\vec{L}_G(t) - \vec{L}_G(0)$.

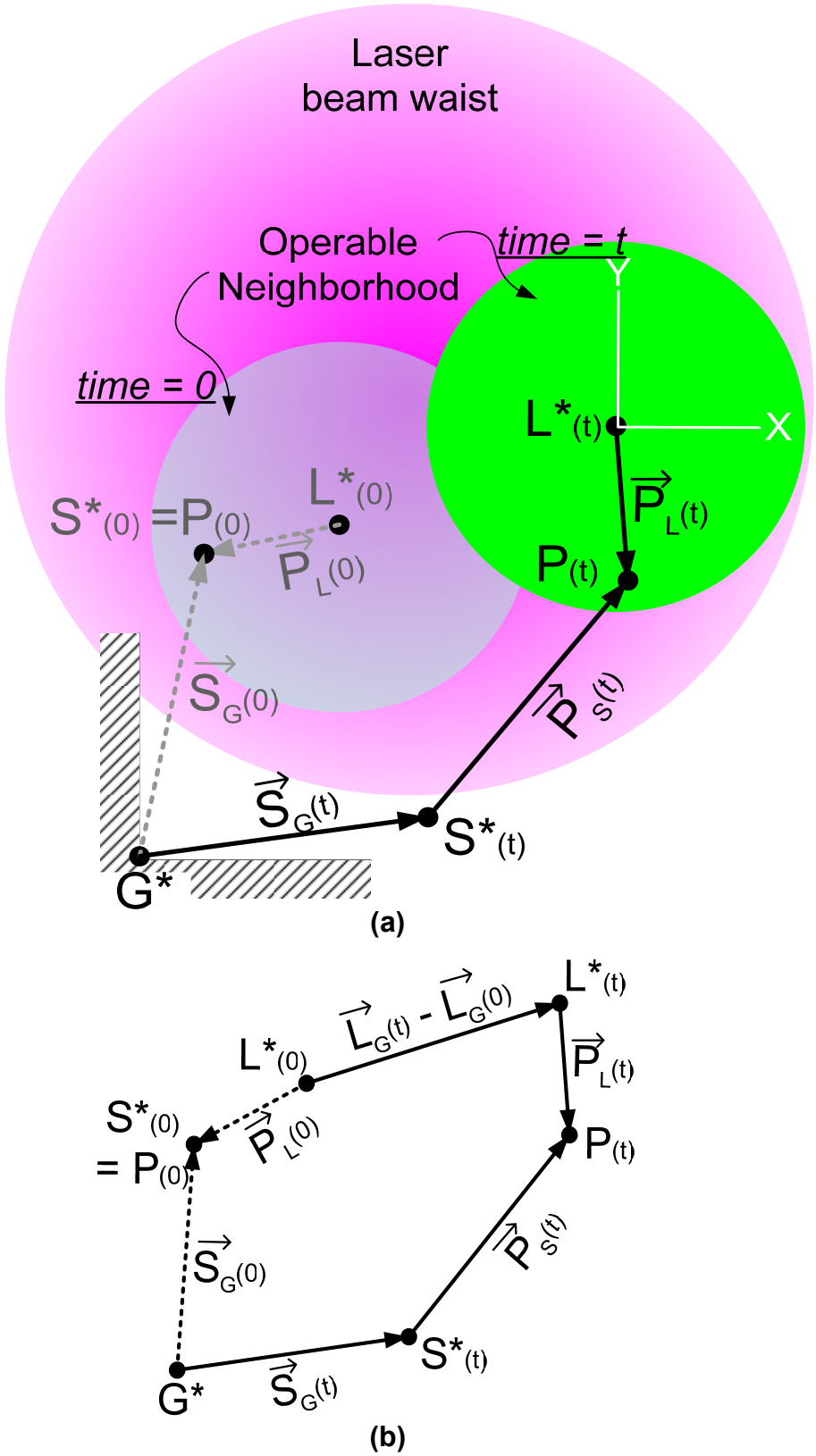

Figure 6-3: Handling relocation of the set point

Traversing the vector loop, we can write:

$$\begin{aligned}\vec{P}_S(t) &= -\vec{S}_G(t) + \vec{S}_G(0) - \vec{P}_L(0) + \vec{L}_G(t) - \vec{L}_G(0) + \vec{P}_L(t) \\ &= \left[\vec{P}_L(t) - \vec{S}_G(t) + \vec{L}_G(t)\right] - \left[\vec{P}_L(0) - \vec{S}_G(0) + \vec{L}_G(0)\right]\end{aligned}$$

The RHS of the equation is similar to that of Equation 3-1, with the terms added for relocation of the laser coordinate frame, i.e., $\vec{L}_G(t) - \vec{L}_G(0)$.

6.7 Incorporating the optimization procedure into the 3DFM

In this dissertation, I have restricted the optimization approach to simulations. The description of the optimization approach assumed that a position feedback is operational; and each iteration of the simulation began by recalibrating the QPD response on the fly using the procedure described in chapter 4. The ultimate goal, however, is to incorporate the optimization procedure in the 3DFM instrument, hence I here summarize the necessary tasks.

A typical experiment involving optimization may be broken down into following steps:

1. Obtain an offline estimate of F_{QP} and initiate position feedback.
2. Obtain an on-the-fly estimate of F_{QP} as well as that of F_{PQ} .
3. Execute steps 2 to 8 of the optimization procedure described in section 6.4 and obtain the step vector current operating point.
4. Translate the set point of the feedback loop by the step vector. Because this change is essentially a step input for the feedback loop, we must wait for sufficient time to let the loop reach a steady state. Because the bandwidth of the feedback loop is approximately 30 Hz, I estimate that 1

ms of waiting time would be sufficient for steps up to 100 nm. If needed, more accurate estimate of the wait time can be obtained by driving the stage with appropriately-sized steps and measuring the time till the stage reaches the steady state value. Record the relocation of the set points, to be used for the position measurement procedure described in section 6.6.

5. Repeat the steps 2 to 4 until the sensitivity index converges.

The procedure for estimating F_{QP} offline as well as on the fly has been incorporated and tested in the software controlling the 3DFM. The procedure for estimating F_{PQ} and rest of the optimization procedure has been implemented and tested in a stand-alone simulator in Matlab. Hence the task remaining is to translate the code related to optimization procedure to VC++, i.e. the programming language in which controller software for the 3DFM is written. The code to be translated includes custom-built subroutines for analytically computing and evaluating Jacobian and gradient; as well as the Matlab-inbuilt routine for SVD. Once all pieces of the code are available in C++, they should be put together as the step-by-step procedure described above. Coding necessary for adding a wait time and keeping track of set-point relocation is trivial.

Chapter 7 Measuring frequency response in biology

In order to grow and perform vital functions, cells must adapt to external forces and dynamic mechanical properties of their environment. Investigating and understanding how cells respond, through remodeling and gene expression, to external stimuli, is of great scientific interest. It is also known that the viscoelastic properties, i.e., stress-strain relationships, play a key role in many biological processes such as cell crawling, wound healing, gene expression and protein regulation, and even cell's programmed death [75]. Several diseases, such as cancer, asthma, or sickle cell anemia, involve alteration of the viscoelastic properties of a given cell type. The viscoelastic properties of the cells are primarily controlled by organization and mechanics of the cytoskeletal network -- a dynamic assembly of biopolymers, principally comprised of actin filaments, intermediate filaments, and microtubules, interacting with a variety of associated proteins, crosslinkers, and molecular motors. The mechanical properties of the cytoskeletal network and cell membranes are therefore the focus of many experimental studies.

The approaches to investigate mechanical properties of the cytoplasm and cell membrane can be grouped into two broad categories: passive and active. The passive techniques involve monitoring natural motion of particles attached to a cell membrane or imbedded in cytoplasm; while active techniques involve

monitoring mechanical response to external stress stimuli. The first use of particle tracking for probing cell-membrane mechanics was reported by Webb and collaborators [5] and several further developments involving video tracking have been reported since [6, 11-13, 18, 19]. Kusumi and Sako [9] reviewed the use of video-based particle tracking in investigating the role of the membrane skeleton in cell surface organization; while Saxton and Jacobson [10] provided a comprehensive review of using single-particle-diffusion measurements to understand the structure and the dynamics of a cell membrane. In addition to video, laser-based techniques for single particle tracking are also used for passive investigation of cellular mechanics [36, 38-40, 76-80]. For active probing and measurements of the viscoelastic properties of a cell, a diverse repertoire of micromanipulation techniques is available. Examples include atomic force microscopy (AFM) [81-83], micropipettes [84], cell indentation [85], shear flow cytometry [86, 87], microplates [88-92], optical tweezers [92-95], optical stretchers [96, 97], magnetic tweezers [1, 45-48, 50, 52, 54] and magnetic cytometry [98-105].

The aforementioned micromanipulation techniques probe both the membrane and the cytoskeleton properties at different length scales and time scales by exerting stresses and strains in different geometries and with different orders of magnitude. Among these, the techniques based on single-particle manipulation and tracking are of a specific interest because of their ability to reveal local properties of a heterogeneous environment, at both high spatial resolution and high temporal resolution. The remainder of the dissertation is concerned with applications of Agnostic Tracking to probe cellular mechanics. In

this chapter, I will describe a concept of building a high-bandwidth frequency-response analyzer for biology, based on Agnostic Tracking as implemented in the 3D Magnetic Force Microscope (3DFM).

7.1 What is a frequency response?

The *"frequency-response"* of a system can be loosely defined as the *"response"* of the system represented in the *"frequency"* domain. In general, it is a measure of the output of any system when a signal of varying frequency and constant amplitude is applied as its input.

The term frequency response is well defined if the system is assumed to be linear; there are standard ways to measure frequency response of a linear system. However, interpretation of the term frequency response is not well defined for a nonlinear system; and to the best of my knowledge, there is no single canonical way to measure frequency response of a nonlinear system. First I will review the standard protocol for measuring frequency response of a linear system, and then I will present an abstract scheme that can be employed to measure the frequency response of any linear system and restricted types of nonlinear systems.

7.1.1 Why do we need to measure the frequency response?

As per recent reports, relaxations at all time scales are present simultaneously within the cell body, which is in contrast to the traditional view that a cell can be modeled using a small, finite number of relaxation times or time constants. For example, recent experimental studies have revealed that both the

cytoplasm and the cellular membranes have complex viscoelastic moduli that exhibit a power law behavior over a frequency range of 0.1 Hz to 1kHz [89, 92, 101, 106]. Also, while it is known that biopolymers such as fibrin fiber and microtubules possess high stiffness, the exact frequency dependence of viscoelastic properties of many of the biopolymers is still to be investigated. A technique that can generate mechanical stimuli and measure the response thereto, both with a wide frequency band, can provide a complete picture of complex viscoelastic properties of the biological entity under investigation.

7.2 How to measure the frequency response?

As we saw, it is desired to measure frequency response in biology. Here, I will define the frequency response for a linear and a nonlinear system and then describe methods of measuring each.

7.2.1 Frequency response of a linear system

Linear systems are defined by their superposition property. A system $y = f(x)$ is said to be linear if the following equation is satisfied for all inputs x_1 and x_2, and all constants a and b.

$$f(ax_1 + bx_2) = af(x_1) + bf(x_2) \qquad \text{Equation 7.1}$$

A convenient way of representing a linear system is using its unit impulse response. For example, $y(t) = h(\tau) * x(t)$ is a single-input single-output system with an impulse response $h(\tau)$. If the system is also time invariant (i.e. $h(\tau)$ does not change over time), then the frequency response is defined as the Fourier transform of the unit impulse response:

$$H(f) = \int h(\tau) e^{-2\pi f \tau} d\tau$$ Equation 7.2

Also by taking Fourier transform on both sides of the input-output relationship in the time domain, we get

$$Y(f) = H(f) X(f)$$ Equation 7.3

Where,

$$X(f) = \int_0^T x(t) e^{-j2\pi ft} dt$$

$$Y(f) = \int_0^T y(t) e^{-j2\pi ft} dt$$

Note that the RHS of the equation is a simple multiplication, unlike the convolution for the time-domain equation. The result of the Fourier transform is a complex number that varies with frequency. So, the frequency response can be represented in polar form as:

$$H(f) = A_{(f)} e^{j\phi(f)}$$

Where,

$A(f)$ = system gain for the input frequency f

$\phi(f)$ = system phase for the input frequency f

We can rewrite the input-output relationship in the frequency domain as:

$$Y(f) = A_{(f)} e^{j\phi(f)} X(f)$$

Thus, if the input is decomposed into sinusoids, a linear system only changes the amplitude and the phase of the input sinusoids, but not the frequency. Thus the output of a linear system exists only at those frequencies at

which the input exists. This is a key observation that greatly simplifies the measurement of the frequency response of a linear system.

7.2.2 Measuring frequency response of a linear system

For simplicity, we will consider the single-input, single-output linear, time-invariant system depicted below

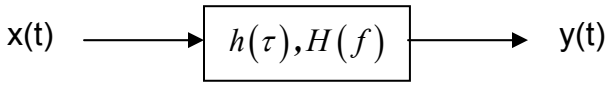

From the definition of the frequency response,

$$Y(f) = H(f)X(f)$$

So, from knowledge of the finite Fourier transforms Y(f) and X(f), the frequency response could be readily computed as

$$\widehat{H}(f) = \frac{Y(f)}{X(f)}$$

In practice, to avoid the division by a complex number, both the numerator and the denominator are multiplied by the complex conjugate of the denominator. Thus,

$$\widehat{H}(f) = \frac{X^*(f)Y(f)}{|X(f)|^2}$$

Usually the signals in the time domain *x(t)* and *y(t)* have more points (and thus more information) than their Fourier transforms *X(f)* and *Y(f)*, because the duration of the data is usually longer than that required for specified frequency-resolution in *H(f)*. E.g., for a 0.1 Hz resolution in *H(f)*, only 10 seconds of data is required. In practice, the time-domain data are partitioned into multiple sections,

each of the length that is required for specified frequency resolution in *H(f)*; and then results for all sections are averaged, which reduces the error in the estimate of *H(f)*. Thus,

$$\widehat{H}(f) = \frac{E\left[X^*(f)Y(f)\right]}{E\left[\left|X(f)\right|^2\right]}$$

The numerator and denominator can now be replaced by a term familiar to the signal-processing community, i.e., *spectral density functions.*

$$\widehat{H}(f) = \frac{\lim_{T\to\infty}\frac{2}{T}E\left[X^*(f)Y(f)\right]}{\lim_{T\to\infty}\frac{2}{T}E\left[\left|X(f)\right|^2\right]}$$

$$= \frac{G_{xy}(f)}{G_{xx}(f)} \qquad \text{Equation 7.4}$$

$$= \frac{\text{Input-output cross spectral density function}}{\text{Input autospectral density function}}$$

So, the canonical procedure for estimating the frequency response of a linear system is to take the element-wise ratio of input-output cross-spectral density function to input auto-spectral density function.

7.2.3 Nonlinear systems

Any system that does not satisfy equation 6.1 is dubbed as a nonlinear system. For a nonlinear system the output may exist at both super-harmonics (quadratic system, cubic system etc) and sub-harmonics (quartz plates, crystal oscillators etc) of the input frequencies. If the system involves modulation (heterodyning), the output frequency can even be shifted from the input frequency. So, the frequency response of a nonlinear system cannot be

represented simply as a polar complex number (a gain and a phase) varying with frequency. Also, because the sub-harmonics and super-harmonics of two frequencies can overlap, the output to a wide-frequency-band input cannot be treated or visualized as a whole to compare responses at different frequencies. Thus analyzing the response of a nonlinear system in the frequency domain requires special treatment. In the next section, I will present a scheme for estimating and representing a restricted type of nonlinear systems in the frequency domain.

7.2.4 Analyzing nonlinear systems in frequency domain

For the purpose of measuring the frequency response of any system, the input should contain all the frequencies at which the frequency response is of interest. A common practice for linear systems is to use band-limited white noise as the input; which contains equal energy of each frequency within a specific frequency band and zero energy for frequencies outside the band. Thus the denominator in Equation 6.4 reduces to a constant, and the numerator reduces to a function of Fourier transform of the output only. Both of the simplifications offered by white noise could also be achieved if the input is a train of sinusoids of varying frequencies but constant amplitude; as long as the sinusoids cover all the frequencies of interest. In addition, the sinusoidal system is particularly advantageous when dealing with nonlinear systems. When the input is a sinusoid, the output record can be segmented such that each section contains response to only one sinusoidal input. This segmentation according to input frequencies avoids the overlapping of the system response to multiple

frequencies. Once the output is segmented, an analysis procedure can be carried out on each segment separately.

One commonly employed approach for analyzing nonlinear systems is in terms of the energy that the super-harmonics of the test frequency contain in the measured output. The canonical term used for this type of analysis is total-harmonic-distortion (THD), a metric of *nonlinearity*, defined as the ratio of energy at the fundamental to the energy at harmonics, both in the output. Energy at any frequency is obtained by integrating the peak at the particular frequency in the power-spectral-density (PSD) function of the signal. THD once computed for each segment, can be plotted as a function of input frequency on a single graph; which can be considered as a representation of the system response in the frequency domain. Another relevant metric is efficacy of the system, defined as the ratio of recovered energy to input energy. Here, recovered energy is obtained by calculating the power spectral density function of the particular output segment and then summing up the energy contained in all harmonics (including fundamental) of the test frequency. Once efficacy is computed for each segment of the output, the *efficacy* of the system can be plotted as a function of the input frequency on a single graph, which again gives a representation of the system response in the frequency domain.

Thus an input comprised of sinusoids of constant amplitude and varying frequency offers a way of analyzing a nonlinear system in the frequency domain. I will discuss later that the efficacy measurement as a function of the input frequency is particularly appealing for investigating mechanical-properties in biology.

7.3 Frequency-response analyzer for biology: state of the art

Because the frequency response is directly related to viscoelastic properties, some work has been done to build a frequency response measuring apparatus for the field of biophysics. Parallel microplates are often used to create oscillations across the whole cell body and measure macroscopic elastic modulus [88, 90]; however, single-particle based techniques must be applied in order to probe the local mechanical properties. Three primary approaches have been employed: magnetic twisting cytometry [99, 100, 104, 107], optical tweezers [92, 94], and oscillatory magnetic bead rheometer [55, 108].

7.3.1 Magnetic twisting cytometry

Magnetic twisting cytometry (MTC) was developed by Fredberg and collaborators, which probes mechanical properties of an adherent cell by applying a torque to a magnetic bead that is tightly bound to the cell surface. Here, magnetic moments of ferromagnetic beads are aligned using a brief strong magnetic field. Then a weaker, “twisting” field is applied perpendicular to the original field. Because a ferromagnetic bead retains its magnetism, the interaction between the retained magnetic moment of the bead and the second magnetic field produces a torque on the bead, and exerts a controlled shear stress (up to approximately 70 dyne/cm^2) on bound cell surface receptors. The strength of the second magnetic field is varied sinusoidally in time to produce oscillations of the bead, thus exert sinusoidal stress on the cell surface receptors. The average angular rotation (strain) of the beads is measured by detecting the horizontal component of the bead’s remnant fields using a magnetometer [54,

109]. The relationship between the applied torque and resulting angular rotations is used to determine the complex modulus of elasticity (G_e).

In addition to rotation, the applied torque also causes a lateral displacement of the bead. Recently, investigations using the relationship between the applied torque and resulting lateral bead displacements have also been reported [107, 110], which is called optical magnetic twisting cytometry (OMTC). Here, the lateral bead displacement is detected by a charge-coupled device (CCD) camera. Image acquisition is phase locked to the twisting field using a synchronous pulse triggering.

Because the stress experienced by the surface receptor is dependent on the geometry of the binding site between the bead and the cell, computation of the actual elastic modulus of the cell requires knowledge of the geometry. Milanjovich [111] reported 3D finite element models to compute the relationships between the applied torque and resulting cell deformation, bead rotation, and lateral bead translation. They studied the effects of different degrees of bead embedding and cell height within a geometrically linear range of cell deformation. They report that the relationships between applied torque and bead rotation or translation is linear up to bead rotations of 15°, above which geometrical nonlinearities become significant. They also show that even though the bead rotates, the torque is nearly constant over each cycle.

7.3.2 Optical tweezers

In optical tweezers (OT), a microbead bound to membrane receptors is trapped in a focused laser beam and is used as a handle to apply oscillatory force to the cellular membrane and cytoskeleton. The trap is kept at a fixed position while the experimental chamber is subjected to a sinusoidal displacement by moving the specimen translation stage at frequencies discretely varying in the range of 0.05 to 50 Hz. The displacements of the chamber and of the bead are recorded with a CCD camera at rates up to 500 Hz with trigger pulses synchronized with the stage motion. The displacement of the bead from the center of the trap gives the force exerted, while the cellular deformation is given by the relative displacement between the chamber and the bead. The force and the deformation have relative nonzero phase, so must be represented as complex numbers, a ratio of that gives the complex modulus of elasticity (G_e) within a scaling factor.

Both the magnetic twisting cytometry and optical tweezers have their own advantages and limitations. MTC offers wide bandwidth (up to 1 kHz), but the strain measurements are confounded by simultaneous rotation and translation. Also, because a macroscopic magnetometer placed outside the specimen can only detect the *averaged* remnant magnetic moments of all beads present in the specimen, the measurement of strain is not truly local unless low bandwidth video imaging is used for translation measurement. On the other hand, optical tweezers can apply a purely translational stress and measure the local strain of each particle. However, the strength of the force is limited by laser power, and

the bandwidth of force exertion is limited by the mechanical response of the specimen-translation stage. Additionally, both of the techniques suffer by the geometry dependence of the stress. Because the site of bead-cell interface undergoes a local deformation, the actual stress delivered depends on the interface geometry, which is largely uncontrollable an usually unobservable. It has been reported, however, that the geometry dependence can be accounted for by introducing a factor that can either be computed numerically using finite element simulations [111] or be calculated using analytical expressions [92, 94].

7.3.3 Oscillatory magnetic bead rheometer

Sackmann and collaborators [55, 108] reported a novel rheometer based on oscillatory motion of a magnetic bead induced using electromagnets. Unlike MTC, their technique uses superparamagnetic beads and exerts lateral stress, thus avoiding bead rotations and restricting the strain to be translational. The bandwidth of stress exertion is only limited by the properties of the magnetic-core material (beyond 1 kHz); however, the measurement of magnetic bead translation had to be done using video imaging, limited to approximately 50Hz to 100 Hz.

I present an extension of the oscillatory magnetic bead rheometer by exploiting the synergy between the high-bandwidth stress exertion ability of the 3DFM electromagnets with high bandwidth local- strain-measurement ability of laser interferometry on magnetic beads. In the 3DFM, lateral magnetic forces with frequencies up to 5 kHz can be exerted, whereas the position of the bead can be detected at rates only limited by the QPD response, for now 10 kHz. Also,

while it is barely debatable that the complex mechanical properties of biological specimens are anisotropic tensor fields, the state-of-the-art techniques described above facilitate only one-dimensional measurements of those properties. Using the 3DFM, it is possible to exert forces in multiple dimensions simultaneously, which provides a more complete measurement of mechanical properties. I prefer to call the tool a *frequency- response analyzer* because its application scope is broader than rheology, which is only concerned with flow-related properties of a material. For example, using the technique, mechanical (as opposed to rheological) properties of a single strand of fibrin fiber or a cilium can be analyzed by oscillating an attached bead. The remainder of this chapter is organized as follows. First, I will present a 3DFM-magnet-excitation scheme to produce a force that revolves around covering all directions in the specimen plane, along with simulation results. Then, I will provide preliminary, proof-of-concept, experimental results comparing thus-measured frequency response of a Newtonian fluid and of a cellular membrane with their respective expected responses.

7.4 Three-dimensional magnetic force microscopy (3DFM)

The 3DFM is our custom-design microscope that offers high bandwidth micromanipulation combined with nanoscale measurements, enabling a broad variety of biological studies. As the name suggests, manipulation involves applying magnetic forces to magnetic particles attached to a biological object (e.g. a beating cilium, a cell membrane, etc) or suspended in a biological environment (e.g. cytoplasm, mucus, etc). The position of the particle is followed

in 3D using BFP laser interferometry or in 2D using bright-field imaging, and the mechanical properties of interest are extracted. For the application at hand, we use BFP laser interferometry augmented by Agnostic Tracking, which has been described in previous chapters. A detailed description of the electromagnetic force exertion system will follow.

7.4.1 Magnetic subsystem: Introduction

Beginning with Crick's [112] in-vitro studies of the viscoelastic properties of cytoplasm in 1949, magnetic forces have been used to investigate a wide range of biophysical properties and phenomena at the cellular and sub-cellular levels. These instruments offer force sensitivity on par with the most sensitive probe-based techniques, facilitate non-invasive manipulation, are relatively inexpensive, and may be used for high-throughput, parallel investigations. Two generations of 3DFM were developed in our lab, each distinguished by their unique electromagnetic system. The results reported here were obtained on the second generation, a thin-foil based assembly that offers electromagnetic field bandwidths beyond 3 kHz in combination with full 4π steradians of force directionality. I will briefly review the concepts of electromagnetism and will refer the reader to our instrumentation paper for the detailed description of the system.

7.4.2 The theory of electromagnetism

Electromagnetism is a phenomenon where an electric current passing through a conductor produces a magnetic field around the conductor, or vice versa. A simple electromagnet is a solenoid, where multiple turns of a current carrying conductor are wound around a core to produce higher magnetic flux in

the core. If *N* is the number of turns and *I* is the current passing through the conductor, the magneto-motive force (mmf) induced in the magnetic circuit is,

$$mmf = NI$$

Analogous to the electromotive force (emf) producing an electric field, the magneto motive force produces a magnetic field. Magnetic reluctance (S) is the resistance of a material to the magnetic field. Magnetic reluctance of any part of a magnetic circuit that has a length *l* and a cross-sectional area *a* is given by,

$$S = \frac{l}{\mu a}$$

Where, μ is the permeability of the material, an intrinsic property.

Magnetic flux (Φ), is a measure of magnetism, a quantity analogous to current in an electric circuit. Thus, magnetic flux is related to magnetomotive force and magnetic reluctance by,

$$\Phi = \frac{mmf}{S}$$

Because the flux preferentially adopts a path of least magnetic reluctance, permeability and dimensions of the core can be selected to channel the flux to a desired place.

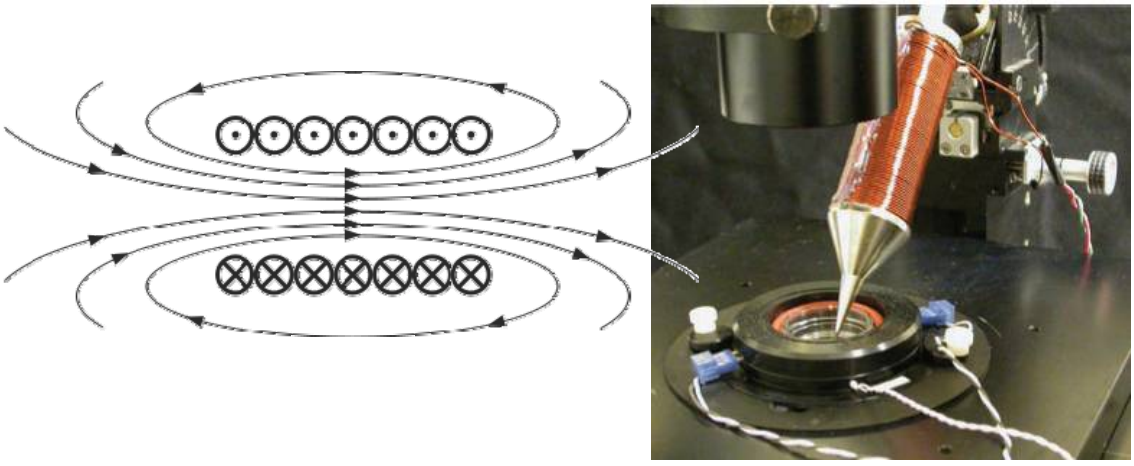

Figure 7-1: Solenoid, the simplest electromagnet

Magnetic flux density (*B*) is defined as the magnetic flux passing through a unit area, so

$$B = \frac{\Phi}{a}$$

Figure 7-1 shows an illustration of a solenoid (left) and a photograph of a simple solenoid with a tapered tip (right). Here the flux is channeled through the tapered tip because of high relative permeability of the core magnetic material compared to surrounding air. By means of reducing the cross-sectional area, the tapering provides for high flux density at the tip. As we will see momentarily, greater magnetic field density produces higher force on a magnetic particle.

7.4.3 Forces on magnetic particles

Force on a magnetic particle is caused by an interaction between its magnetic dipole moment $\vec{m}$ and the gradient $\nabla \vec{B}$ of an incident magnetic field. For a soft, magnetically-permeable particle, $\vec{m}$ is entirely induced by the incident field. When the magnetic particle is not saturated,

$$\vec{m} = \frac{\pi d^3}{2\mu_0}\left(\frac{\mu_r - 1}{\mu_r + 2}\right)\vec{B},$$

where μ_o is the permeability of free space in SI units, μ_r is the relative permeability of the particle, and *d* is the diameter of the particle. The magnetic force is,

$$\vec{F} = \nabla\left(\vec{m} \bullet \vec{B}\right) = \frac{\pi d^3}{4\mu_0}\left(\frac{\mu_r - 1}{\mu_r + 2}\right)\nabla\left(\left|\vec{B}\right|^2\right). \qquad \text{Equation 7.5}$$

The field is usually produced by multiple electromagnet pole tips arranged in space to provide the necessary directional capability. Except very near a pole tip, the field's behavior can be modeled by a monopole. According to this model, the magnitude of $\vec{B}$ from a singly excited magnetic pole is proportional to $B_p / \left|\vec{r}\right|^2$, where B_p is the pole strength and $\vec{r}$ is the vector connecting the particle to the pole in the direction toward the pole. Omitting the constant terms in Equation 7.5, force on a magnetic particle can be modeled as

$$\vec{F} \propto \nabla\left(\left|\vec{B}\right|^2\right) \propto \frac{B_p^2}{\left|\vec{r}\right|^5}\tilde{r} \qquad \text{Equation 7.6}$$

Where $\tilde{r}$ is the unit vector in the direction of $\vec{r}$.

If $\vec{B}$ at the location of the particle is higher than the particle's saturation limit, $\vec{m}$ is fixed and independent of $\vec{B}$. So, force is

$$\mathbf{F} = \nabla\left(\vec{m} \bullet \vec{B}\right) = \vec{m}_{Max}\nabla\left(\left|\vec{B}\right|\right)$$

So, in relative terms,

$$\mathbf{F} \propto \nabla\left(\left|\vec{B}\right|\right) \propto \frac{\left|B_p\right|}{\left|\vec{r}\right|^3}\tilde{r} \qquad \text{Equation 7.7}$$

7.4.4 Electromagnet design and implementation

Other people of the 3DFM team contributed to the design and implementation of the electromagnetic system. Hence, I refer the reader to our instrumentation paper [48] for a detailed account of the design and implementation of the electromagnetic system of the 3DFM.

7.4.5 Electromagnet system characterization

I will present characterization of the two primary design features relevant for a frequency response analyzer. Firstly, I will present verification of the force directionality, thus to support the claim that we can oscillate a bead in all directions and determine the complete tensor field of mechanical properties. Secondly, I will present the bandwidth characterization of the electromagnetic system.

7.4.5.1 Force magnitude and directionality

To verify the ability to pull in all directions, the large-scale magnetic symmetry is demonstrated by pulling a 2.8 μm superparamagnetic bead (M-280; Dynal Biotech, Oslo, Norway) towards each magnetic axis of symmetry (Figure 7-2a). This required 26 different excitations; towards each of the six pole tips individually, between two adjacent poles, and between each set of three adjacent poles. Large blue rods indicate pole locations, whereas light dots indicate directions of measured bead motion in response to the force. For each of the 26 excitations, the pole tip was energized for 3 seconds, with the excitation order arranged so that the bead returned to the center of the geometry after every 2 excitations. In this experiment, movement in the expected direction is seen, but is

off from the expected location by 6 to 12 degrees (depending on the axis of rotation). The deviation of the lab coordinate system from its theoretical location is most likely the source of this difference.

Fine control of bead position is demonstrated in Figure 7-2(b). Here, force vectors were generated to sample the angle space between three poles, filling one octant of the surface of the sphere. Forces were applied in each direction for 3 seconds, with the bead being returned back to the origin after each excitation via a force in the opposite direction. The small-scale bead control (filling of the octant) shown in Figure 7-2(b), combined with the symmetry data of Figure 7-2(a) indicates that we would be able to fill all 8 octants on the surface of the sphere, and thus, pull the bead in all directions.

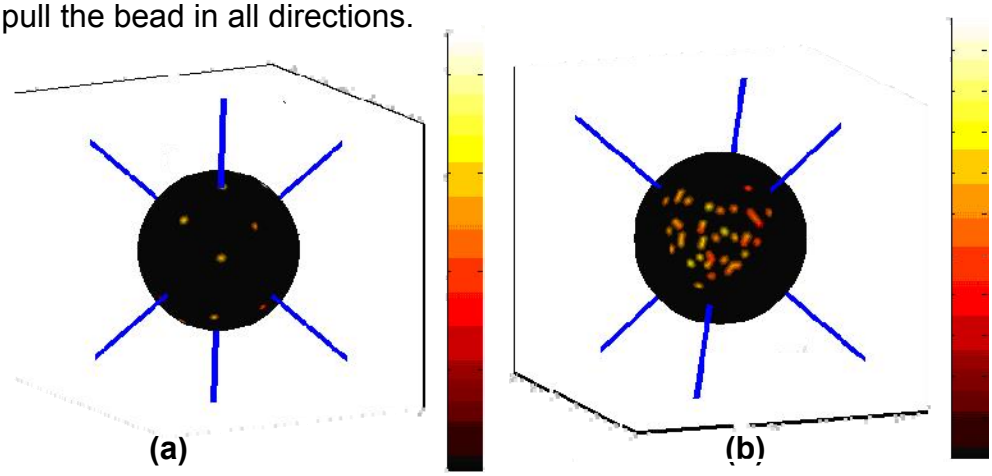

Figure 7-2: Characterization of force directionality

7.4.5.2 Bandwidth characterization

To determine the force bandwidth of the magnetic system, 1 micron super paramagnetic beads were oscillated between opposite poles in a planar, six pole geometry. Test frequencies were varied from 2 Hz to 4 kHz in a discrete manner. To account for the artifacts introduced by motion of the bead relative to the poles,

a control-sinusoid was superimposed on each test frequency. Motion of the bead was measured by laser tracking at 10 kHz. The response to each test frequency was determined in four steps. First, I took PSD of the bead position over the time-window over which excitation at that test-frequency was applied. Second, the height of the peak at the test-frequency was converted in terms of bead motion amplitude by integrating the corresponding peaks in PSD. Third, for the same time-window, I computed the response to the control frequency in the manner identical to that for the response to the test-frequencies. Finally, the response to test-frequencies was normalized by the response to the control frequency. As shown in Figure 7-3, this analysis revealed that the -3dB roll off in the response function is beyond 3 kHz.

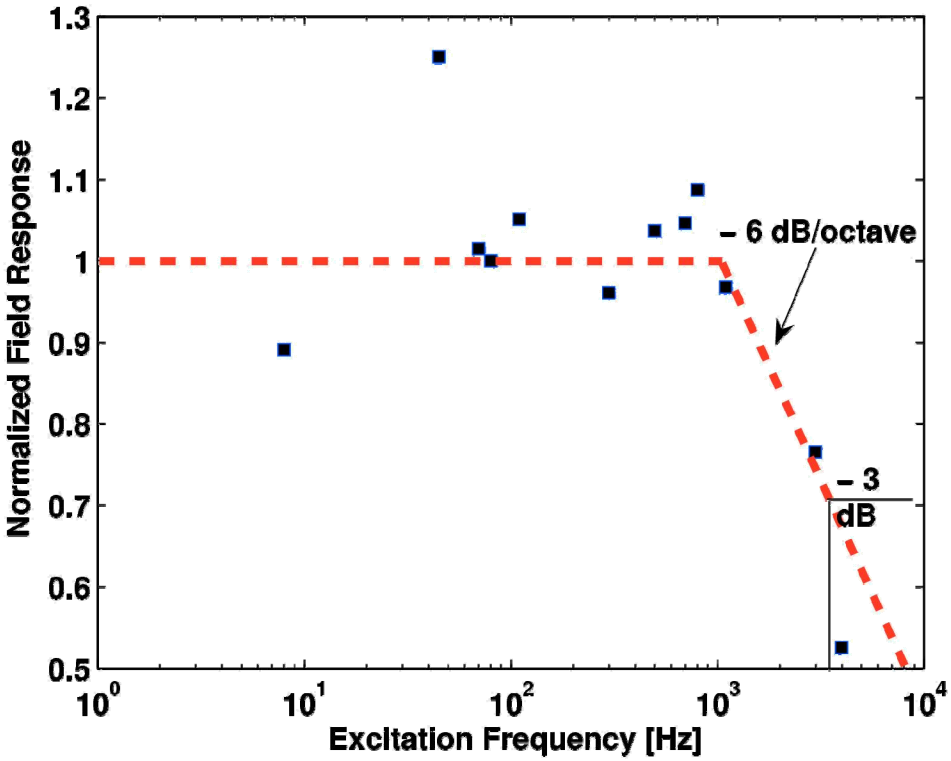

Figure 7-3: Characterization of electromagnet bandwidth

7.5 Pole geometry selection and excitation scheme

Because of the magnetic flux conservation, a geometry with only two poles will always cause equal strength for each pole, irrespective of which pole is explicitly energized. Thus, a particle at the center of the geometry will not feel any force, while a particle off of the center will be monotonically pulled towards the nearest pole. Clearly, a two-pole geometry cannot be used to exert oscillatory forces on a particle. As we saw earlier, a six-pole FCC geometry can be used to pull in any direction, thus can be used to exert oscillatory forces. However, using an FCC geometry requires both top and bottom drive rings, which considerably reduces the operable height of the specimen. Also, many biological specimens are locally planar or two dimensional, e.g., a cellular membrane. I will demonstrate using simulations that a three-pole or a four-pole planar geometry can produce forces in any direction in the specimen plane. I limited experiments to 2D oscillatory forces, and used a three-pole planar geometry.

7.6 Simulated forces based on the Point-charge model

As mentioned previously in Equation 7.6 and 7.7, the field generated by sharp-tip electromagnets can be approximated by a point-charge model, except very near the tip. When multiple poles are present, Equation 7.6 (for unsaturated bead) changes to:

$$\vec{F} \propto \nabla\left(\left|\vec{B}\right|^2\right) \propto \sum_i \frac{B_{pi}^2}{\left|\vec{r}_i\right|^5}\tilde{r}_i \qquad \text{Equation 7.8}$$

Where, the subscript *i* indicates i^{th} pole.

Equation 7.7, for a saturated bead, changes to:

$$\vec{F} \propto \nabla\left(\left|\vec{B}\right|\right) \propto \sum_i \frac{\left|B_{pi}\right|}{\left|\vec{r}_i\right|^3}\tilde{r}_i \qquad \text{Equation 7.9}$$

I will use these equations to verify the excitation schemes for both three pole and four pole geometries.

7.6.1 Case 1: Bead not saturated

Figure 7-4 shows simulated forces exerted on an unsaturated bead by a three-pole planar geometry. The three red dots in the plot on the left represent the point charges or pole tips. The black dot in the center represents location of the magnetic bead. The pole tips are assumed to be in the same Z plane as the bead. The blue arrows indicate the direction of force being applied. As seen, force is applied in all directions within the plane. The top-right plot shows how the components of the force vary with time. The bottom-right plot shows the coil excitations that are used to generate the force. For this case, three sinusoids with 1Hz frequency and 120^o relative phase shift are used as the three coil currents.

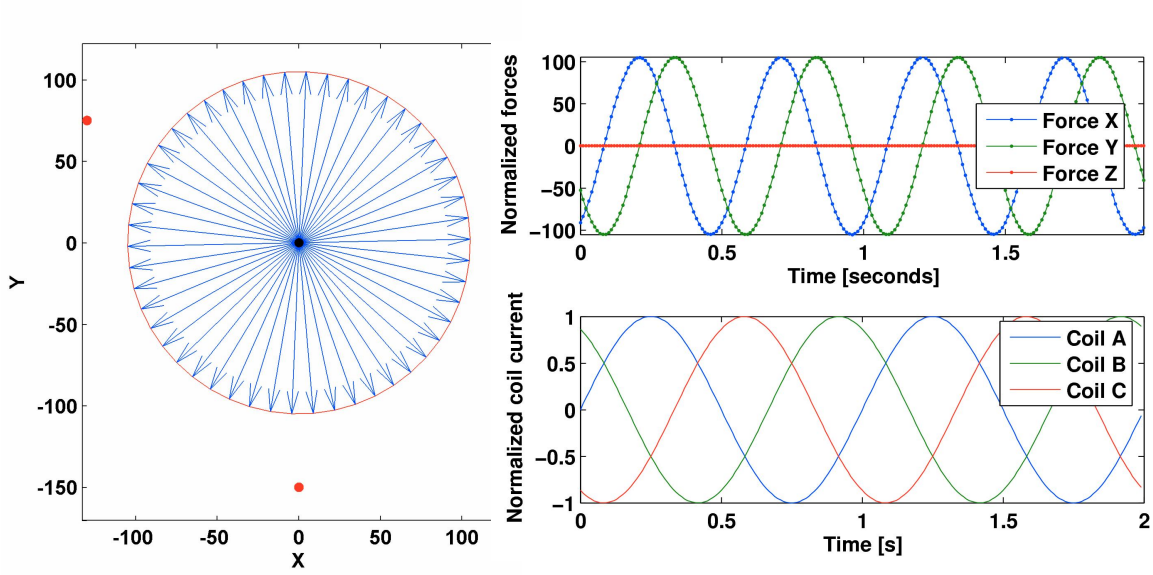

Figure 7-4: Simulated Force: unsaturated bead, 3-pole geometry

Figure 7-5 shows similar simulation results using a four-pole planar geometry. Again, as seen, it is possible to exert force in all directions within the specimen plane.

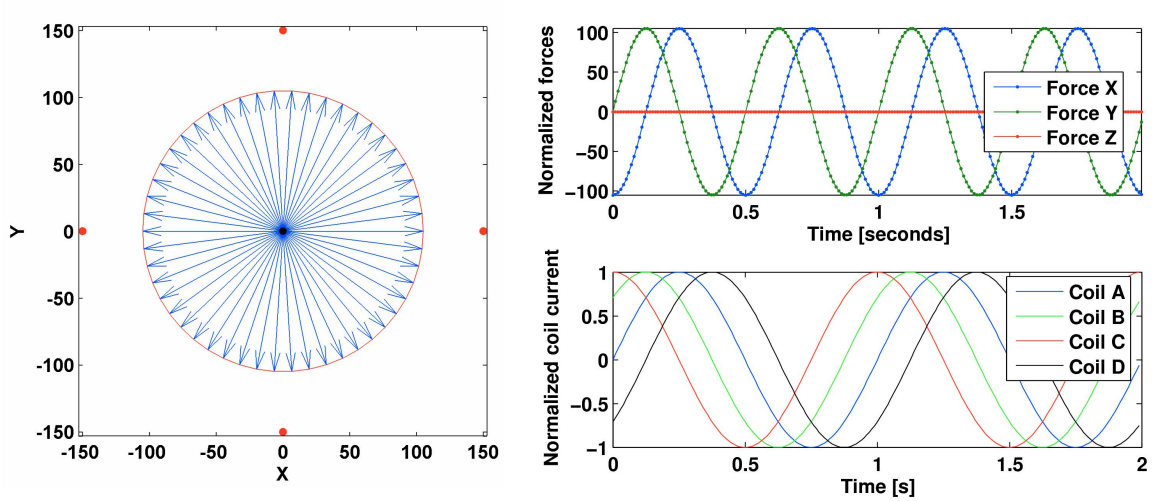

Figure 7-5: Simulated forces: unsaturated bead, 4-pole geometry

Thus, when the bead is unsaturated, both three-pole and four-pole geometries can produce sinusoidal force in all directions in the plane of the specimen. However, superparamagnetic beads have very low susceptibility and

saturate at relatively weak fields. In many experiments, it is desired to obtain higher forces and thus operate in the regime where the bead is saturated. Next, I present simulations for the case when the bead is saturated.

7.6.2 Case 2: Bead saturated

Figure 7-6 shows simulation results for a saturated bead pulled by a three-pole geometry. As seen, the XY components of the force are no longer sinusoidal; however, the force vectors do cover all directions in the specimen plane. As I will describe later, I account for up to four harmonics when determining the frequency response. Also, using the power-spectral-density of the simulated forces, I found that compared to the fundamental frequency, the higher-than-2nd harmonics in the force cycles produced here are weaker by at least three orders of magnitudes. thus are negligible.

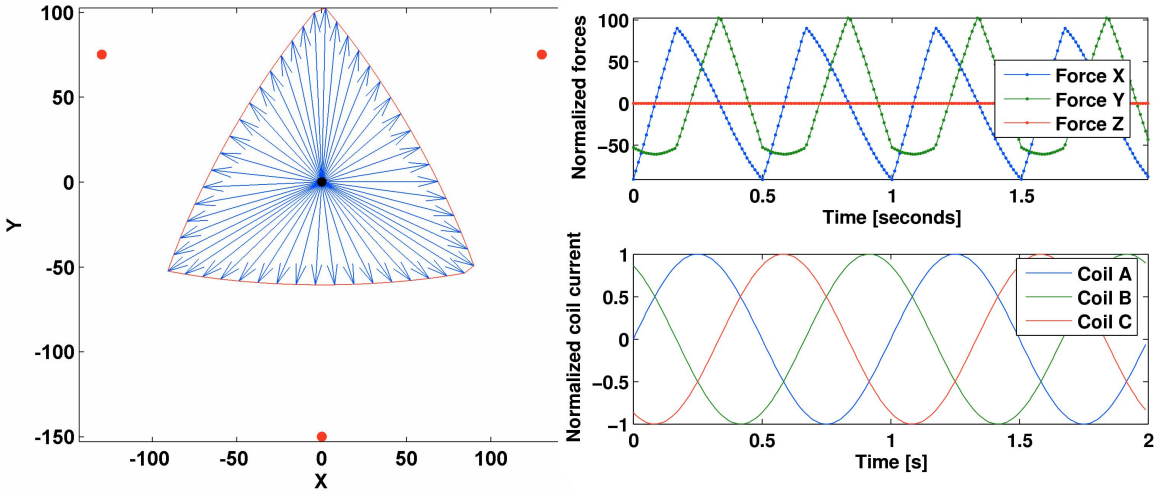

Figure 7-6: Simulated forces: saturated bead, 3-pole geometry

As we would expect, the excitation scheme for the four-pole geometry can be improvised not to produce harmonic distortions when the bead is saturated. Figure 7-7 shows results of the related simulation. As seen, the force

components are purely sinusoidal, and force vectors uniformly cover all directions of the specimen plane. This is achieved by adjusting relative phases of the excitation sinusoids and energizing only one pair of poles at a time, the active pair revolves with the direction of the force. Three points are noteworthy:

1. Because the excitation scheme is different compared to the unsaturated bead, the user must make a decision a priori about whether the expected level of bead-magnetization is in the saturated regime or the unsaturated regime.
2. Unlike the unsaturated case, the frequency of the force sinusoid is the same as the excitation frequency.
3. Here the coil currents are forced to reverse their polarities every time they reach zero. This scheme ensures inbuilt degauss and prevents remanence from building up in the pole tips.

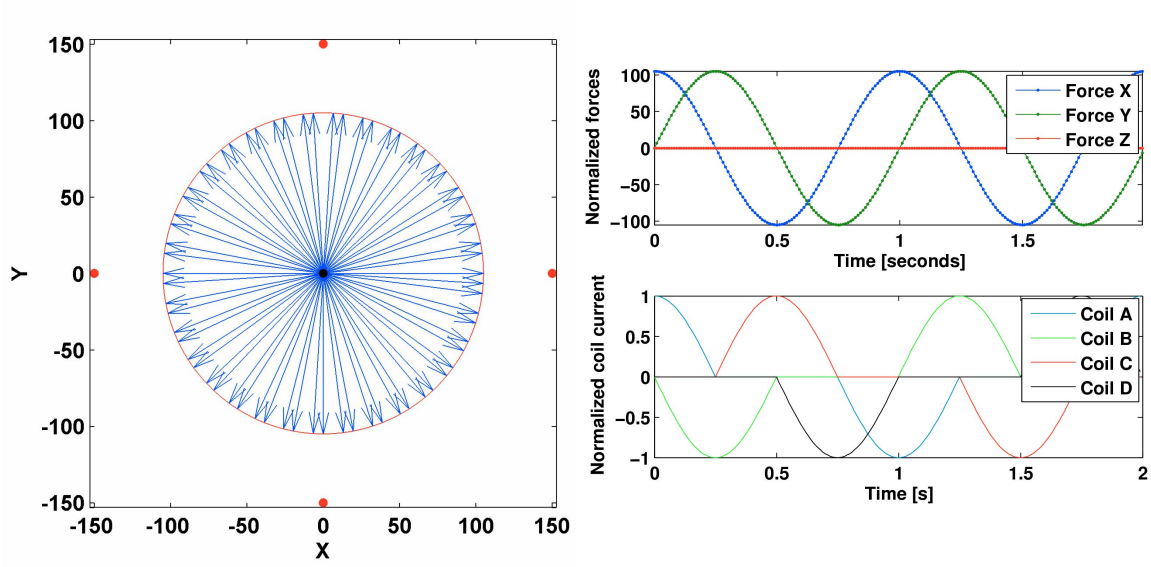

Figure 7-7: Simulated forces: saturated bead, 4-pole geometry

7.7 Experimental Results

In the previous section, we saw that both planar geometries, three pole and four pole, can be used to exert oscillatory forces that spatially revolve to cover all directions in the specimen plane. This section presents experimental characterization of the technique using the three-pole geometry.

7.7.1 Karo solution

Here, 2.8 um diameter superparamagnetic particles are suspended in a Karo solution. The specimen is then put into the 3DFM magnetic stage and a particle is aligned with the center of a three-pole geometry and the coils are energized in the manner described in section 7.6.1. The frequency of the excitation sinusoid is discretely varied in geometric progression from 1 Hz to 1 kHz, and 10 cycles of each frequency are applied. Because aligning the particle in the exact center of the geometry is difficult, even a sinusoidal force causes a net motion of the particle towards the nearest pole. To account for this motion, an excitation burst of control-frequency sinusoids (150 Hz) was interleaved between each pair of test frequencies. The position of the bead was measured at 10 kHz using laser tracking. The analysis procedure was as follows:

1. Segment the position-vs-time trace such that each segment has only one test frequency followed by a control-frequency burst.
2. For each segment, compute two PSDs: one for the bead position during the test-frequency burst, and one for the same during the control-frequency burst.

3. Say the excitation frequency during the segment is *f*. Pick the first four harmonics, i.e., *f*, *2f*, *3f* and *4f*, and integrate the peaks at each of the four harmonics in both of the PSDs computed. Because the dimension of PSD is power / frequency, integrating a peak over its adjacent bins (usually two) gives the power accumulated in that particular peak. Let us say for a particular harmonic, the power obtained for the test burst is P_t and that for the control burst is P_c.
4. Execute step 3 for a PSD of passive diffusion of the same bead. For peaks at each harmonic, subtract the power obtained for passive diffusion, say P_d, from both the power obtained for test burst and the power obtained for control burst. Say, for a particular harmonic, the results are ($P'_t = P_t - P_d$), and ($P'_c = P_c - P_d$).
5. Sum the P'_t and P'_c for all four harmonics of the excitation frequency. Normalize the result for the test burst with the result for the control burst. This number shows how the induced bead motion varies with the excitation frequency.
6. Take square root of the result in step 5 to convert from power to displacement; multiply it by the excitation frequency, and plot it against the excitation frequency. According to Stoke's law for a Newtonian fluid, the amplitude of the motion in response to an external force is inversely proportional to the frequency of the external force; so multiplying by the frequency should produce a number independent of the frequency.

Figure 7-8 shows the plot created by following these steps. As seen, the experimental data follows the theoretical model fairly well for frequencies higher

than 10 Hz. However, for the frequencies below 10 Hz, the experimental data shows large discrepancies. One possible explanation is that interleaving of the control frequency burst is not adequate to account for the monotonic motion of the bead at low frequencies. For example, 10 cycles of 1 Hz cause monotonic motion of the bead for 10 seconds, thus the amplitude of the response may change significantly during the test frequency burst itself. An interleaved control frequency burst can only account for the change between two test frequency bursts, but not for the change within a test frequency burst.

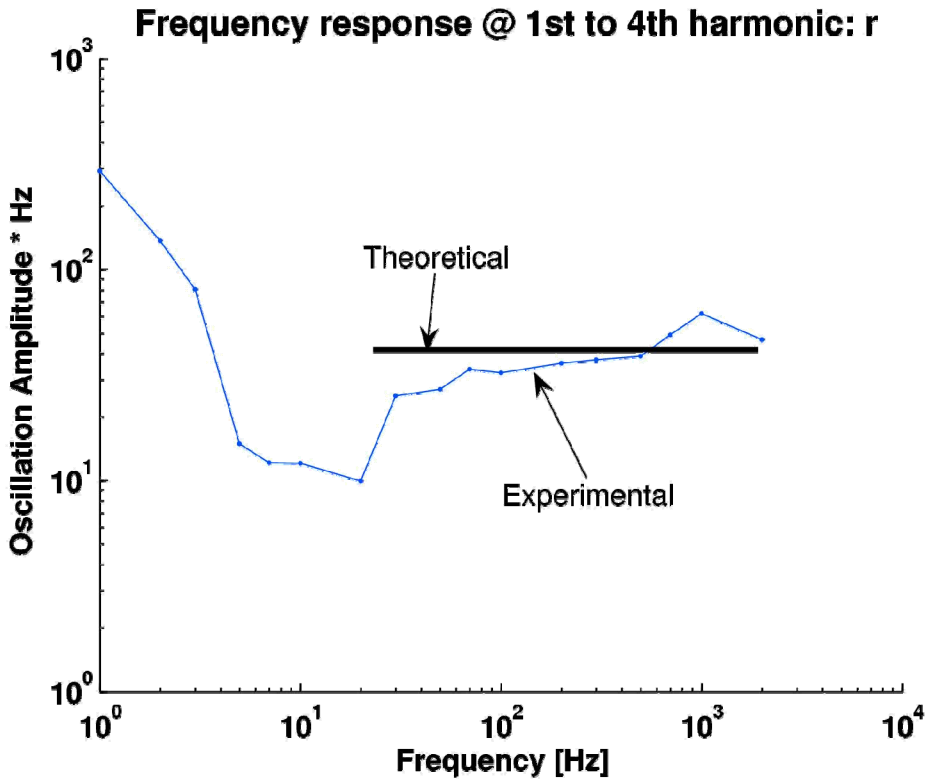

Figure 7-8: Measuring frequency response of Karo

7.7.2 HBC (M-231) cell membrane

As reviewed in section 7.1, understanding mechanical properties of a cell membrane over a wide range of time scales is desirable. Here I produce an

experimental result obtained by applying the frequency-response analyzer tool to a live cellular membrane.

7.7.2.1 Cell culture

M-231 human breast cancer-derived cells were obtained from collaborators (Gary Johnson and Kenneth Jacobsen, UNC-CH) and from the Lineberger Tissue Culture facility, UNC-CH. Cells were grown at 37° C in DMEM medium (Gibco) and 10% FBS (HyClone, Inc) in tissue culture flasks until needed. For experiments, the cells were trypsinized and plated onto UV cleaned 24 x 50 mm glass #1.5 coverslips. After at least one day, 2.8 μm, COOH, superparamagnetic beads were attached to the cell surface. Cells were then returned to the incubator for 30 min. The cells were then rinsed several times with PBS and then fresh medium to remove unattached beads.

Cells on the coverslips were then placed within the magnetic stage and a silicon grease ring drawn about the cell region. Imaging was carried out with Nikon 100x 1.3 NA oil Plan Fluor or 60x 1.2 NA water objective.

7.7.2.2 Frequency response analysis

The method of oscillatory force exertion, data collection and data analysis were identical to that for Karo; except, because the bead is attached to a cell, it does not monotonically move towards a pole; so control frequencies were not applied. Figure 7-9 shows the results. As seen, the frequency dependence of the response in terms of power exhibits an exponent of 0.75, giving 0.375 as the exponent in terms of bead motion amplitude. This exponent characterizing the frequency dependence of the material response in terms of strain (motion

amplitude) is known as alpha (α). Several studies have reported various values of alpha[92, 101]. Even though the value 0.375 is slightly different than the mean value reported by others for the characteristic exponent for membranes of various cells (approximately 0.2), it is within the range of published values (i.e. 0.15 to 0.5).

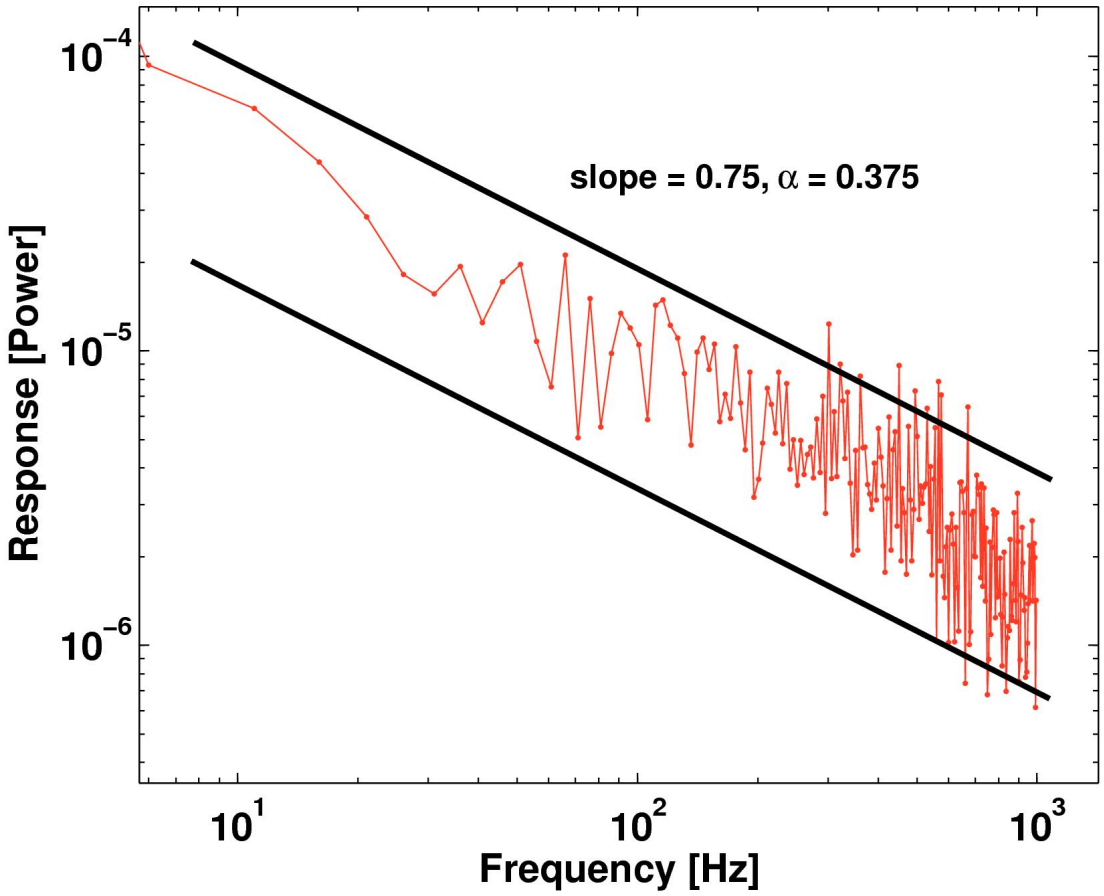

Figure 7-9: Measuring frequency response of a cell membrane

7.8 Summary

In this chapter we have visited a novel technique to probe mechanical properties of biological objects at the nanoscale, and with high bandwidth. Two experimental results were presented: calibrating the frequency response of a Newtonian fluid, and measuring the frequency response of a live cell membrane. Several advancements are possible, e.g. using four-pole geometry to better control the frequency characteristics of force exerted, superimposing the control frequency burst instead of interleaving it, etc. In spite of a few discrepancies from the standard values, the results are encouragingly in an agreement. The improvements described above may resolve the discrepancies and promote the utility of the technique.

Chapter 8 Applications : Probing cellular mechanics

This chapter presents two novel biophysical phenomena, whose investigation was enabled by Agnostic Tracking. First, an anchoring-dependent nonlinear response of a cell membrane was observed upon application of a step force. Second, a previously unknown grouping was revealed in the diffusion characteristics of the vesicles in a live cytoplasm. Also, plausible explanations to each phenomenon will be offered.

8.1 Anchoring-dependent nonlinear response of a cell membrane

The physical properties of the plasma membrane have been probed by a number of methods, from high speed video to experiments with the laser trap. Many interesting phenomenon have been observed, from subdiffusive to superdiffusive behavior, caused by proposed structures such as corrals and lipid rafts [9, 113-115]. I here present a comparison of the behavior of beads anchored to the outer leaflet of the plasma membrane versus anchored through a transmembrane link to the cytoskeleton. Also, traditionally, cell membranes have been modeled as linear systems [101, 116, 117]. I here report nonlinear dynamics in membrane mechanics upon application of an external step force. I also show that the phenomenon can be used as a test for whether a particular protein is peripheral or integral.

8.1.1 Method

To obtain specific linkages to GPI anchors (glycosylphosphatidylinositol) or β-1 Integrin receptors, we added biotinylated mouse anti-human CD73 (a gift from Ken Jacobson's lab, UNC-CH) antibody or β1 (CD29) antibodies to IMR-90 (human lung fibroblast) cells for 15 minutes; then washed, and added Streptavidin (SA) coated 1 um diameter supraparamagnetic beads (Dynal, Inc) for 30 minutes (Figure 8-1). These were then rinsed with medium, and the cells were placed in our magnetic stage on the 3DFM. The beads were pulled using the magnetic fields with a force in the range of 25 pN to 100 pN, and their position was tracked in 3D at 10 kHz using Agnostic Tracking.

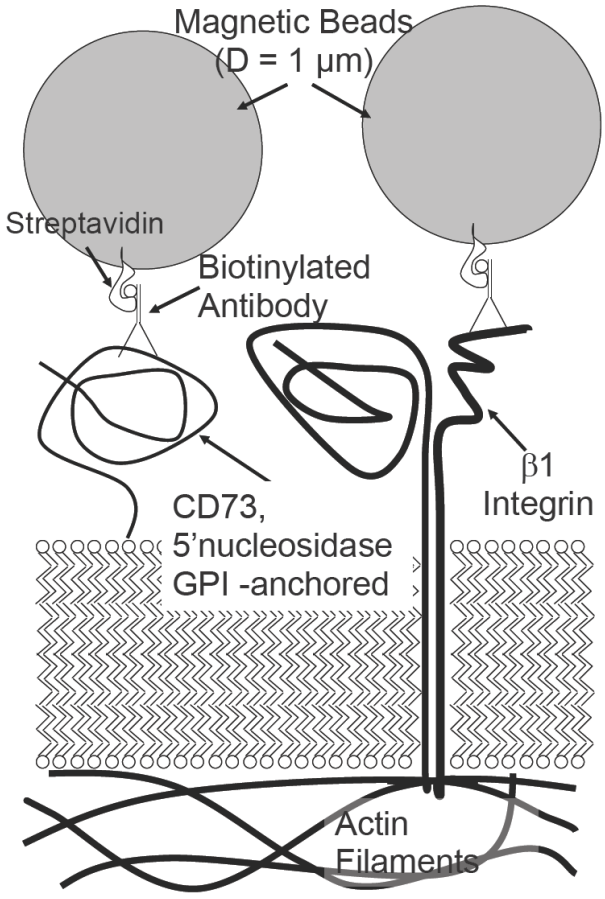

Figure 8-1: Two types of bead anchoring on cell membrane

8.1.2 Results

In the absence of a magnetic force, the GPI-anchored beads showed significantly higher thermal fluctuations compared to the β1-Integrin-anchored beads. The difference in the amplitude of thermal fluctuations may be because the Integrin receptors are directly connected to the cytoskeleton, while the GPI anchors are not. Interestingly, the thermal fluctuations of GPI-anchored beads were greatly suppressed when magnetic force was active, whereas the Integrin-anchored beads did not show any change in thermal fluctuations upon application of force (Figure 8-2).

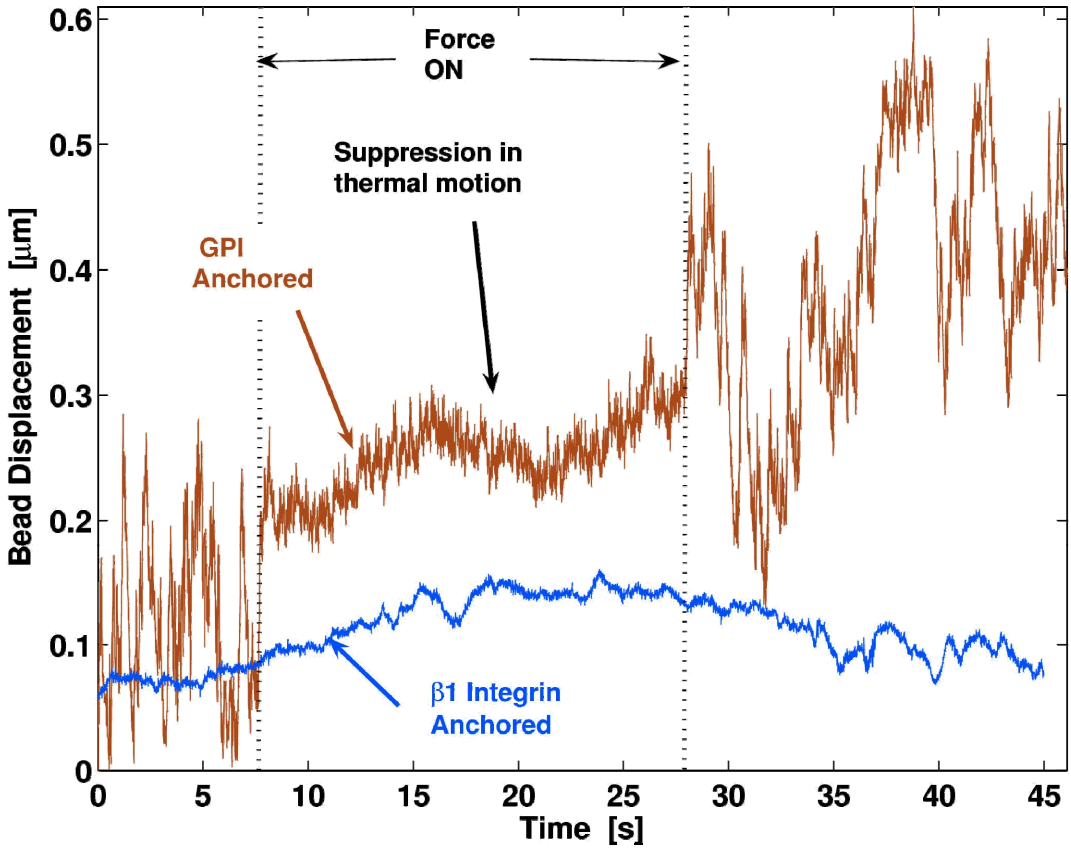

Figure 8-2: Position traces of membrane-anchored beads

To further investigate the nature of the quick suppression, we explored a novel analysis approach. We observed the time-dependence of the power-spectral-density (PSD) of the bead motion.

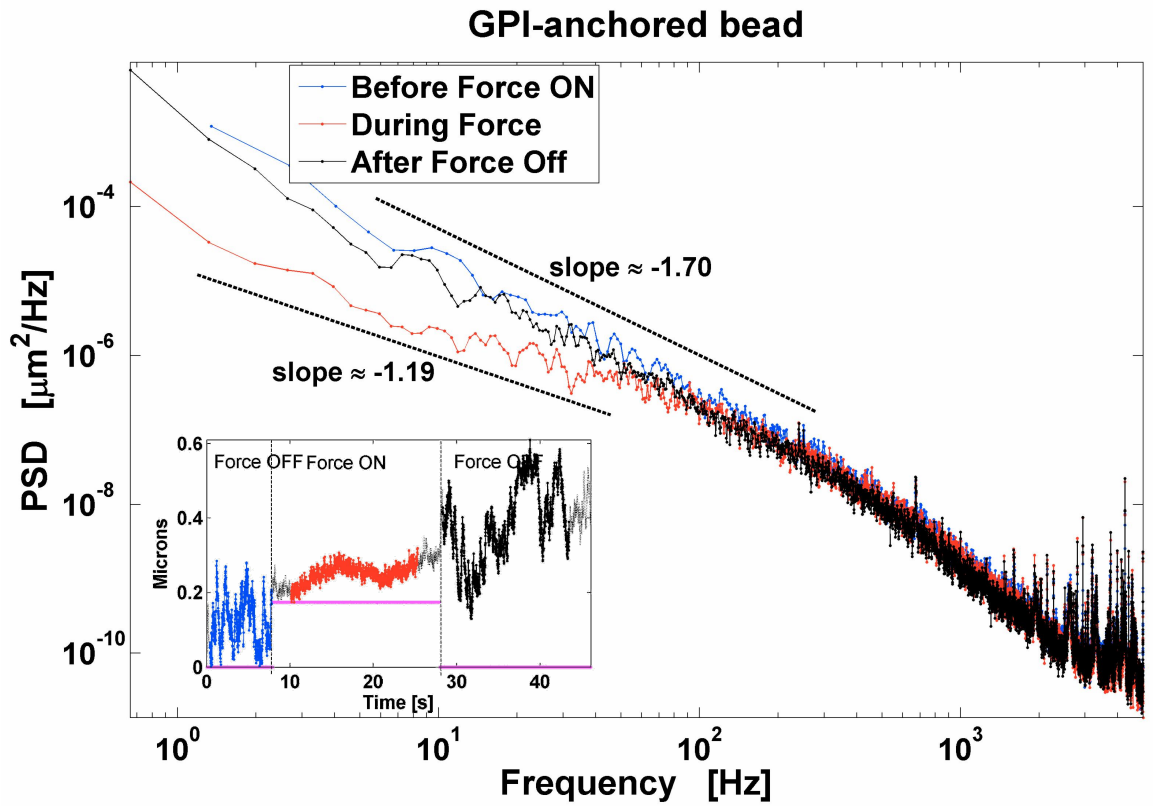

Figure 8-3: PSD of thermal motion of a GPI-anchored bead

Figure 8-3 shows three PSD curves for the bead motion before force application, during force application, and after force turned off. The position trace of a GPI bead is provided in the inset. The color of a section in the inset matches with the color of the associated PSD curve.

8.1.3 Discussion

As observed in Figure 8-3, an application of force causes the PSD curve to bend to an approximately -1.2 slope for lower frequencies (< 100 Hz); while the behavior at higher frequencies (< 300 Hz) remains unaffected. Thus the

suppressions of the thermal fluctuations as observed in the time domain is not distributed evenly across the whole spectrum. This nonlinear suppression implies a fundamental change in the environment of the bead. I hypothesize that the force pushes the bead against the barriers of the membrane skeleton; hence the dynamics of the membrane skeleton are reflected in the bead motion. As another explanation, the membrane itself may stiffen upon application of the force; however, stiffening at this time scales (< 0.01 s) seems unlikely and has not been reported so far. Additional controls may reveal further insights into the mechanism behind the phenomenon.

As a separate interesting observation, the suppression phenomenon can be used as a test to determine whether a specific protein (i.e., the target of the bead-labeling antibody) is peripheral or integral. A bead anchored to an integral protein (e.g. Integrin) –which is attached to the cytoskeleton-- will not show any suppression in the thermal fluctuations upon application of external force; where as a bead anchored to a peripheral protein (e.g., GPI) will show the suppression.

8.2 Organelle diffusion inside live cytoplasm

Understanding viscoelastic properties of the cytoplasm is an active area of research in the field of biophysics. One appealing approach for probing properties of the cytoplasm is to analyze the diffusive or molecular-motor driven motion of endoplasmic particles. The particle being tracked could be a microinjected or phagocytosed bead [77, 118-121], or it could be an endogenous vesicle [78, 122] or molecule [123]. Magnetic beads can also be ingested by cells

and pulled by magnetic fields to study cytoplasmic response to external mechanical stimuli [2, 124, 125]. Because neither diffusive nor driven motion is constrained to be in the image plane, 3D position detection is usually desired. Measurement of viscoelastic modulus with high bandwidth requires high temporal resolution, while detection of molecular-motor steps requires nanoscale spatial resolution. I demonstrate the utility of the high spatiotemporal resolution offered by our technique for tracking 3D motion of endogenous vesicles. The ability to track the vesicles in their native states without labeling is an added advantage of using laser-scattering based position detection. Also, because we use a low-power, non-trapping laser, the natural motion of vesicles is not inhibited; and because we use position feedback, we are able to track a long range motion of vesicles.

8.2.1 Method

Xenopus melanophore cells were a gift from Vladimir Gelfand (Northwestern University). These cells are grown in L-15 medium at room temperature. They were trypsinized and plated onto glass coverslips as described, and used within 4 days of plating. The motion of individual melanosomes was followed using Agnostic Tracking.

M-231 cells were cultured as mentioned in the previous section.

8.2.2 Results

Figure 8-4(a) shows the position of a melanosome diffusing inside a live Xenopus melanophore cell measured over time, while Figure 8-4(b) depicts the

same trace in 3D. A preliminary characterization of maximum velocities gave approximately 700 nm/ sec, which is comparable to the literature values [126].

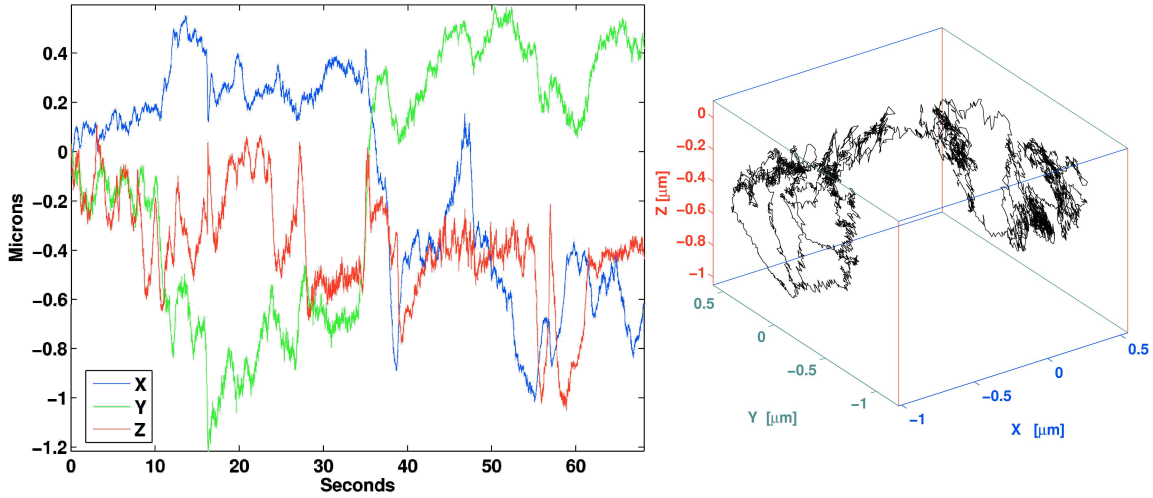

(a) (b)

Figure 8-4: A melanosome diffusing inside a live melanophore

We use mean-square-displacement (msd) as a function of window length as a measurement of viscoelastic properties. Figure 8-5 shows ensemble of such curves produced by tracking six organelles inside live Human Breast Cancer (M-231) cells. Each curve is shifted in the Y-axis by a normalization routine in order to collapse the ensemble and enable easy comparison of slopes. A group of organelles exhibit a 0.66-power law for the whole range of τ , which is consistent with previously reported values for organelle diffusion in cytoplasm based on experiments [122] as well as theory [127, 128]. This agreement demonstrates applicability of our approach for tracking unlabelled vesicles. Also, at shorter time scales (< 0.01 s) a group of vesicles exhibit a 0.41-power law; which, to the best of our knowledge, has never been reported for particle diffusion in cytoplasm. Although the organelles were chosen from multiple cells, no clear correlation

between grouping of the msd curves and cells existed. The result has interesting implications.

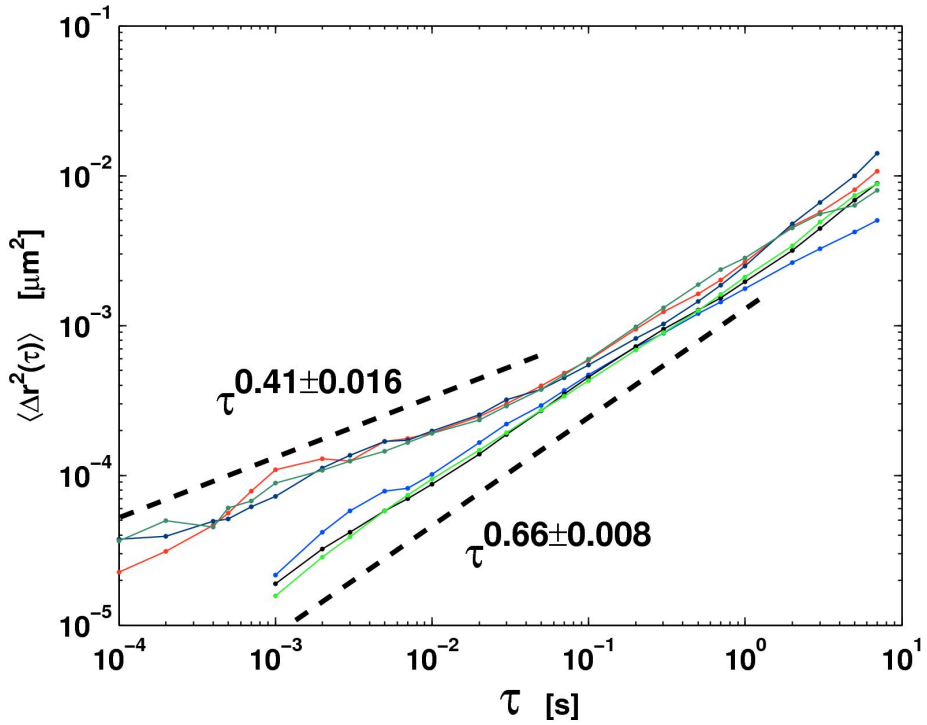

Figure 8-5: Novel grouping of vesicular diffusive behavior

8.2.3 Discussion

For a particle diffusing in an entangled network of polymers, a 0.75 power law would suggest that the polymers comprising the network are semiflexible, which are characterized by large molecular cross section, i.e. the ratio of persistence length to the molecular diameter [129]. On the other hand, a power law in the range of 0.5 to 0.66 would suggest presence of flexible polymers [130, 131], characterized by smaller molecular cross section, or shorter persistence length. It is known that mainly three kinds of polymers are present in cytoplasm: F-Actin, Microtubules, and intermediate filaments. F-Actin is considered a semiflexible polymer, because its persistence length (L_p≈17 μm) is of the same

order of its contour length ($L_c \approx$ 10-15 μm); while microtubules are considered rigid polymers because of the huge persistence length ($L_p \approx$ 6 mm). Thus, neither F-Actin, nor microtubules can be attributed to the 0.5 slope of msd curves. However, some of the intermediate filaments (e.g. keratin, vimentin) have short persistence length and have been reported to behave as flexible polymers [132-137].

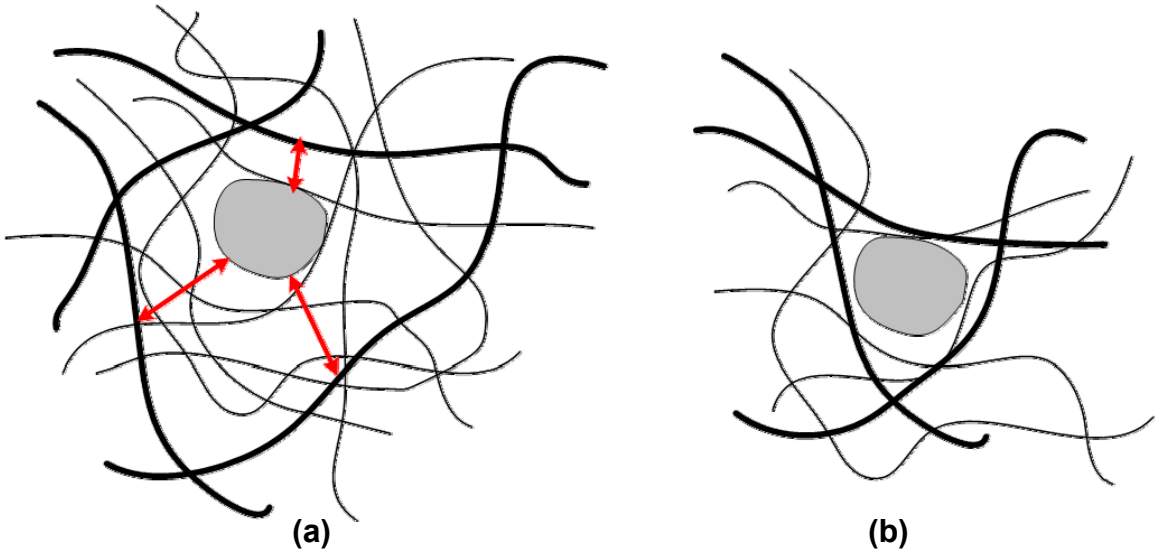

Figure 8-6: A possible explanation for the grouping

The sketch in Figure 8-6 shows two arrangements differing in the characteristic of the polymer network in the neighborhood of the organelle. The thick curves represent semiflexible or rigid polymers (F-Actin, Microtubules etc), whereas the thin curves represent flexible polymers (intermediate filaments). In Figure 8-6(a), a vesicle is immediately surrounded by flexible polymers, while semiflexible filaments are present farther. At short time scales, the vesicle diffuses in the local neighborhood only, thus exhibiting a power law close to 0.5, associated with a flexible polymer network. Longer time scales allow the vesicle

to diffuse farther; thus the dynamics of the semiflexible polymer network are reflected at longer time scales as the 0.66-power law. In Figure 8-6(b), the vesicle is immediately surrounded by semiflexible polymers; thus the vesicle experiences dynamics of a semiflexible polymer network at all time scales. Also, in the experimental data in Figure 8-5, after normalizing such that the curves coincide at longer time scales, the 0.41 power-law part is above the 0.66 power law part. This observation suggests that a 0.41 power law is associated with relatively higher energy in the bead motion; which is again consistent with the sketch in Figure 8-6(a), because the motion at that time scale is only constrained by the flexible polymer network.

The proposed explanation for the grouping of MSD curves among vesicles of the same cell type suggests that the heterogeneity of the cytoplasm can be characterized based on the slope of MSD curves at short time scales; and the characterization may further be used to determine the environment of a particular organelle and thus location of the organelle with reference to cytoplasm. It is noteworthy that the high-bandwidth capability of Agnostic Tracking enables the MSD analysis at time scales shorter than those offered by video tracking. Also, because we can track the long range motion of an organelle, observing the MSD curves over several short window spans may reveal the cytoplasmic itinerary followed by a particular vesicle in order to carry out a particular task.

APPENDIX A: BIAS AND VARIANCE OF THE COEFFICIENT ESTIMATES

Considering only X-axis component of Equation 3.5,

$$\hat{\beta}_k^x = \left(\overline{R_k}^T \overline{R_k}\right)^{-1} \overline{R_k}^T \overline{S}_{Lx}$$

$$= \left(\overline{R_k}^T \overline{R_k}\right)^{-1} \overline{R_k}^T \left(\overline{R_k}\beta_k^x + \overline{\varepsilon}_x\right) \qquad \left\langle \because \overline{S}_{Lx} = \overline{R_k}\beta_k^x + \overline{\varepsilon}_x \right\rangle$$

$$= \left(\overline{R_k}^T \overline{R_k}\right)^{-1} \overline{R_k}^T \overline{R_k}\beta_k^x + \left(\overline{R_k}^T \overline{R_k}\right)^{-1} \overline{R_k}^T \left(\overline{\varepsilon}_x\right)$$

$$\hat{\beta}_k^x = \beta_k^x + \left(\overline{R_k}^T \overline{R_k}\right)^{-1} \overline{R_k}^T \left(\overline{\varepsilon}_x\right) \qquad \text{Equation A.1}$$

Taking expected values on both sides of Equation A.1,

$$E\left[\hat{\beta}_k^x \middle| \overline{R_k}\right] = E\left[\beta_k^x + \left(\overline{R_k}^T \overline{R_k}\right)^{-1} \overline{R_k}^T \left(\overline{\varepsilon}_x\right) \middle| \overline{R_k}\right]$$

$$= \beta_k^x + \left(\overline{R_k}^T \overline{R_k}\right)^{-1} E\left[\overline{\varepsilon}_x \middle| \overline{R_k}\right]$$

For offline estimation, $\overline{\varepsilon}_x = \overline{\varepsilon}'_x - \overline{P}_{Sx}$, so

$$E\left[\hat{\beta}_k^x \middle| \overline{R_k}\right] = \beta_k^x + \left(\overline{R_k}^T \overline{R_k}\right)^{-1} \left(E\left[\overline{\varepsilon}'_x \middle| \overline{R_k}\right] + E\left[\overline{P}_{Sx} \middle| \overline{R_k}\right]\right)$$

Assuming that 2nd order polynomial adequately describes the true F_{QP}

$$E\left[\hat{\beta}_k^x \middle| \overline{R_k}\right] = \beta_k^x + \left(\overline{R_k}^T \overline{R_k}\right)^{-1} E\left[\overline{P}_{Sx} \middle| \overline{R_k}\right] \qquad \text{Equation A.2}$$

For on-the-fly estimation, $\overline{\varepsilon}_x = \overline{\varepsilon}'_x - \overline{p}_x$

$$E\left[\hat{\beta}_k^x \middle| \overline{R_k}\right] = \beta_k^x + \left(\overline{R_k}^T \overline{R_k}\right)^{-1} \left(E\left[\overline{\varepsilon}'_x \middle| \overline{R_k}\right] + E\left[\overline{p}_x \middle| \overline{R_k}\right]\right)$$

Assuming that 2nd order polynomial adequately describes the true F_{QP}

$$E\left[\hat{\beta}_k^x \middle| \overline{R_k}\right] = \beta_k^x + \left(\overline{R_k}^T \overline{R_k}\right)^{-1} E\left[\overline{p}_x \middle| \overline{R_k}\right] \qquad \text{Equation A.3}$$

Taking variance on both sides of Equation A.1,

$$\sigma^2\left[\hat{\beta}_k^x \middle| \overline{R}_k\right] = \sigma^2\left[\left(\overline{R_k}^T \overline{R_k}\right)^{-1} \overline{R_k}^T \left(\overline{\varepsilon}_x\right) \middle| \overline{R}_k\right]$$

$$= \left(\overline{R_k}^T \overline{R_k}\right)^{-1} \overline{R_k}^T \sigma^2\left[\overline{\varepsilon}_x \middle| \overline{R}_k\right] \overline{R_k} \left(\overline{R_k}^T \overline{R_k}\right)^{-1}$$

$$= \sigma^2\left[\overline{\varepsilon}_x \middle| \overline{R}_k\right] \left(\overline{R_k}^T \overline{R_k}\right)^{-1} \overline{R_k}^T \overline{R_k} \left(\overline{R_k}^T \overline{R_k}\right)^{-1}$$

$$= \sigma^2\left[\overline{\varepsilon}_x \middle| \overline{R}_k\right] \left(\overline{R_k}^T \overline{R_k}\right)^{-1}$$

$$= \frac{\sigma^2\left[\overline{\varepsilon}_x \middle| \overline{R}_k\right]}{\sum_{n=0}^{N} R_{k\langle n\rangle}{}^2} \qquad \left\langle \because \overline{R}_k = R_{k\langle n\rangle} \qquad n = 0,1,2,...,N \right\rangle$$

For offline estimation, $\overline{\varepsilon}_x = \overline{\varepsilon}'_x - \overline{P}_{Sx}$, so

$$\sigma^2\left[\hat{\beta}_k^x \middle| \overline{R}_k\right] = \frac{\sigma^2\left[\overline{\varepsilon}'_x \middle| \overline{R}_k\right] + \sigma^2\left[\overline{P}_{Sx} \middle| \overline{R}_k\right]}{\sum_{n=0}^{N} R_{k\langle n\rangle}{}^2} \qquad \text{Equation A.4}$$

For on-the-fly estimation, $\overline{\varepsilon}_x = \overline{\varepsilon}'_x - \overline{p}_x$, so

$$\sigma^2\left[\hat{\beta}_k^x \middle| \overline{R}_k\right] = \frac{\sigma^2\left[\overline{\varepsilon}'_x \middle| \overline{R}_k\right] + \sigma^2\left[\overline{p}_x \middle| \overline{R}_k\right]}{\sum_{n=0}^{N} R_{k\langle n\rangle}{}^2} \qquad \text{Equation A.5}$$

REFERENCES

1. Crick, F.H.C., Hughes, A. F. W., *The Physical Properties of Cytoplasm: A Study By Means Of The Magnetic Particle Method.* Experimental Cell Research, 1949. **Suppl. 1**(37).

2. Yagi, K., *The mechanical and colloidal properties of Amoeba protoplasm and their relations to the mechanism of amoeboid movement.* Comparative Biochemistry and Physiology, 1961. **3**(2): p. 73-80.

3. Abercrombie, M., J.E.M. Heaysman, and S.M. Pegrum, *The locomotion of fibroblasts in culture : III. Movements of particles on the dorsal surface of the leading lamella.* Experimental Cell Research, 1970. **62**(2-3): p. 389-398.

4. Abercrombie, M., J.E.M. Heaysman, and S.M. Pegrum, *The locomotion of fibroblasts in culture I. Movements of the leading edge.* Experimental Cell Research, 1970. **59**(3): p. 393-398.

5. Barak, L.S. and W.W. Webb, *Diffusion of low density lipoprotein-receptor complex on human fibroblasts.* J. Cell Biol., 1982. **95**(3): p. 846-852.

6. Debrabander, M., et al., *Probing Microtubule-Dependent Intracellular Motility with Nanometer Particle Video Ultramicroscopy (Nanovid Ultramicroscopy).* Cytobios, 1985. **43**(174): p. 273-283.

7. Schnapp, B.J., J. Gelles, and M.P. Sheetz, *Nanometer-Scale Measurements Using Video Light-Microscopy.* Cell Motility and the Cytoskeleton, 1988. **10**(1-2): p. 47-53.

8. Saxton, M.J., *Single-Particle Tracking - Effects of Corrals.* Biophysical Journal, 1995. **69**(2): p. 389-398.

9. Kusumi, A. and Y. Sako, *Cell surface organization by the membrane skeleton.* Current Opinion in Cell Biology, 1996. **8**(4): p. 566-574.

10. Saxton, M.J. and K. Jacobson, *SINGLE-PARTICLE TRACKING:Applications to Membrane Dynamics.* Annual Review of Biophysics and Biomolecular Structure, 1997. **26**(1): p. 373-399.

11. Geerts, H., et al., *Nanovid Tracking, a New Automatic Method Based on Colloidal and Video Microscopy for the Study of Motility in Living Cells.* Archives Internationales De Physiologie De Biochimie Et De Biophysique, 1986. **94**(4): p. Bp1-Bp1.

12. Geerts, H., et al., *Nanovid Tracking - a New Automatic Method for the Study of Mobility in Living Cells Based on Colloidal Gold and Video Microscopy.* Biophysical Journal, 1987. **52**(5): p. 775-782.

13. Geerts, H., M. de Brabander, and R. Nuydens, *Nanovid microscopy.* Nature, 1991. **351**(6329): p. 765-766.

14. Allen, R.D., N.S. Allen, and J.L. Travis, *Video-enhanced contrast, differential interference contrast (AVEC-DIC) microscopy: A new method capable of analyzing microtubule-related motility in the reticulopodial network of allogromia laticollaris.* Cell Motility and the Cytoskeleton, 1981. **1**(3): p. 291-302.

15. Gelles, J., B.J. Schnapp, and M.P. Sheetz, *Tracking kinesin-driven movements with nanometre-scale precision.* Nature, 1988. **331**(6155): p. 450-453.

16. Schnapp, B.J., J. Gelles, and M.P. Sheetz, *Nanometer-scale measurements using video light microscopy.* Cell Motility and the Cytoskeleton, 1988. **10**(1-2): p. 47-53.

17. Sheetz, M.P. and S.C. Kuo, *Tracking Nanometer Movements of Single Motor Molecules*, in *Methods in Cell Biology, Vol 39*. 1993. p. 129-136.

18. Fujiwara, T., et al., *Phospholipids undergo hop diffusion in compartmentalized cell membrane.* J. Cell Biol., 2002. **157**(6): p. 1071-1082.

19. Murase, K., et al., *Ultrafine Membrane Compartments for Molecular Diffusion as Revealed by Single Molecule Techniques.* Biophys. J., 2004. **86**(6): p. 4075-4093.

20. Yildiz, A., et al., *Myosin V Walks Hand-Over-Hand: Single Fluorophore Imaging with 1.5-nm Localization.* Science, 2003. **300**(5628): p. 2061-2065.

21. Yildiz, A. and P.R. Selvin, *Fluorescence Imaging with One Nanometer Accuracy: Application to Molecular Motors.* Acc. Chem. Res., 2005. **38**(7): p. 574-582.

22. Speidel, M., Jon A., and E.L. Florin, *Three-dimensional tracking of fluorescent nanoparticles with subnanometer precision by use of off-focus imaging.* Optics Letters, 2003. **28**: p. 69-71.

23. Levi, V., Q.Q. Ruan, and E. Gratton, *3-D Particle Tracking in a Two-Photon Microscope: Application to the Study of Molecular Dynamics in Cells.* Biophysical Journal, 2005. **88**: p. 2919-2928.

24. Levi, V., et al., *Scanning FCS, a novel method for three-dimensional particle tracking.* Biochem Soc Trans, 2003. **31**(Pt 5): p. 997-1000.

25. Kis-Petikova, K., Gratton, E., *Distance measurement by circular scanning of the excitation beam in the two-photon microscope.* Microscopy Research and Technique, 2004. **63**(1): p. 34-49.

26. Dietrich, C., et al., *Relationship of Lipid Rafts to Transient Confinement Zones Detected by Single Particle Tracking.* Biophys. J., 2002. **82**(1): p. 274-284.

27. Tilney, L.G. and D.A. Portnoy, *Actin filaments and the growth, movement, and spread of the intracellular bacterial parasite, Listeria monocytogenes.* J Cell Biol, 1989. **109**(4 Pt 1): p. 1597-608.

28. Mounier, J., et al., *Intracellular and cell-to-cell spread of Listeria monocytogenes involves interaction with F-actin in the enterocytelike cell line Caco-2.* Infect Immun, 1990. **58**(4): p. 1048-58.

29. Theriot, J.A., et al., *Involvement of profilin in the actin-based motility of L. monocytogenes in cells and in cell-free extracts.* Cell, 1994. **76**(3): p. 505-17.

30. Salathe, M., K.B. Adler, and R.C. Boucher, eds. *Cilia and Mucus: From Development to Respiratory Defense*. 2001, Dekker: New York.

31. Allersma, M.W., et al., *Two-dimensional tracking of ncd motility by back focal plane interferometry.* Biophysical Journal, 1998. **74**(2): p. 1074-1085.

32. Ghislain, L.P., N.A. Switz, and W.W. Webb, *Measurement of Small Forces Using an Optical Trap.* Review of Scientific Instruments, 1994. **65**(9): p. 2762-2768.

33. Ghislain, L.P. and W.W. Webb, *Scanning-force microscope based on an optical trap.* Optics Letters, 1993. **18**(19): p. 1678-1680.

34. Gittes, F. and C.F. Schmidt, *Back-focal-plane detection of force and motion in optical traps.* Biophysical Journal, 1998. **74**(2): p. A183-A183.

35. Gittes, F. and C.F. Schmidt, *Interference model for back-focal-plane displacement detection in optical tweezers.* Optics Letters, 1998. **23**(1): p. 7-9.

36. Peters, I.M., et al., *Three dimensional single-particle tracking with nanometer resolution.* Review of Scientific Instruments, 1998. **69**(7): p. 2762-2766.

37. Pralle, A., et al., *Three-dimensional high-resolution particle tracking for optical tweezers by forward scattered light.* Microsc Res Tech, 1999. **44**(5): p. 378-86.

38. Lang, M.J., et al., *An automated two-dimensional optical force clamp for single molecule studies.* Biophysical Journal, 2002. **83**(1): p. 491-501.

39. Visscher, K. and S.M. Block, *Versatile optical traps with feedback control*, in *Molecular Motors and the Cytoskeleton, Pt B*. 1998. p. 460-489.

40. Visscher, K., S.P. Gross, and S.M. Block, *Construction of multiple-beam optical traps with nanometer-resolution position sensing.* Ieee Journal of Selected Topics in Quantum Electronics, 1996. **2**(4): p. 1066-1076.

41. Visscher, K., M.J. Schnitzer, and S.M. Block, *Single kinesin molecules studied with a molecular force clamp.* Nature, 1999. **400**(6740): p. 184-189.

42. Rohrbach, A. and E.H.K. Stelzer, *Three-dimensional position detection of optically trapped dielectric particles.* Journal of Applied Physics, 2002. **91**(8): p. 5474-5488.

43. Rohrbach, A. and E.H.K. Stelzer, *Trapping forces, force constants, and potential depths for dielectric spheres in the presence of spherical aberrations.* Applied Optics, 2002. **41**(13): p. 2494-2507.

44. Rohrbach, A., H. Kress, and E.H.K. Stelzer, *Three-dimensional tracking of small spheres in focused laser beams: influence of the detection angular aperture.* Opt. Lett, 2003. **28**: p. 411-413.

45. Amblard, F., et al., *A magnetic manipulator for studying local rheology and micromechanical properties of biological systems.* Review of Scientific Instruments, 1996. **67**(3): p. 818-827.

46. Assi, F., et al., *Massively parallel adhesion and reactivity measurements using simple and inexpensive magnetic tweezers.* Journal of Applied Physics, 2002. **92**(9): p. 5584-5586.

47. Barbic, M., et al., *Scanning probe electromagnetic tweezers.* Applied Physics Letters, 2001. **79**(12): p. 1897-1899.

48. Fisher, J.K., et al., *Thin-foil magnetic force system for high-numerical-aperture microscopy.* Review of Scientific Instruments, 2006. **77**(2): p. 023702.

49. Fisher, J.K., et al., *Three-dimensional force microscope: A nanometric optical tracking and magnetic manipulation system for the biomedical sciences.* Review of Scientific Instruments, 2005. **76**(5): p. 053711-11.

50. Gosse, C. and V. Croquette, *Magnetic tweezers: micromanipulation and force measurement at the molecular level.* Biophys J, 2002. **82**(6): p. 3314-29.

51. Haber, C. and D. Wirtz, *Magnetic tweezers for DNA micromanipulation.* Review of Scientific Instruments, 2000. **71**(12): p. 4561-4570.

52. Huang, H., et al., *Three-dimensional cellular deformation analysis with a two-photon magnetic manipulator workstation.* Biophys J, 2002. **82**(4): p. 2211-23.

53. Strick, T.R., et al., *The elasticity of a single supercoiled DNA molecule.* Science, 1996. **271**(5257): p. 1835-7.

54. Valberg, P.A. and D.F. Albertini, *Cytoplasmic motions, rheology, and structure probed by a novel magnetic particle method.* J Cell Biol, 1985. **101**(1): p. 130-40.

55. Ziemann, F., J. Radler, and E. Sackmann, *Local measurements of viscoelastic moduli of entangled actin networks using an oscillating magnetic bead micro-rheometer.* Biophys J, 1994. **66**(6): p. 2210-6.

56. Liu, Y., et al., *Evidence for localized cell heating induced by infrared optical tweezers.* Biophys J, 1995. **68**(5): p. 2137-44.

57. Peterman, E.J.G., et al., *Optical tweezer experiments: Temperature effects and back focal plane interferometry.* Biophysical Journal, 2001. **80**(1): p. 73a-73a.

58. Peterman, E.J.G., F. Gittes, and C.F. Schmidt, *Laser-induced heating in optical traps.* Biophysical Journal, 2003. **84**(2): p. 1308-1316.

59. Schonle, A. and S.W. Hell, *Heating by absorption in the focus of an objective lens.* Optics Letters, 1998. **23**(5): p. 325-327.

60. Born, M. and E. Wolf, *Principles of Optics, 6th edition.* Pergamon Press, 1980.

61. Stone, M.H., *The Generalized Weierstrass Approximation Theorem*. 1948, JSTOR. p. 237-254.

62. Kleinbaum, D.G., L.L. Kupper, and K.E. Muller, *Applied regression analysis and other multivariable methods*. 2nd ed. 1988, Boston, Mass.: PWS-Kent Pub. Co. 228-250.

63. Weisberg, S., *Applied linear regression*. 2nd ed. Wiley series in probability and mathematical statistics. Applied probability and statistics,. 1985, New York: Wiley. 42-43.

64. Rohrbach, A., et al., *Trapping and tracking a local probe with a photonic force microscope.* Review of Scientific Instruments, 2004. **75**(6): p. 2197-2210.

65. Welch, G. and G. Bishop, *An Introduction to the Kalman Filter*, in *Technical Reports*. 1995, Department of Computer Science, University of North Carolina: Chapel Hill. p. TR95-041.

66. Musoff, H. and P. Zarchan, *Fundamentals Of Kalman Filtering: A Practical Approach*. 2 ed. Progress in Astronautics and Aeronautics. Vol. 190. 2005: Americal Institue for Aeronautics and Astronautics (AIAA).

67. Kalman, R.E., *A New Approach to Linear Filtering and Prediction Problems.* Transactions of the ASME -- Journal of Basic Engineering, 1960. **82**(D): p. 35-45.

68. Einstein, A. and R. Furth, *Investigations on the theory of Brownian movement*. 1956, New York: Dover Publications.

69. Brown, R., *A brief account of microscopical observations made in the months of June, July and August, 1827, on the particles contained in the pollen of plants; and on the general existence of active molecules in organic and inorganic bodies.* Edinburgh new Philosophical Journal, 1828(July-September): p. 358-371.

70. Mason, T.G., et al., *Particle Tracking Microrheology of Complex Fluids.* Physical Review Letters, 1997. **79**(17): p. 3282.

71. Mathlouthi, M. and J. Génotelle, *Rheological properties of sucrose solutions and suspensions*. Sucrose: properties and applications, ed. M. Mathlouthi and P. Reiser. 1995, London: Blakie Academicd & Professional. 126-154.

72. Lawson, C.L. and R.J. Hanson, *Solving least squares problems*. 1974: Prentice-Hall Englewood Cliffs, NJ.

73. Pierre, D.A., *Optimization Theory with Applications*. 1986: Dover Publications.

74. Kreyszig, E., *Advanced engineering mathematics*. 1993: Wiley New York.

75. Janmey, P.A., *The cytoskeleton and cell signaling: Component localization and mechanical coupling.* Physiological Reviews, 1998. **78**(3): p. 763-781.

76. Lau, A.W.C., et al., *Microrheology, Stress Fluctuations, and Active Behavior of Living Cells.* Physical Review Letters, 2003. **91**(19): p. 198101-4.

77. Tseng, Y., T.P. Kole, and D. Wirtz, *Micromechanical Mapping of Live Cells by Multiple-Particle-Tracking Microrheology.* Biophys. J., 2002. **83**(6): p. 3162-3176.

78. Yamada, S., D. Wirtz, and S.C. Kuo, *Mechanics of living cells measured by laser tracking microrheology.* Biophysical Journal, 2000. **78**(4): p. 1736-1747.

79. Gittes, F., et al., *Microscopic Viscoelasticity: Shear Moduli of Soft Materials Determined from Thermal Fluctuations.* Physical Review Letters, 1997. **79**(17): p. 3286.

80. Ghislain, L.P., I. Brustmascher, and W.W. Webb, *Force and Membrane Compliance Measurements Using an Optical Trap and Laser Interferometry.* Biophysical Journal, 1993. **64**(2): p. A109-A109.

81. Sato, M., et al., *Local mechanical properties measured by atomic force microscopy for cultured bovine endothelial cells exposed to shear stress.* Journal of Biomechanics, 2000. **33**(1): p. 127-135.

82. Rotsch, C., K. Jacobson, and M. Radmacher, *Dimensional and mechanical dynamics of active and stable edges in motile fibroblasts investigated by using atomic force microscopy.* PNAS, 1999. **96**(3): p. 921-926.

83. Alcaraz, J., et al., *Microrheology of Human Lung Epithelial Cells Measured by Atomic Force Microscopy.* Biophys. J., 2003. **84**(3): p. 2071-2079.

84. Sato, M., et al., *Application of the micropipette technique to the measurement of cultured porcine aortic endothelial cell viscoelastic properties.* J Biomech Eng, 1990. **112**(3): p. 263-8.

85. Petersen, N.O., W.B. McConnaughey, and E.L. Elson, *Dependence of Locally Measured Cellular Deformability on Position on the Cell, Temperature, and Cytochalasin B.* PNAS, 1982. **79**(17): p. 5327-5331.

86. Dewey, C.F., Jr., et al., *The dynamic response of vascular endothelial cells to fluid shear stress.* J Biomech Eng, 1981. **103**(3): p. 177-85.

87. Barbee, K.A., P.F. Davies, and R. Lal, *Shear Stress-Induced Reorganization of the Surface-Topography of Living Endothelial-Cells Imaged by Atomic-Force Microscopy.* Circulation Research, 1994. **74**(1): p. 163-171.

88. Thoumine, O. and A. Ott, *Time scale dependent viscoelastic and contractile regimes in fibroblasts probed by microplate manipulation.* Journal of Cell Science, 1997. **110**: p. 2109-2116.

89. Desprat, N., et al., *Creep Function of a Single Living Cell.* Biophys. J., 2005. **88**(3): p. 2224-2233.

90. Desprat, N., A. Guiroy, and A. Asnacios, *Microplates-based rheometer for a single living cell.* Review of Scientific Instruments, 2006. **77**(5): p. 055111-9.

91. Caille, N., et al., *Contribution of the nucleus to the mechanical properties of endothelial cells.* Journal of Biomechanics, 2002. **35**(2): p. 177-187.

92. Balland, M., et al., *Power laws in microrheology experiments on living cells: Comparative analysis and modeling.* Physical Review E (Statistical, Nonlinear, and Soft Matter Physics), 2006. **74**(2): p. 021911-17.

93. Yanai, M., et al., *Regional rheological differences in locomoting neutrophils.* Am J Physiol Cell Physiol, 2004. **287**(3): p. C603-611.

94. Laurent, V.M., et al., *Assessment of Mechanical Properties of Adherent Living Cells by Bead Micromanipulation: Comparison of Magnetic Twisting*

Cytometry vs Optical Tweezers. Journal of Biomechanical Engineering, 2002. **124**(4): p. 408-421.

95. Balland, M., A. Richert, and F.o. Gallet, *The dissipative contribution of myosin II in the cytoskeleton dynamics of myoblasts.* European Biophysics Journal, 2005. **V34**(3): p. 255-261.

96. Wottawah, F., et al., *Optical rheology of biological cells.* Physical Review Letters, 2005. **94**(9).

97. Guck, J., et al., *The optical stretcher: A novel laser tool to micromanipulate cells.* Biophysical Journal, 2001. **81**(2): p. 767-784.

98. Deng, L., et al., *Localized mechanical stress induces time-dependent actin cytoskeletal remodeling and stiffening in cultured airway smooth muscle cells.* Am J Physiol Cell Physiol, 2004. **287**(2): p. C440-448.

99. Fabry, B., et al., *Implications of heterogeneous bead behavior on cell mechanical properties measured with magnetic twisting cytometry.* Journal of Magnetism and Magnetic Materials, 1999. **194**(1-3): p. 120-125.

100. Laurent, V.M., et al., *Partitioning of Cortical and Deep Cytoskeleton Responses from Transient Magnetic Bead Twisting.* Annals of Biomedical Engineering, 2003. **V31**(10): p. 1263-1278.

101. Lenormand, G., et al., *Linearity and time-scale invariance of the creep function in living cells.* Journal of The Royal Society Interface, 2004. **1**(1): p. 91-97.

102. Meyer, C.J., et al., *Mechanical control of cyclic AMP signalling and gene transcription through integrins.* Nat Cell Biol, 2000. **2**(9): p. 666-668.

103. Ohayon, J., et al., *Analysis of Nonlinear Responses of Adherent Epithelial Cells Probed by Magnetic Bead Twisting: A Finite Element Model Based on a Homogenization Approach.* Journal of Biomechanical Engineering, 2004. **126**(6): p. 685-698.

104. Wang, N., J.P. Butler, and D.E. Ingber, *Mechanotransduction across the cell surface and through the cytoskeleton.* Science, 1993. **260**(5111): p. 1124-1127.

105. Wang, N. and D.E. Ingber, *Probing transmembrane mechanical coupling and cytomechanics using magnetic twisting cytometry.* Biochem Cell Biol, 1995. **73**(7-8): p. 327-35.

106. Fabry, B., et al., *Time scale and other invariants of integrative mechanical behavior in living cells.* Physical Review E (Statistical, Nonlinear, and Soft Matter Physics), 2003. **68**(4): p. 041914-18.

107. Fabry, B., et al., *Scaling the Microrheology of Living Cells.* Physical Review Letters, 2001. **87**(14).

108. Keller, M., J. Schilling, and E. Sackmann, *Oscillatory magnetic bead rheometer for complex fluid microrheometry.* Review of Scientific Instruments, 2001. **72**(9): p. 3626-3634.

109. Maksym, G.N., et al., *Mechanical properties of cultured human airway smooth muscle cells from 0.05 to 0.4 Hz.* Journal of Applied Physiology, 2000. **89**(4): p. 1619-1632.

110. Fabry, B., et al., *Signal Transduction in Smooth Muscle: Selected Contribution: Time course and heterogeneity of contractile responses in cultured human airway smooth muscle cells.* J Appl Physiol, 2001. **91**(2): p. 986-994.

111. Mijailovich, S.M., et al., *A finite element model of cell deformation during magnetic bead twisting.* Journal of Applied Physiology, 2002. **93**(4): p. 1429-1436.

112. Crick, F.H.C. and A.F.W. Hughes, *The physical properties of cytoplasm: a study by means od the magnetic particle method.* Exp. Cell. Res., 1949. **1**: p. 37-80.

113. Kusumi, A., Y. Sako, and M. Yamamoto, *Confined lateral diffusion of membrane receptors as studied by single particle tracking (nanovid microscopy). Effects of calcium-induced differentiation in cultured epithelial cells*. 1993, Biophysical Soc. p. 2021-2040.

114. Edidin, M., S.C. Kuo, and M.P. Sheetz, *Lateral movements of membrane glycoproteins restricted by dynamic cytoplasmic barriers*. 1991. p. 1379.

115. Chen, Y., et al., *Transient anchorage of cross-linked glycosyl-phosphatidylinositol-anchored proteins depends on cholesterol, Src family kinases, caveolin, and phosphoinositides*. 2006, Rockefeller Univ Press. p. 169.

116. Bausch, A.R., et al., *Local Measurements of Viscoelastic Parameters of Adherent Cell Surfaces by Magnetic Bead Microrheometry.* Biophys. J., 1998. **75**(4): p. 2038-2049.

117. Bausch, A.R., W. Moller, and E. Sackmann, *Measurement of Local Viscoelasticity and Forces in Living Cells by Magnetic Tweezers.* Biophysical Journal, 1999. **76**(1): p. 573-579.

118. Caspi, A., R. Granek, and M. Elbaum, *Diffusion and directed motion in cellular transport.* Physical Review E, 2002. **66**(1): p. 011916.

119. Ragsdale, G.K., J. Phelps, and K. Luby-Phelps, *Viscoelastic response of fibroblasts to tension transmitted through adherens junctions.* Biophys. J., 1997. **73**(5): p. 2798-2808.

120. Nan, X., et al., *Observation of Individual Microtubule Motor Steps in Living Cells with Endocytosed Quantum Dots.* J. Phys. Chem. B, 2005. **109**(51): p. 24220-24224.

121. Daniels, B.R., B.C. Masi, and D. Wirtz, *Probing Single-Cell Micromechanics In Vivo: The Microrheology of C. elegans Developing Embryos.* Biophys. J., 2006. **90**(12): p. 4712-4719.

122. Tolic-Norrelykke, I.M., et al., *Anomalous Diffusion in Living Yeast Cells.* Physical Review Letters, 2004. **93**(7): p. 078102-4.

123. Golding, I. and E.C. Cox, *Physical Nature of Bacterial Cytoplasm.* Physical Review Letters, 2006. **96**(9): p. 098102-4.

124. Wolfgang, F., W. Monika, and S. Erich, *Dictyostelium cells' cytoplasm as an active viscoplastic body.* European Biophysics Journal, 2001. **V30**(4): p. 284-294.

125. Wilhelm, C., F. Gazeau, and J.C. Bacri, *Rotational magnetic endosome microrheology: Viscoelastic architecture inside living cells.* Physical Review E (Statistical, Nonlinear, and Soft Matter Physics), 2003. **67**(6): p. 061908-12.

126. Tvarusko, W., et al., *Time-resolved analysis and visualization of dynamic processes in living cells*. 1999. p. 7950-7955.

127. Gittes, F. and F.C. MacKintosh, *Dynamic shear modulus of a semiflexible polymer network.* Physical Review E, 1998. **58**(2): p. R1241.

128. Morse, D.C., *Viscoelasticity of tightly entangled solutions of semiflexible polymers.* Physical Review E, 1998. **58**(2): p. R1237.

129. Erwin, F., *Physics in Cell Biology: On the Physics of Biopolymers and Molecular Motors.* ChemPhysChem, 2002. **3**(3): p. 270-275.

130. Doi, M. and S.F. Edwards, *The Theory of Polymer Dynamics* Internatioal Series of Monographs on Physics. Vol. 73. 1986, New York: Oxford University Press, Inc.

131. Schnurr, B., et al., *Determining Microscopic Viscoelasticity in Flexible and Semiflexible Polymer Networks from Thermal Fluctuations.* Macromolecules, 1997. **30**(25): p. 7781-7792.

132. Janmey, P.A., et al., *Viscoelastic properties of vimentin compared with other filamentous biopolymer networks.* J. Cell Biol., 1991. **113**(1): p. 155-160.

133. Leterrier, J.F., et al., *Mechanical Effects of Neurofilament Cross-bridges. MODULATION BY PHOSPHORYLATION, LIPIDS, AND INTERACTIONS WITH F-ACTIN.* J. Biol. Chem., 1996. **271**(26): p. 15687-15694.

134. Ma, L., et al., *Keratin Filament Suspensions Show Unique Micromechanical Properties.* J. Biol. Chem., 1999. **274**(27): p. 19145-19151.

135. Coulombe, P.A., et al., *The `ins' and `outs' of intermediate filament organization.* Trends in Cell Biology, 2000. **10**(10): p. 420-428.

136. Xu, J., Y. Tseng, and D. Wirtz, *Strain Hardening of Actin Filament Networks. REGULATION BY THE DYNAMIC CROSS-LINKING PROTEIN alpha -ACTININ.* J. Biol. Chem., 2000. **275**(46): p. 35886-35892.

137. Mucke, N., et al., *Assessing the Flexibility of Intermediate Filaments by Atomic Force Microscopy.* Journal of Molecular Biology, 2004. **335**(5): p. 1241-1250.